

DRAFT

A Volcano Rekindled: The Renewed Eruption of Mount St. Helens, 2004–2006.
Edited by David R. Sherrod, William E. Scott, and Peter H. Stauffer
U.S. Geological Survey Professional Paper 2007-XXXX

Chapter 30. Petrology of the 2004–2006 Mount St. Helens lava dome—implications for magmatic plumbing and eruption triggering

By John S. Pallister, Carl R. Thornber, Katherine V. Cashman, Michael A. Clyne, Heather A. Lowers, Charles W. Mandeville, Isabelle K. Brownfield, and Gregory P. Meeker

Abstract

Eighteen years after dome-forming eruptions ended in 1986, and with little warning, Mount St. Helens began to erupt again in October 2004. During the ensuing two years, the volcano extruded more than $80 \times 10^6 \text{ m}^3$ of gas-poor, crystal-rich dacite lava. The 2004–2006 dacite is remarkably uniform in bulk-rock composition and, at 65 percent SiO_2 , among the most silica-rich and incompatible-element-depleted magmas erupted at Mount St. Helens during the past 500 years. Since shortly after the first spine of lava appeared, samples have been collected using a steel box dredge (“Jaws”) suspended 20–35 m below a helicopter and, occasionally, by hand sampling. As of the spring of 2006, 25 age-controlled samples have been collected from the seven spines of the new lava dome. Samples were obtained from both the interiors of spines and from their carapaces, which are composed of fault gouge and cataclasite 1–2 m thick. The dacite lava is crystal rich, with 40–50 percent phenocrysts. The groundmass is extensively crystallized to a cotectic assemblage of quartz, tridymite, and Na- and K-rich feldspar microlites, raising the total crystal content to more than 80 percent on a vesicle-free basis in all but

the earliest erupted samples. Early samples and those collected from near the spine margin are more glassy and vesicular than those collected later and from the interior of the spines. Oxide thermobarometer determinations for the earliest erupted samples we collected cluster at temperatures of approximately 850°C and at an oxygen fugacity one log unit above the nickel-nickel oxide (NNO) buffer curve. In contrast, samples from relatively glass-poor samples erupted in late 2004 and early 2005 have zoned oxides with apparent temperatures that range to greater than 950°C . The higher temperatures in these microlite-rich rocks are attributed to latent heat evolved during extensive and rapid groundmass crystallization. Low volatile contents of matrix glasses and presence of tridymite and quartz in the high-silica rhyolite matrix glass indicate extensive shallow (<1 km) crystallization of the matrix, driven by degassing of water, and solidifying the magma below the level of the vent. The mode of eruption of the dacite as a series of fault-gouge-mantled spines is explained by this process of extensive subvent degassing and solidification.

Although the current dacite is more silica rich than 1980–86 dome rocks, most major and trace element concentrations of the 1980–86 and 2004–06 magma batches are broadly similar, and magmatic gas emissions

have been low and have had similar ratios to those of the 1980s, raising the possibility that the magma might be residual from the 1980–1986 reservoir. However, titanium and chromium are enriched relative to the most recent 1980–86 and Goat Rocks (A.D. 1800–1857) eruptive cycles, and heavy rare-earth element abundances are slightly depleted relative to those erupted during the past 500 years at Mount St. Helens. These data suggest either addition of new gas-poor dacite magma or tapping a region of the preexisting reservoir that was not erupted previously.

A relatively low pressure of last phenocryst growth suggests that the magma was derived from near the apex of the Mount St. Helens magma reservoir at a depth of about 5 km. Viewed in the context of seismic, deformation, and gas emission data, the petrologic and geochemical data can be explained by ascent of a geochemically distinct batch of magma into the apex of the reservoir during the period 1987–1997, followed by upward movement of magma into a new conduit, beginning in late September 2004.

The question of new versus residual magma has implications for the long-term eruptive behavior of Mount St. Helens, as arrival of a new batch of dacitic magma from the deep crust could herald the beginning of a new long-term cycle of eruptive activity. It is also important to our understanding of what triggered the eruption and its future course. Two hypotheses for triggering are considered: (1) top-down fracturing related to the shallow groundwater system and (2) an increase in reservoir pressure brought about by recent magmatic replenishment. With respect to the future course of the eruption, similarities between textures and character of eruption of the 2004–06 dome and the long-duration (greater than 100 years) pre-1980 summit dome, along with the low eruptive rate of the current eruption, suggest that the eruption could continue sluggishly for years to come.

Introduction

End members of natural phenomena offer important constraints on processes, in part because they provide a means to understand boundary conditions. The ongoing eruption of Mount St. Helens is such an end member, as it represents a sustained low-rate dacite eruption at a potentially explosive volcano. A fortunate combination of conditions has allowed us to investigate fundamental questions about volcanic plumbing systems, triggers for eruptions, and controls on explosivity.

The dacite has largely solidified to crystalline rock beneath the surface, such that the first two years of the eruption have been characterized by nearly continuous extrusion of lava spines. Furthermore, because the spines have been extruded at an angle, the vent has been partially exposed through most of the eruption, allowing up-close access by helicopter to install instruments, document the character of the spines, and collect a series of lava and gouge samples through time. The sample collection, along with field observations and seismic, deformation, thermal, and gas monitoring, form the basis for this and other petrologic papers in this volume.

We have employed an unusual method of sampling borrowed from the oceanographic community. A dredge bucket suspended beneath a helicopter was used repeatedly to collect samples from the actively extruding spines over the course of the eruption. Samples have been distributed widely to petrologists and geochemists at a variety of institutions in the U.S. and overseas. Accordingly, petrologic studies of the 2004–2006 eruption were undertaken through a team approach, which brought together more than 25 petrologists from a dozen institutions to contribute to the interpretation of the eruption (Pallister and others, 2005). We thank these scientists and acknowledge their contributions and those of our USGS colleagues, as through this community approach and synthesis of different types of data we have advanced our understanding.

This report deals primarily with the general petrology of the dacite lava and what it tells us about magmatic processes when viewed in the broader context of monitoring data and Mount St. Helens' history. We report results from field observations and petrographic studies using optical and scanning electron microscopy, microprobe analyses of glasses and Fe-Ti oxide minerals, Fourier Transform Infrared (FTIR) spectroscopy, and a comparison of the whole-rock major- and trace-element compositions of 2004–2006 samples with those of previous eruptive episodes at Mount St. Helens. Other petrologic reports in this volume focus on silicate mineral chemistry and zoning, isotopic data, phase equilibria, the petrology and chemistry of ash samples, as well as detailed studies of the chemistry of the dacite and textures of the unusually thick fault gouge that mantles the lava spines.

Field Geology and Sampling

A chronology of the eruption is given by Scott and others (this volume, chap. 1), and details of lava dome

growth are described and illustrated by Vallance and others (this volume, chap. 9) and summarized in digital elevation models and photogeologic maps (Schilling and others, this volume, chap. 8; Herriott and others, this volume, chap. 10). Here we provide only a brief outline of field relations used to establish eruption ages of samples and field observations that are important to interpretation of the petrology. The 2004–2006 eruption sequence began with intense seismic unrest, uplift of crater floor, and deformation of glacial ice during late September 2004 and was followed by a series of phreatic explosions during the first week of October. Beginning October 11, 2004, spines of juvenile lava extruded in the deformed area and have extruded virtually continuously ever since. On January 16, 2005, and March 8, 2005, the only sizable explosions since early October 2004 blanketed the crater floor with ash and ballistic fragments. For safety, use of a steel dredge (fig. 1), sling-loaded to a helicopter, and a few short-duration landings permitted collection of rock and gouge samples from the spines. A total of 25 locations were sampled on 16 days during the period between October 2004 and February 2006, as shown in table 1 and in the photogeologic maps of Herriott and others (this volume, chap. 10).

There have been no pumiceous eruptions, and, except for small flows formed during collapse of the initial spine in October–November 2004 (fig. 2), there have been no dome-collapse pyroclastic flows during the eruption. Descriptions of ash samples collected from deposits of the few small explosive eruptions and many small rockfalls and rock avalanches are given in Rowe and others (this volume, chap. 29), and descriptions of the fault gouge, which mantles the dacite spines, are given in Cashman and others (this volume, chap. 19).

On October 11, 2004, the first spine (spine 1) of new lava was extruded through uplifted glacier near the south flank of the 1980–1986 lava dome, and we began collecting lava samples soon after. During the remainder of October, spine 2 emerged and extended to the south, while a new area of the glacier was uplifted east and then southeast of the initial spine. Our initial samples were collected from spine 1 by helicopter dredging using a makeshift bucket dredge, followed by landings and hand sampling on October 27 and November 4. By October 27, protuberances of hot lava breached the area of uplifted glacier in the southeastern part of the crater, and by November 4 an elongate wedge of new lava emerged from the uplift, rose to a height of about 100 m (fig. 3), and was thrust laterally toward the south crater wall, plowing the crater glacier aside. Because of its elongate, recumbent form, spine 3 became known as a “whaleback,” a term used to describe similar recumbent

spines during an early stage of the eruption at Soufrière Hills volcano, Montserrat (Watts and others, 2002). Initially, the whaleback had a smooth east face mantled by soft white fault gouge; this face dipped 40–60° degrees east and was marked by downplunge striations and darker-colored “bathtub rings,” the latter recording uplifted positions where the spine had previously been in contact with a debris apron at its base. During November and December 2004, GPS data and fixed-camera observations recorded the whaleback moving southward in conveyor-like fashion, transporting new lava from a vent at its north end and shedding it as hot talus blocks to the south and west (Schilling and others, this volume, chap. 8; Vallance and others, this volume, chap. 9).

By mid-December 2004, oblique longitudinal fractures developed in spine 3. By early January 2005, spine 3 had broken into multiple fracture-bounded segments and spine 4 began to emerge from the vent. Spine 4 was also extruded southeast as a whaleback. It overrode rubble from spine 3 until it too reached the south crater wall and fragmented in mid- to late-April as spine 5 emerged from the vent. Spine 5 overrode and buried the two earliest spines. It began to fragment into rubble in late July 2005. Smaller, rubbly spine 6 then emerged, but it was extruded southwest from the vent and extended farther west than previous spines. During the fall of 2005, a sag opened between spines 5 and 6 as spine 6 continued to extrude and thrust upward and to the southwest. Finally, during October 2005 and continuing into 2006, spine 7 emerged and was thrust steeply to the southwest; it overrode spine 6, and part of it collapsed to form a talus apron that extended onto the narrowing west arm of the crater glacier, which was trapped between the westward-thrusting dome and the crater wall. The eruption of spine 7 has continued to the time of this writing (September 2006), characterized by near-vertical spine growth and collapse, producing a large mass of dacite rubble in the western part of the crater.

The relatively low angle of extrusion through most of the eruption produced inclined spines that were extruded to the south (spines 2–5), such that the northern half of the vent was exposed at the surface. The vent consisted of an arcuate rim of hot gouge, convex on its north side. The southern margin of the vent has not been exposed. Extrapolation of the exposed rim as a circle yields a vent diameter of 100–200 m; however, variably exposed extensions of the gouge rim along the east and west margins of the spines (on occasions for several hundred meters) suggest an oval vent outline. This oval outline may be the result of the inclined intersection of a north-plunging cylindrical conduit with the crater floor, or it may indicate a true elongation of the vent.

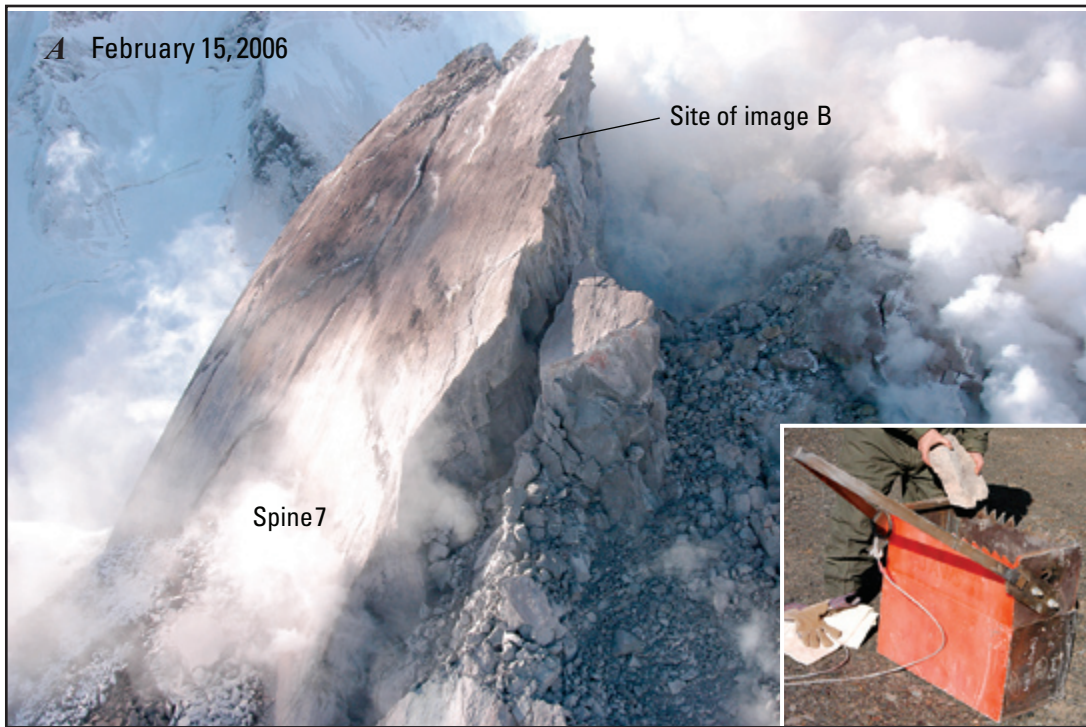


Figure 1. Photographs illustrating use and design of rock dredge. Dredge allowed collection from normally inaccessible locations as shown in the main photos. A, Upper lip of spine 7, where fragments of consolidated gouge and lava from close to the gouge carapace were collected on February 15, 2006. B, View looking down at dredge from helicopter while sampling blocks of dacite from near gouge contact. As shown in the inset photos, the dredge is plate-steel frame, 30 by 60 cm and 30 cm deep, beneath which hangs removable heavy-gauge wire-screen basket for collecting rocks (lower inset). Upper edge of frame is serrated to better bite into rock or gouge, giving dredge its informal name, “Jaws.” Basket can be replaced with steel box for sampling fine-grained material such as gouge (upper inset). Dredge is lifted from a steel ring attached to 1-m-long steel lift arm bolted to sides of frame to allow adjustment of bite angle. A steel leader cable 6 mm in diameter and 5-m-long is attached to steel ring on lift arm. The ring allows side loads to be imparted on dredge to help dislodge it if it becomes wedged in rock face. Steel cable is attached to standard electrically released sling-load cable from helicopter.

Table 1. Rock samples collected in the crater of Mount St. Helens from October 2004 to February 2006.

[All samples of new dome are multiple rock fragments collected by helicopter dredging except SH301 and SH325, collected by hand. Sample numbering sequence continues that adopted for Mount St. Helens reference collection from 1980–1986. Sample numbers with hyphenated suffixes (for example, SH304-2G1) elsewhere in the report refer to individual fragments in these composite samples (Thornber and others, 2007b). Eruption dates are estimated by using collection locations and known lineal rate of extrusion to track samples back to vent, as described in text. Limiting dates specify time interval for emplacement, from known field relations.]

Sample No.	Spine	Collection date	Eruption date	Limiting dates
SH300	1	10/20/2004	10/11/2004	10/11/04–10/20/04
SH300 ¹		do.	<1986 ¹	
SH301 ²	3	10/27/2004	<1986 ²	
SH302	2	10/27/2004	10/14/2004	10/12/04–10/27/04
SH304	3	11/4/2005	10/18/2004	10/12/04–11/04/04
SH305	3	1/3/2005	11/20/2004	10/27/04–12/01/04
SH306	4	1/14/2005	12/15/2004	12/07/04–12/21/05
SH307	4	2/22/2005	2/12/2005	02/01/05–02/15/05
SH308	4	2/22/2005	1/21/2005	01/15/05–02/01/05
SH309	4	2/22/2005	1/13/2005	01/07/05–01/25/05
SH310	4	2/22/2005	1/16/2005	01/10/05–01/28/05
SH311	4	1/19/2005	1/16/2005	01/16/05–01/19/05
SH312	4	4/10/2005	3/8/2005	03/08/05–03/08/05
SH313	4	4/19/2005	4/1/2005	03/15/05–04/05/05
SH314	5	4/19/2005	4/17/2005	04/16/04–04/19/05
SH315	4	4/19/2005	4/1/2005	03/15/05–04/05/05
SH316	5	5/24/2005	4/15/2005	04/01/05–05/10/05
SH317	5	6/15/2005	5/1/2005	04/10/05–05/30/05
SH318	5	7/13/2005	7/7/2005	07/01/05–07/09/05
SH319	5	7/13/2005	5/15/2005	05/01/05–05/25/05
SH320	5	7/13/2005	7/1/2005	06/26/05–07/06/05
SH321	6	8/19/2005	8/10/2005	08/05/05–08/19/05
SH322	6	8/19/2005	8/15/2005	08/10/05–08/19/05
SH323	6	10/18/2005	9/10/2005	08/10/05–10/19/05
SH324	7	12/15/2005	12/5/2005	11/23/05–12/07/05
SH325	7	02/07/2006	12/20/2006	12/05/05–01/01/06
SH326	7	02/15/2006	1/10/2006	01/01/06–01/20/06

¹Dredge sample SH300 contained 2004 dacite and rock fragments uplifted from crater floor (1980–86 dome or shallow conduit rock).

²Hand sample SH301 contained several dacite blocks pushed up from crater floor (1980–86 dome or shallow conduit rock).

Each of the spines displayed a carapace of white to tan fault gouge or cataclasite 1–2 m thick as it emerged from the vent (Cashman and others, this volume, chap. 19). The gouge zone is striated with multiple layers of subparallel slickensides oriented parallel to the transport direction at the point of emergence from the vent. The orientation of the slickensides, combined with photographically or GPS-determined rates of linear spine transport, provide a means to “backtrack” sample localities to the vent and thereby establish eruption

ages, as illustrated by Herriott and others (this volume, chap. 10). Using this method, approximate eruption dates have been estimated for each of the dome samples, along with age ranges, the latter reflecting uncertainty in rate of transport from the vent to the collection locality (table 1). One sample (SH312) is assigned a unique eruption age, coincident with the explosion of March 8, 2005, as it was melted into a nylon rope on a near-vent monitoring station (McChesney and others, this volume, chap. 7; LaHusen and others, this volume, chap. 16).

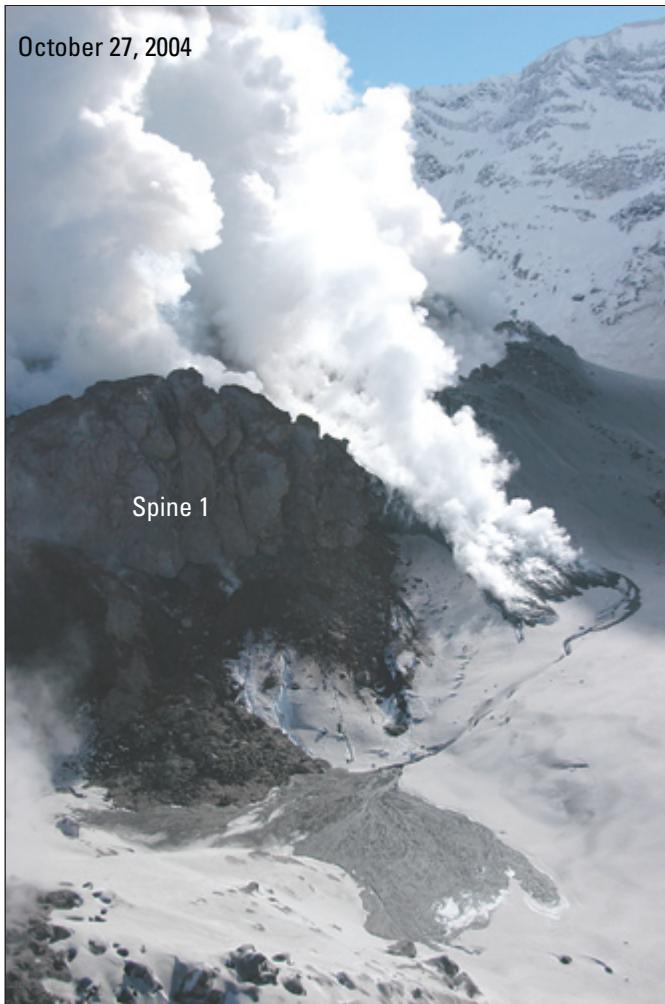


Figure 2. Oblique aerial photograph (view to southeast) of small pyroclastic flow (with vapor clouds rising from it) produced by rockfall from spine 2 (shrouded in cloud) on October 27, 2004. Snowmelt from flow produced watery lahar in small channel on snow-covered glacier, forming small debris fan in basin at base of spine 1.

Laboratory Methods

Petrography and Microbeam Analysis

Polished thin sections of representative samples were prepared and examined using petrographic and scanning electron microscopes (SEM), electron microprobe, and imaging methods. Because of extensive, very fine grained groundmass crystallization, modal analyses were done using a combination of optical point counting, low- and high-magnification SEM image analysis of backscattered electron images, and multi-element microprobe-stage raster maps. Thin section raster map data were processed using image analysis software to give area percentages for a series of color

bins, which were adjusted to differentiate phases in the sample and then combined through a series of additions, subtractions, and normalizations to yield approximate area percentages of the phases. Stage-raster maps were made at low (1 cm^2) and high (2.56 mm^2) magnifications. For example, the color spectrum was adjusted so that red areas in the low-magnification Al map equal area percentage of plagioclase phenocrysts (fig. 4). When added to percent of small green lath-shaped microlites in the high-magnification Al map, the total feldspar abundance was obtained. Similarly, red to yellow areas of the two Fe maps gives the percentage of oxides, which is subtracted from the percentage of nonblack areas in the low-magnification Si map to determine percentage of void space. Yellow areas in the high-magnification Si map give the percentage of SiO_2 phases, which are present only in the groundmass. Glass abundance is obtained from the K maps by subtracting the area percentage of K-rich phases (yellow, alkali feldspar) in the high-magnification map from the percentage of glass (blue) in the low-magnification map. Using these types of mapping and image analysis techniques, it has been possible to quantify the abundance and textures of crystals, glass, and vesicles at scales ranging from centimeters to microns (table 2).

Matrix glass, glass inclusions, oxide minerals, and selected silicate minerals were analyzed using the electron microprobe, and the results are summarized in tables 3 and 4 and in the appendix. Most microprobe analyses were conducted at 15-kV accelerating voltage and 20-nA beam current, using the JEOL 8900 microprobes at USGS laboratories in Denver, Colo., and Menlo Park, Calif. SEM analyses were conducted using a JEOL 5800LV SEM equipped with an energy-dispersive X-ray system (EDS) at the USGS microbeam laboratory in Denver. Natural and synthetic silicate standards were used and off-peak background corrections were applied to standards and unknowns, and secondary silicate mineral standards were used to verify and monitor the analytical routines. Glass standard NIST SRM 610 (Ihinger and others, 1994; Pearce and others, 1997) was used as a secondary standard for S and Cl. Beam spot sizes were varied according to the material being analyzed and the nature of the problem being examined. Point beams were used for oxides and to examine zoning profiles, larger spot sizes (to $40 \mu\text{m}$) were used where possible to analyze glasses, and iterative counting techniques, similar to those pioneered by Nielson and Sigurdsson (1981), were used during all glass analyses to monitor and, where indicated, to correct for alkali and silica migration. To avoid loss related to electron beam damage, the elements Na, K,

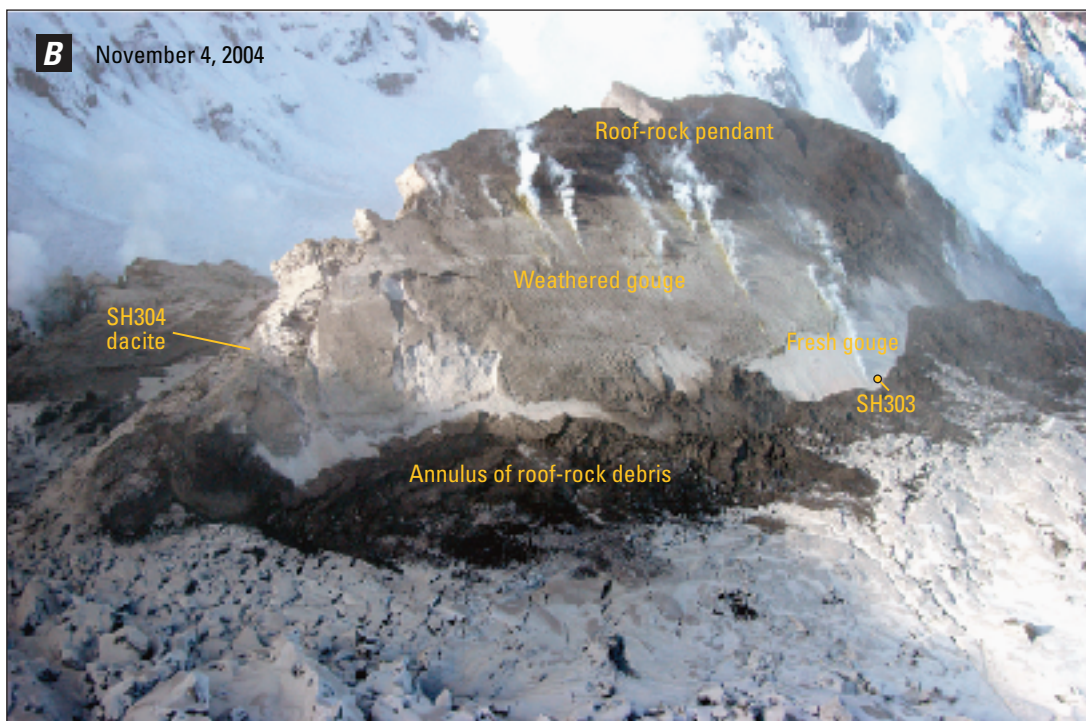
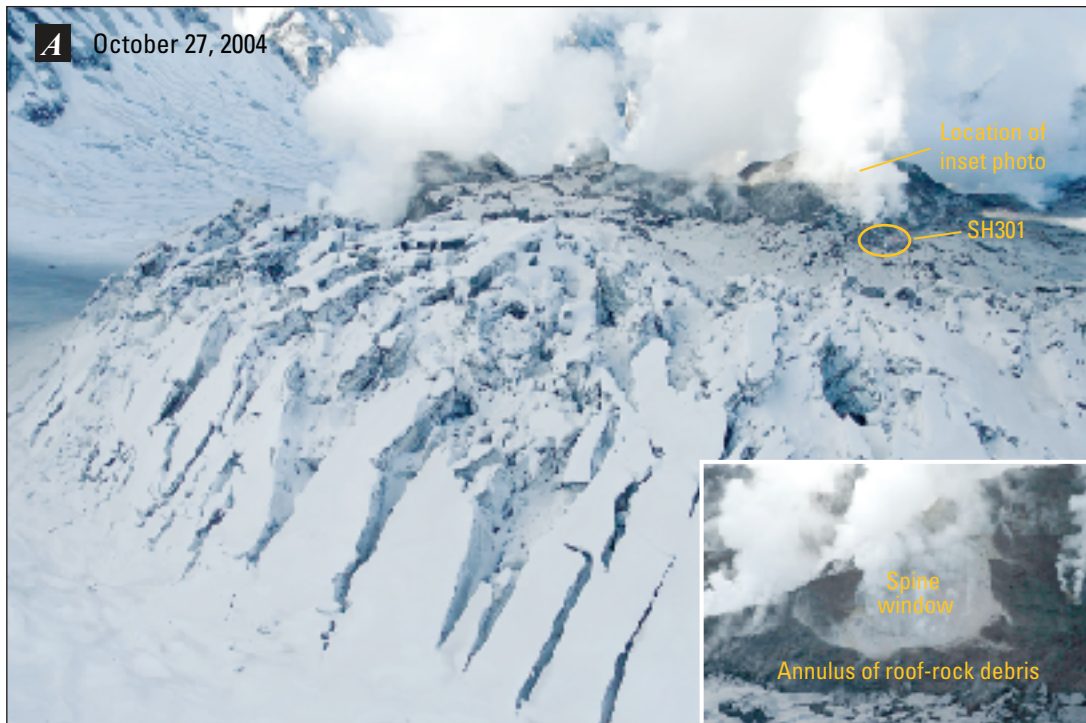
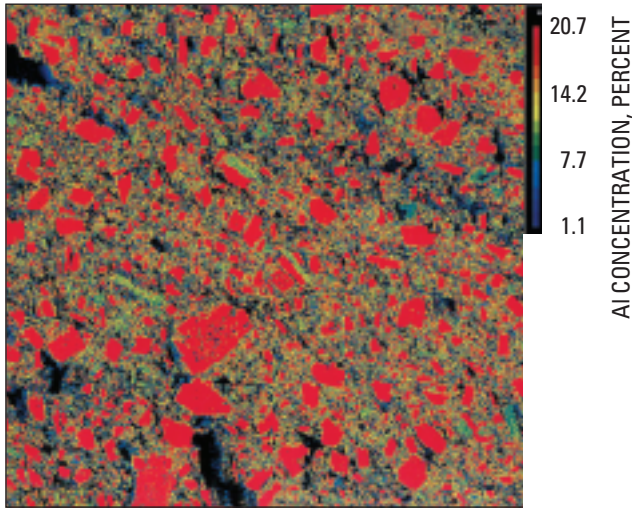
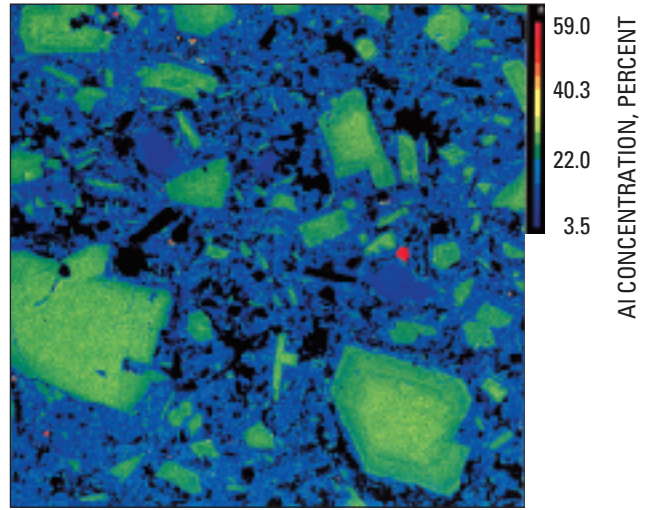


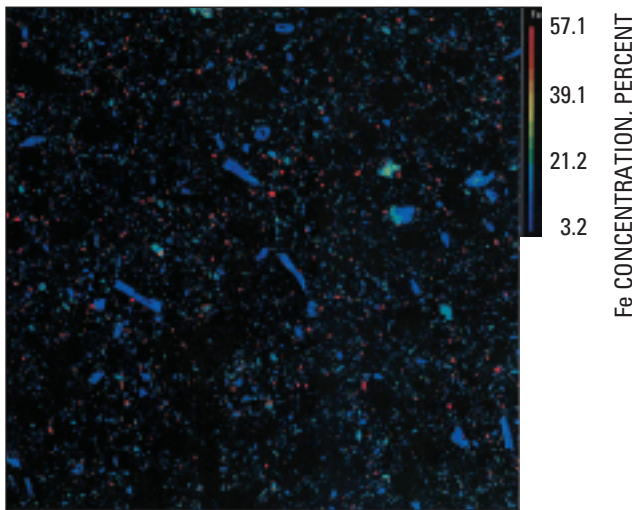
Figure 3. Sampling sites for new dome rocks early in eruption. A, View to west of lava exposed at crest of uplifted glacier in southeast crater on October 27, 2004. Steam emanates from surface of spine 3, surrounded by dark (wet) debris from the crater floor and root of the 1980-86 dome that was brought to surface atop spine. Inset shows initial window through crater-floor debris, exposing gouge on spine 3 surface. Our sample (SH301) was from roof rock collected near helicopter (circled). B, View to northwest of same area on November 4, 2004, showing fault-gouge mantled and striated east face of spine 3, now about 100 m above uplifted surface of the deformed glacier. First dense dacite sample of the spine interior (SH304) was dredged from southeast end of spine 3 and was still hot when returned to a staging area 10 km distant. First gouge sample was collected during a short-duration landing at SH303. Note roof-rock pendant of crater-floor debris, which was transported upward as spine emerged from glacier and rose upward and obliquely to the southeast. See Cashman and others (this volume, chap. 19) for additional details of gouge carapace.



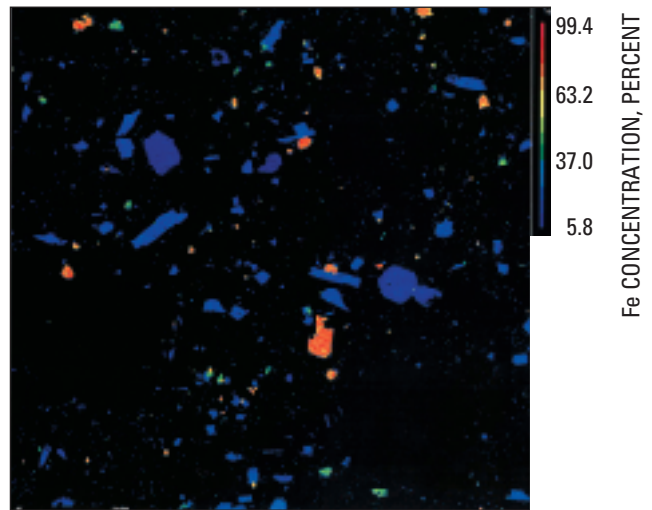
AI MAP, 1 x 1 CENTIMETERS



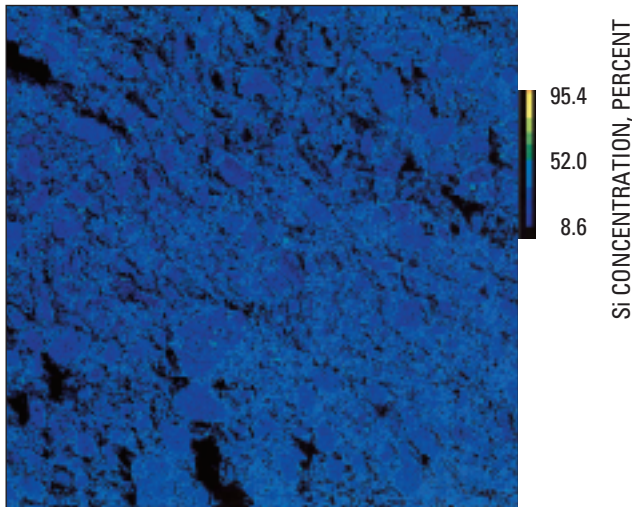
AI MAP, 1.6 x 1.6 MILLIMETERS



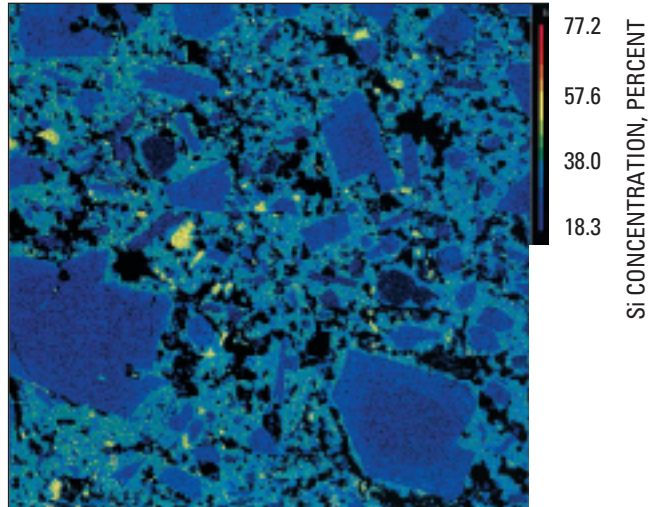
Fe MAP, 1 x 1 CENTIMETERS



Fe MAP, 1.6 x 1.6 MILLIMETERS



Si MAP, 1 x 1 CENTIMETERS



Si MAP, 1.6 x 1.6 MILLIMETERS

Caption on next page.

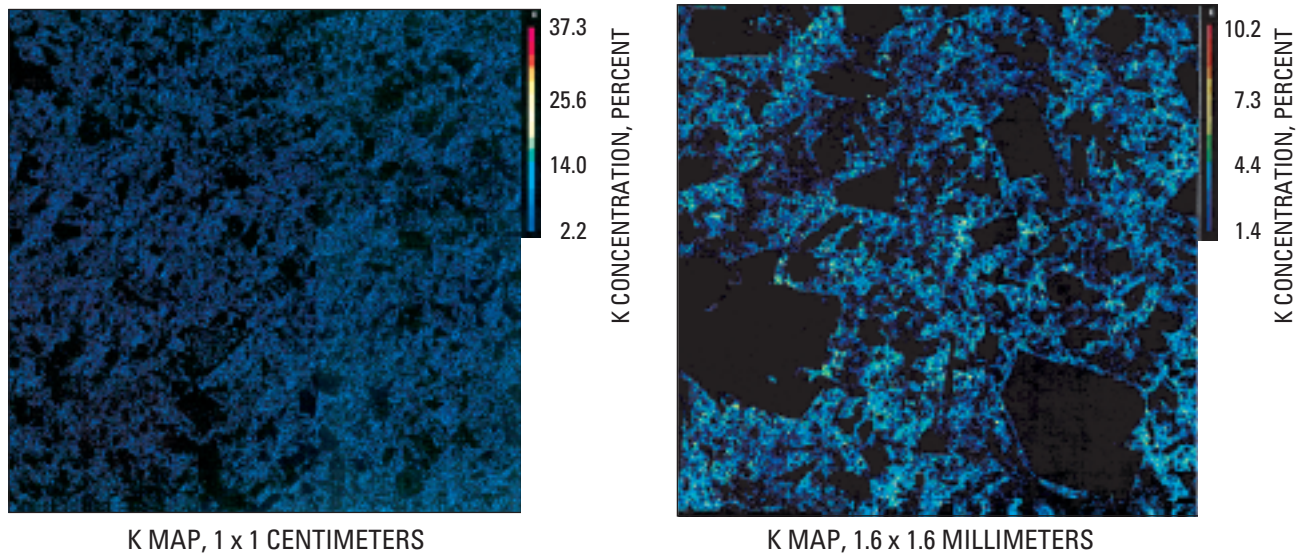


Figure 4. Electron microprobe-stage raster maps of sample SH305-1A illustrating procedure for deriving abundance of phases from image analysis. Each map produced by driving microprobe stage over areas approximately 1 cm² and then 2.6 mm² (the latter to differentiate matrix phases) while simultaneously recording X-ray peak intensities from five wavelength-dispersive spectrometers and from backscattered electron detector. The X-ray intensities are compared to standard intensities to derive approximate concentrations of major elements as oxides and plotted according to stage position to produce images shown here.

and Si were analyzed before other elements in glasses, and count rates were collected for these elements starting immediately when the beam was unblanked. Curves were individually fit to the count rate data for each analysis, and the intercept at time zero was used in the data reduction routines. Long count times (>300 seconds on and off peak) were used for S and Cl analyses, yielding detection limits of 70–90 ppm for S and about 50 ppm for Cl. On the basis of long-term reproducibility of standard analyses, analytical reproducibility for microprobe analyses is estimated as 1–2 percent of the reported amounts for major elements, except for H₂O, which is calculated by the difference of complete major- and minor-element probe analyses from 100 percent and is subject to uncertainties of about 1 weight percent.

In addition, three sets of approximately 700-1000 microprobe point analyses each were done in polygonal grids and averaged to characterize the bulk composition of two small quenched inclusions. A third set of gridded point analyses were done over a similar-size grid in the host dacite to test the method. To save time, mean atomic number background corrections and short (approximately 20 s) dwell times were used for these analyses, cutting analytical time to approximately 36 hours for each area. The resulting data for the dacite host were also used to calculate an analytical mode by binning analyses into mineral types, glass, and void space according to a series of compositional and stoichiometric rules (see “Probe,” table 5).

IR Spectroscopy Analysis

Dissolved water and carbon dioxide in two unusual glassy samples, SH304-2G1 and SH304-2G2, were determined by Fourier Transform Infrared (FTIR) spectroscopy in the Department of Earth and Planetary Sciences at the American Museum of Natural History, utilizing a Nicolet 20SXB FTIR spectrometer attached to a Spectra Tech IR Plan microscope, according to methods described by Mandeville and others (2002). A total of 10 to 16 spots were measured in the most microlite-free (Fe-Ti oxides and orthopyroxene) regions of matrix glass in each sample, and IR results are reported in table 6. Because of the small size of glass inclusions and matrix melt films in the typical microcrystalline dacite, it has only been possible to determine water contents by FTIR on the matrix glass in the one glass-rich sample (SH304-2G).

Bulk-Rock Analysis

Representative samples of the dacite lava were coarse crushed in a hydraulic press and hand-picked for bulk rock analyses. Splits of the crushed dacite were cleaned of xenolithic material, and the cleaned samples were submitted for analysis at USGS labs in Denver, Colo. Splits of many of the samples were also analyzed at Washington State University’s Geoanalytical Laboratory. Major-element analyses of whole-rock samples were

Table 2. Modal data for samples from 2004–2006 Mount St. Helens lava dome. Further explanation of methods in “Laboratory Methods” section.

[Optical modes, as volume percent, are derived by counting 1,000 or 1,300 points at 100x magnification. Grains and voids smaller than 30 μm in maximum dimension are counted as matrix.

TS, thin section; DRE, dense-rock-equivalent abundances. DRE calculated by subtracting voids and renormalizing the optical modes and microbeam “ALL” modes.

Hornblende, used informally for a range of amphibole compositions, forms large (1-3 mm) phenocrysts; consequently its abundance in individual sections may not be statistically representative.

Silica phases are late stage in their formation and are excluded in the phenocryst abundance.

Microbeam map analysis modes, as volume percent, derived from image analysis of 1-cm² microprobe stage-raster maps of X-ray intensities for Si, Al, Mg, Fe, K and backscattered electron intensity, combined with image analysis of SEM backscattered electron images of 100-μm² areas.

Column labeled “All” tabulates complete modal analysis, including microlites (1-30 μm maximum diameter), obtained by microbeam imaging at scales of 1 cm² and 100 μm².

Probe DRE for phenocryst abundance calculated from 1,024 analyses of 1-μm spots distributed over a 1-cm² grid and binned (after excluding 262 analyses with totals >102% or <85%) according to mineral types and glass using the following compositional and stoichiometric rules:

Plagioclase if Si+Al = 3.85-4.15 (based on 8 oxygens) and K2O <2 percent;

Anorthoclase if Si+Al = 3.85-4.15 (based on 8 oxygens) and K2O >2 percent;

Hypersthene if MgO >17 percent;

Hornblende if MgO = 8-17 percent and Na2O >1 percent;

Quartz if SiO2 >78 percent;

Silica phase (tridymite, cristobalite) if SiO2 = 72-78 percent;

Fe-Ti oxide if FeO+TiO2 >30 percent and SiO2 <10 percent.

Plagioclase category as part of microprobe analysis may include anorthoclase, except where counted separately in the analysis of SH315-4.

Microlite abundance calculated by subtracting total crystals determined by microbeam analysis from phenocryst abundance determined by microbeam (m) or optical (o) methods.

Values for glass by K2O balance are weight percent and calculated on a volatile-free basis from the percentage of glass needed to give the K2O determined by bulk chemical analysis. To convert to volume percent, multiply by 1.1]

Optical mode, percent	SH304-2A, spine 3 1000 points counted			SH304-2G1, spine 3 1000 points counted			SH305-1A, spine 3 1300 points counted			SH315-4, spine 4 1300 points		
	TS	DRE	DRE	TS	DRE	DRE	TS	TS	DRE	TS	TS	DRE
Plagioclase	30	31	32	22	22	22	27	27	30	39	39	39
Hypersthene	4	4	4	3	3	3	4	4	5	6	6	6
Hornblende	8	8	2	2	2	2	4	4	4	4	4	4
Oxides	2	2	2	1	1	1	2	2	2	2	2	2
Silica phases							0.2	0.2	0.2			
Voids	2			0.4			9	9		1		
Matrix	55	55	60	72	73	73	53	53	59	49	49	49
Sum	100	100	100	100	100	100	100	100	100	100	100	100
Phenocrysts	44	45	40	27	27	27	37	37	41	51	51	51

Microbeam map analysis, percent	SH319-1, spine 5 1300 points counted			SH321-A, spine 6 1300 points counted			SH325-1A, spine 7 1300 points counted			SH-305-1A			Probe (DRE)		
	TS	DRE	All	DRE	TS	All	DRE	TS	All	DRE	TS	All	DRE	TS	DRE
Plagioclase	32	35	47	64	22	22	22	32	33	52	32	33	52	32	48
Anorthoclase															15
Hypersthene	3	4	4	5	2	4	4	5	5	8	5	5	8	5	5
Hornblende	5	6	6	8	2	2	2	3	3	6	3	3	6	3	3
Oxides	1	1	1	1	0.3	0.4	0.4	1	1	2	1	1	2	1	1
Silica phases															16
Voids	8		25	22	1	1		36	37		36	37			
Glass			17		73	71	72	18	19	30	18	19	30		13
Matrix	50	55	100	100	100	100	100	4	100	100	4	100	100		100
Sum	100	100	100	100	100	100	100	100	100	100	100	100	100		100
Phenocrysts	42	45	58	78	26	28	28	41	43	69	41	43	69		87
Total crystals															
Microlites (m)				33			2			29			29		
Microlites (o)				38			1			28			28		37
K ₂ O weight percent					3.38	1.83	54				5.09	1.41			
Glass by K ₂ O balance															28

Optical mode, percent ¹	SH319-1, spine 5 1300 points counted			SH321-A, spine 6 1300 points counted			SH325-1A, spine 7 1300 points counted			Average microcrystalline dacite			
	TS	DRE	All	DRE	TS	All	DRE	TS	All	DRE	TS	DRE	SD
Plagioclase	36.3	36.9	37.1	37.8	37.1	37.8	37.8	33.8	34.4	34.4	33.9	34.8	3.7
Hypersthene	5.2	5.3	6.3	6.4	6.3	6.4	6.4	2.5	2.6	2.6	4.7	4.8	1.4
Hornblende ⁴	5.5	5.6	3.5	3.6	3.5	3.6	3.6	2.6	2.7	2.7	4.6	4.7	2.0
Oxides	1.4	1.4	1.1	1.1	1.1	1.1	1.1	1.4	1.4	1.4	1.6	1.6	0.4
Silica phases ⁵	1.1	1.1	1.0	1.0	1.0	1.0	1.0	1.1	1.1	1.1	0.8	0.9	0.4
Voids	1.6		1.8		1.8			1.8			2.8		
Matrix	48.8	49.6	49.2	50.1	49.2	50.1	50.1	56.8	57.8	57.8	51.9	53.5	4.4
Sum	100.0	100.0	100.0	100.0	100.0	100.0	100.0	100.0	100.0	100.0	100.3	100.3	0.1
Phenocrysts	48.5	49.3	49.0	48.9	49.0	48.9	48.9	41.4	41.1	41.1	45.6	46.0	4.3

Table 3A. Electron-microprobe analyses of matrix minerals in 2004–2006 dacite.

[Oxides in weight percent.]

Sample No.	SiO ₂	Al ₂ O ₃	FeO	MgO	CaO	Na ₂ O	K ₂ O	TiO ₂	P ₂ O ₅	MnO	BaO	Total
<u>Anorthoclase and orthoclase microlites (less than 30 μm)</u>												
SH322-1-d-7	68.3	18.3	0.47	0.00	0.40	5.73	6.70	0.06	0.02	0.01	0.13	100.1
SH322-1-d-5	65.3	21.5	0.37	0.02	2.95	7.54	2.50	0.04	0.03	0.00	0.04	100.2
<u>Plagioclase microlites (less than 30 μm)</u>												
SH322-1-d-4	60.9	24.0	0.36	0.00	5.05	7.58	1.48	0.03	0.01	0.00	0.07	99.5
SH321-C-7d-3 (i)	62.3	23.0	0.52	0.00	3.77	8.00	1.42	0.05	0.01	0.00	0.10	99.2
SH321-C-7b-2 (h)	60.8	24.5	0.48	0.00	5.43	7.53	1.11	0.04	0.00	0.01	0.04	99.9
SH321-C-7c-7 (h)	59.9	25.0	0.47	0.00	6.14	7.42	0.93	0.01	0.00	0.00	0.03	99.8
SH321-C-7d-2 (i)	60.3	24.3	0.51	0.02	5.32	7.62	0.82	0.01	0.01	0.01	0.07	99.0
SH321-C-7d-1 (i)	57.0	26.6	0.58	0.00	8.14	6.66	0.45	0.03	0.00	0.01	0.02	99.5
<u>Plagioclase microphenocryst (100 μm)</u>												
SH322-1-b-17	58.6	26.2	0.43	0.01	7.46	6.94	0.58	0.00	0.01	0.01	0.03	100.3
SH322-1-b-18	59.5	25.8	0.35	0.01	6.76	7.45	0.40	0.02	0.02	0.00	0.05	100.3
SH322-1-b-19	58.5	26.0	0.31	0.00	7.36	7.23	0.23	0.03	0.00	0.00	0.06	99.7
SH322-1-b-20	59.8	25.5	0.49	0.00	6.83	7.35	0.67	0.01	0.00	0.01	0.07	100.7
<u>Quartz microlites</u>												
SH321-C-7c-6 (h)	100.0	0.14	0.29	0.01	0.01	0.00	0.03	0.04	0.00	0.01	0.02	100.6
SH321-C-7b-4 (h)	98.3	0.38	0.16	0.01	0.02	0.07	0.05	0.07	0.01	0.00	0.05	99.2
SH321-C-7d-4 (i)	99.6	0.12	0.17	0.01	0.01	0.02	0.00	0.04	0.00	0.00	0.01	99.9
SH321-C-7d-5 (i)	99.5	0.07	0.16	0.00	0.03	0.00	0.01	0.06	0.00	0.00	0.02	99.9
SH322-1-d-3	98.7	0.63	0.11	0.02	0.05	0.13	0.05	0.10	0.00	0.02	0.03	99.8
<u>Tridymite microlites</u>												
SH322-1-b-9	99.1	1.06	0.07	0.00	0.01	0.40	0.02	0.12	0.00	0.00	0.02	100.8
SH322-1-b-10	99.3	0.94	0.07	0.00	0.02	0.34	0.02	0.06	0.01	0.01	0.01	100.7
SH322-1-b-11	98.7	1.02	0.11	0.00	0.03	0.39	0.02	0.10	0.01	0.00	0.00	100.3
SH322-1-d-2	97.0	1.52	0.09	0.00	0.03	0.41	0.11	0.11	0.00	0.02	0.07	99.4
<u>Cristobalite microlites</u>												
SH312-1	93.9	4.27	0.35	0.00	0.15	0.71	0.68	0.15	0.00	0.01	0.04	100.3
SH321-C-7b-5 (h)	93.3	3.57	0.25	0.03	0.36	1.27	0.39	0.08	0.01	0.02	0.00	99.3

obtained by X-ray fluorescence (XRF) methods (Taggart and others, 1987). Trace-element abundances for selected samples were determined by Induction Coupled Plasma–Mass Spectrometric (ICP–MS) and Instrumental Neutron Activation Analysis (INAA) methods (Baedeker and McKown, 1987). On the basis of replicate analyses of standards, analytical reproducibility of major-element abundances is estimated to be better

than 0.4 percent of the reported values for SiO₂ and Al₂O₃. For other elements, reproducibility is better than ± 2 percent of values in the range 1–10 wt. percent and better than ± 6 percent for abundances less than 1 wt. percent. Coefficients of variation ($100 \sigma/x$ in percent) for INAA analyses, based on counting statistics, are given in table 7.

Table 3B. Calculated properties of matrix minerals in 2004–2006 dacite.

[Molecular percent anorthite (An), albite (Ab), and orthoclase (Or). Number of cations based on eight oxygens.]

Sample No.	An	Ab	Or	Si	Al	Fe	Mg	Ca	Na	K	Ti	P	Mn	Ba	Total
<u>Anorthoclase and orthoclase microlites (less than 30 µm)</u>															
SH322-1-d-7	2	55	43	3.04	0.960	0.017	0.000	0.019	0.494	0.380	0.002	0.001	0.000	0.002	4.91
SH322-1-d-5	15	70	15	2.88	1.12	0.014	0.001	0.140	0.646	0.141	0.001	0.001	0.000	0.001	4.95
<u>Plagioclase microlites (less than 30 µm)</u>															
SH322-1-d-4	25	67	9	2.73	1.27	0.013	0.000	0.243	0.660	0.085	0.001	0.000	0.000	0.001	5.00
SH321-C-7d-3 (i)	19	73	8	2.79	1.22	0.020	0.000	0.181	0.695	0.081	0.002	0.000	0.000	0.002	4.99
SH321-C-7b-2 (h)	27	67	6	2.71	1.29	0.018	0.000	0.260	0.651	0.063	0.001	0.000	0.000	0.001	4.99
SH321-C-7c-7 (h)	30	65	5	2.68	1.32	0.018	0.000	0.294	0.644	0.053	0.000	0.000	0.000	0.001	5.01
SH321-C-7d-2 (i)	26	69	5	2.72	1.29	0.019	0.001	0.256	0.666	0.047	0.000	0.000	0.000	0.001	5.00
SH321-C-7d-1 (i)	39	58	3	2.58	1.42	0.022	0.000	0.394	0.583	0.026	0.001	0.000	0.000	0.000	5.02
<u>Plagioclase microphenocryst (100 µm)</u>															
SH322-1-b-17	36	61	3	2.62	1.38	0.016	0.001	0.357	0.601	0.033	0.000	0.000	0.000	0.001	5.01
SH322-1-b-18	33	65	2	2.65	1.36	0.013	0.000	0.323	0.643	0.023	0.001	0.001	0.000	0.001	5.01
SH322-1-b-19	36	63	1	2.62	1.38	0.012	0.000	0.354	0.629	0.013	0.001	0.000	0.000	0.001	5.01
SH322-1-b-20	33	64	4	2.66	1.34	0.018	0.000	0.325	0.633	0.038	0.000	0.000	0.000	0.001	5.01
<u>Quartz microlites</u>															
SH321-C-7c-6 (h)				3.99	0.007	0.010	0.001	0.000	0.000	0.001	0.001	0.000	0.000	0.000	4.01
SH321-C-7b-4 (h)				3.98	0.018	0.006	0.001	0.001	0.005	0.002	0.002	0.000	0.000	0.001	4.01
SH321-C-7d-4 (i)				3.99	0.006	0.006	0.000	0.000	0.001	0.000	0.001	0.000	0.000	0.000	4.01
SH321-C-7d-5 (i)				3.99	0.003	0.005	0.000	0.001	0.000	0.000	0.002	0.000	0.000	0.000	4.00
SH322-1-d-3				3.97	0.030	0.004	0.001	0.002	0.010	0.003	0.003	0.000	0.001	0.000	4.02
<u>Tridymite microlites</u>															
SH322-1-b-9				3.95	0.050	0.002	0.000	0.000	0.031	0.001	0.003	0.000	0.000	0.000	4.04
SH322-1-b-10				3.96	0.044	0.002	0.000	0.001	0.026	0.001	0.002	0.000	0.000	0.000	4.03
SH322-1-b-11				3.95	0.048	0.004	0.000	0.001	0.030	0.001	0.003	0.000	0.000	0.000	4.04
SH322-1-d-2				3.93	0.073	0.003	0.000	0.001	0.032	0.005	0.003	0.000	0.001	0.001	4.05
<u>Cristobalite microlites</u>															
SH312-1				3.81	0.204	0.012	0.000	0.007	0.056	0.035	0.005	0.000	0.000	0.001	4.13
SH321-C-7b-5(h)				3.82	0.172	0.008	0.002	0.016	0.101	0.020	0.003	0.000	0.001	0.000	4.15

Table 4. Electron-microprobe analyses of matrix glass and glass inclusions in 2004–2006 Mount St. Helens dacite and two quenched inclusions from the dacite.

[Oxide abundances in weight percent; Cl and S recalculated as ppm. Sample numbers follow standard format (for example, SH305-1) but have additional coding for specific thin section, spot number; may show additional feature, “core,” to refer to melt inclusions in reacted core of plagioclase. Size indicates beam diameter, in microns. Phases coded as m, matrix; i, inclusion; p, plagioclase; h, hypersthene; a, amphibole; o, oxide. For inclusions, codes combined to show host mineral. Count rates were monitored for Na, K, and Si during each analysis, and these elements were corrected for migration as described in “Laboratory Methods” section. H₂O calculated by difference. Detection limit, D.L., for S ranges between 70 and 86 ppm and corresponds to the value at which one standard deviation is equivalent to 66 percent of the reported value. Lower values reported for S whenever a peak is detected above background, along with larger standard deviation. None detected, n.d., indicates no peak detected above background levels. Column headed “SD, S” shows standard deviation for S, in percent]

Sample and Spot No.	Size	Phase	SiO ₂	Al ₂ O ₃	FeO	MgO	CaO	Na ₂ O	K ₂ O	TiO ₂	P ₂ O ₅	MnO	BaO	Cl	SO ₃	Total	H ₂ O	Cl	S	D.L.	SD, S
<i>Glass inclusions in microcrystalline dacite</i>																					
SH305-1 kc g-6 (core)	1	ip	77.7	11.2	1.02	0.22	0.34	2.82	5.33	0.33	0.05	0.01	0.08	0.081	n.d.	99.23	0.8	810	n.d.	70	
SH305-1 kc g-7 (core)	1	ip	77.3	10.7	1.52	0.26	0.38	2.66	5.32	0.54	0.05	0.00	0.07	0.120	n.d.	98.94	1.1	1200	n.d.	73	
SH305-1 kc g-8 (core)	1	ip	76.8	11.2	1.28	0.18	0.31	2.56	5.36	0.55	0.09	0.02	0.07	0.084	n.d.	98.45	1.6	840	n.d.	76	
SH305-1 kc g-9 (core)	1	ip	77.2	11.1	1.19	0.18	0.37	2.59	5.40	0.49	0.07	0.01	0.08	0.064	n.d.	98.74	1.3	640	n.d.	70	
SH305-1 kc g-10 (core)	1	ip	77.9	11.1	1.25	0.18	0.33	2.60	5.24	0.46	0.05	0.03	0.09	0.057	n.d.	99.28	0.7	570	n.d.	74	
SH305-1 kc g-12 (core)	1	ip	77.4	10.8	0.96	0.04	0.23	2.68	5.16	0.35	0.07	0.00	0.05	0.060	n.d.	97.77	2.2	600	n.d.	73	
SH305-1 kc g-5	1	ip	77.3	11.0	1.14	0.26	0.37	2.61	5.37	0.27	0.04	0.01	0.07	0.086	0.013	98.49	1.5	860	52	66	75
SH305-1 kc g-21	1	ip	78.0	11.6	1.21	0.11	0.38	2.49	5.01	0.45	0.10	0.01	0.04	0.040	0.007	99.43	0.6	400	26	70	150
SH305-1 kc g-22	1	ih	76.6	12.4	1.35	0.03	0.27	3.01	5.72	0.34	0.08	0.01	0.05	0.110	n.d.	99.97	0.0	1100	n.d.	75	
SH305-1 kc g-27	1	ih	71.5	16.8	1.61	1.42	0.99	4.09	2.37	0.17	0.09	0.05	0.06	0.052	0.062	99.27	0.7	520	250	71	18
SH305-1 kc g-23	1	ih	76.8	12.1	1.12	0.01	0.24	3.02	5.63	0.31	0.05	0.02	0.06	0.096	n.d.	99.45	0.5	960	n.d.	75	
SH305-1 kc g-25	1	ia	74.3	13.3	0.98	0.08	0.38	3.14	5.50	0.64	0.07	0.00	0.07	0.145	0.007	98.61	1.4	1450	26	70	154
Average			76.6	11.9	1.22	0.25	0.38	2.85	5.12	0.41	0.07	0.02	0.07	0.08	0.022	98.97	1.0	829		72	
Standard deviation			1.9	1.7	0.20	0.38	0.20	0.44	0.88	0.14	0.02	0.01	0.01	0.03	0.027	0.59	0.6	309			
SH304-2 A9b hb1	1	ia	75.0	13.7	0.84	0.01	0.88	2.45	5.23	0.20	0.02	0.01	0.10	0.105	0.012	98.54	1.5	1050	48	86	110
SH304-2 A9b hb1	20	ia	75.3	13.6	0.86	0.01	0.85	2.03	4.98	0.23	0.06	0.04	0.11	0.112	0.007	98.16	1.8	1120	27	86	216
SH304-2 A9b hb1	20	ia	75.2	13.5	0.87	0.01	0.88	2.32	5.09	0.19	0.01	0.00	0.10	0.103	n.d.	98.37	1.6	1030	n.d.	85	
SH304-2 A9b hb6	5	ia	74.1	12.9	0.81	0.01	0.63	3.44	5.55	0.22	0.03	0.03	0.10	0.125	n.d.	97.93	2.1	1250	n.d.	85	
SH304-2 A9b ighb gl1	1	ia	74.0	14.2	0.91	0.12	0.80	3.69	5.02	0.17	0.05	0.02	0.10	0.139	0.022	99.25	0.7	1390	86	84	63
SH304-2 A9b ighb gl2	1	ia	74.0	14.1	0.93	0.11	0.77	3.96	5.17	0.21	0.07	0.03	0.08	0.139	n.d.	99.58	0.4	1390	n.d.	85	
SH304-2 A9b ighb gl3	1	ia	72.1	15.7	1.00	0.24	1.40	4.38	4.20	0.17	0.16	0.02	0.06	0.100	0.012	99.54	0.5	1000	48	85	106
SH304-2 A9b ighb gl4	1	ia	73.4	15.6	0.84	0.19	1.35	4.21	3.42	0.19	0.08	0.04	0.08	0.113	0.030	99.55	0.4	1130	118	84	45
SH304-2 A9b ighb gl5	1	ia	73.9	15.7	0.83	0.20	1.25	4.12	3.36	0.12	0.10	0.05	0.12	0.112	0.032	99.93	0.1	1120	129	83	41
SH304-2 A9b ighb gl6-1	1	ia	73.7	15.7	0.82	0.18	1.33	4.24	3.38	0.16	0.12	0.05	0.08	0.107	0.020	99.92	0.1	1070	81	85	69
Average			74.1	14.5	0.87	0.11	1.01	3.48	4.54	0.19	0.07	0.03	0.09	0.12	0.019	99.08	0.9	1155			
Standard deviation			1.0	1.1	0.06	0.09	0.29	0.89	0.87	0.03	0.05	0.02	0.02	0.01	0.010	0.75	0.8	142			
<i>Matrix glass in microcrystalline dacite</i>																					
SH305-1 kc g-1	1	m	77.7	13.3	0.63	0.02	0.69	2.20	4.47	0.27	0.06	0.02	0.06	0.026	n.d.	99.38	0.6	260	n.d.	75	
SH305-1 kc g-30	1	m	75.8	12.1	0.70	0.02	0.41	3.36	5.37	0.34	0.07	0.01	0.03	0.030	0.013	98.24	1.8	300	52	76	91

SH305-1 kc g-33	1	m	76.8	11.8	0.68	0.02	0.19	2.21	5.24	0.33	0.08	0.00	0.04	0.036	0.021	97.41	2.6	360	83	74	56
SH305-1a g-1	1	m	76.3	14.2	0.64	0.03	0.92	4.00	4.74	0.27	0.07	0.01	0.04	0.024	n.d.	101.28	0.0	240	n.d.	75	75
SH305-1a g-35	1	m	77.4	11.9	0.83	0.03	0.23	2.97	5.63	0.31	0.05	0.01	0.03	0.023	n.d.	99.42	0.6	230	n.d.	75	75
Average			76.8	12.7	0.69	0.02	0.49	2.95	5.09	0.30	0.07	0.01	0.04	0.03	0.017	99.15	1.1	278			
Standard deviation			0.8	1.0	0.08	0.01	0.31	0.77	0.48	0.03	0.01	0.01	0.01	0.01	0.006	1.46	1.0	53			

Sample and Spot No.	Size	Phase	SiO ₂	Al ₂ O ₃	FeO	MgO	CaO	Na ₂ O	K ₂ O	TiO ₂	P ₂ O ₅	MnO	BaO	Cl	SO ₃	Total	H ₂ O	Cl	S	D.L.	SD, S
<u>Matrix glass in glassy flow-banded dacite</u>																					
SH304-2G1g1-m1	5	m	73.5	13.9	0.91	0.04	1.31	3.96	3.30	0.22	0.07	0.01	0.09	0.089	n.d.	97.40	2.6	890	n.d.	85	85
SH304-2G1g1-m2	5	m	73.1	13.9	1.17	0.17	1.40	4.26	3.38	0.16	0.06	0.01	0.04	0.079	n.d.	97.67	2.3	790	n.d.	85	85
SH304-2G1g1-m3	5	m	73.5	13.9	1.22	0.11	1.37	4.22	3.39	0.21	0.04	0.03	0.07	0.089	n.d.	98.08	1.9	890	n.d.	85	85
SH304-2G1g1-m4	20	m	73.5	13.8	0.98	0.10	1.06	4.19	3.50	0.19	0.02	0.02	0.07	0.089	n.d.	97.59	2.4	890	n.d.	85	85
SH304-2G1g1-m5	1	m	73.6	14.0	0.87	0.04	1.30	4.15	3.46	0.21	0.04	0.00	0.07	0.084	0.008	97.87	2.1	840	34	84	139
SH304-2G1g1-m6	1	m	73.3	13.9	1.02	0.10	1.28	4.05	3.45	0.17	0.05	0.04	0.09	0.089	n.d.	97.49	2.5	890	n.d.	85	85
SH304-2G1g1-m7	1	m	73.3	13.9	1.09	0.12	1.19	3.92	3.51	0.18	0.07	0.03	0.08	0.087	0.008	97.41	2.6	870	34	84	142
SH304-2G1g1-m8	1	m	73.2	14.0	0.96	0.08	1.18	4.09	3.55	0.21	0.07	0.03	0.09	0.088	n.d.	97.55	2.5	880	n.d.	85	85
SH304-2G1g1-m9	1	m	73.7	13.8	0.89	0.04	1.18	4.17	3.59	0.18	0.05	0.02	0.09	0.088	n.d.	97.81	2.2	880	n.d.	85	85
SH304-2G1g1-m10	1	m	73.3	14.0	0.79	0.04	1.19	4.23	3.62	0.22	0.03	0.01	0.06	0.084	n.d.	97.52	2.5	840	n.d.	85	85
SH304-2G1g1-m11	1	m	73.6	14.0	0.94	0.06	1.44	4.20	3.16	0.20	0.09	0.04	0.07	0.081	n.d.	97.89	2.1	810	n.d.	85	85
SH304-2G5g1	40	m	74.3	12.5	1.18	0.10	1.15	4.76	2.61	0.24	0.02	0.00	0.07	0.075	n.d.	96.98	3.0	750	n.d.	85	85
Average			73.5	13.8	1.00	0.08	1.25	4.18	3.38	0.20	0.05	0.02	0.07	0.09	0.008	97.61	2.4	852			
Standard deviation			0.3	0.4	0.14	0.04	0.11	0.21	0.27	0.02	0.02	0.01	0.01	0.00	0.000	0.29	0.3	47			

Glass inclusions in glassy flow-banded dacite

SH304-2G1g1-g1	1	io	73.9	14.0	1.33	0.10	1.43	4.34	3.11	0.48	0.07	0.00	0.09	0.099	n.d.	98.95	1.1	990	n.d.	85	85
SH304-2G1g3-1	1	ih	73.6	14.0	0.94	0.02	1.48	4.08	3.17	0.21	0.01	0.01	0.08	0.086	n.d.	97.74	2.3	860	n.d.	85	85
SH304-2Gg4-1	1	ih	76.4	12.2	0.85	0.07	1.00	3.88	3.29	0.03	0.06	0.05	0.08	0.082	0.005	97.96	2.0	820	19	86	232
SH304-2Gg6-1	1	ip	72.9	14.5	0.54	0.01	2.47	5.59	2.26	0.13	0.06	0.03	0.06	0.081	0.010	98.59	1.4	810	38	85	132
Average			74.2	13.7	0.92	0.05	1.60	4.47	2.96	0.21	0.05	0.02	0.08	0.09	0.007	98.31	1.7	870			
Standard deviation			1.5	1.0	0.33	0.04	0.62	0.77	0.47	0.19	0.02	0.02	0.01	0.01	0.003	0.56	0.6	83			

Glass inclusion in dacite fragment in gouge

11-4 gou gr7	1	ih	63.7	17.8	2.78	0.23	3.32	4.90	2.41	1.24	0.41	0.03	0.06	0.281	0.031	97.17	2.8	2810	125	75	37
--------------	---	----	------	------	------	------	------	------	------	------	------	------	------	-------	-------	-------	-----	------	-----	----	----

Matrix glass in fragments from tephra erupted January 16, 2005

WS1-19-05 g1	20	m	70.6	14.7	2.10	0.52	2.21	4.89	2.17	0.38	0.11	0.07	0.08	0.076	n.d.	97.96	2.0	760	n.d.	75	75
WS1-19-05 g2	20	m	70.7	14.7	2.11	0.54	2.25	4.90	2.19	0.37	0.07	0.05	0.07	0.080	n.d.	98.07	1.9	800	n.d.	75	75
WS1-19-05 2-22	20	m	71.0	14.5	2.13	0.46	2.07	3.88	2.16	0.32	0.07	0.04	0.07	0.088	n.d.	96.73	3.3	880	n.d.	75	75
WS1-19-05 2-23	20	m	71.5	14.8	1.99	0.48	2.24	4.97	2.09	0.33	0.08	0.04	0.04	0.075	n.d.	98.58	1.4	750	n.d.	75	75
WS1-19-05 5-25	20	m	73.5	12.7	1.80	0.28	1.30	4.41	2.56	0.36	0.09	0.03	0.07	0.083	n.d.	97.26	2.7	830	n.d.	75	75
WS1-16-05 5-26	20	m	73.1	12.8	1.84	0.26	1.30	4.43	2.46	0.41	0.08	0.03	0.06	0.087	n.d.	96.84	3.2	870	n.d.	75	75
Average			71.7	14.0	2.0	0.4	1.9	4.6	2.3	0.4	0.1	0.0	0.1	0.1	n.d.	97.6	2.4	815			
Standard deviation			1.3	1.0	0.1	0.1	0.5	0.4	0.2	0.0	0.0	0.0	0.0	0.0	0.0	0.7	0.7	55			

Glass inclusions in fragments from tephra erupted January 16, 2005

WS1-19 gi-43	1	io	73.8	14.9	1.01	0.02	0.30	4.71	4.00	0.61	0.05	0.03	0.07	0.389	0.012	99.87	0.1	3890	47	72	97
WS1-19 gi-44	1	io	74.3	15.1	0.94	0.02	0.58	5.84	3.14	0.55	0.12	0.01	0.07	0.369	n.d.	101.05	0.0	3690	n.d.	75	75

Table 5. Major-element compositions of host dacite and small quenched inclusions from 2004–2006 Mount St. Helens dome lava.

[Oxides reported as weight percent. Compositions determined by automated electron-microprobe, sampling from 736 to 1021 points distributed across gridded areas of polished sections and compared with bulk rock X-ray fluorescence (XRF) analyses of the dacite. Rejected were analyses with totals greater than 102 percent or less than 85 percent (resulting from, for example, beam overlap with void space in the microprobe mount). Comparison of normalized average composition of host by microprobe to that by XRF shows excellent agreement (within 1 percent) for SiO₂, and Na₂O, good agreement (within 7 percent) for Al₂O₃, CaO, and K₂O, and moderate (30 percent low for MgO) to poor agreement (47–72 percent low for TiO₂, FeO, and MnO). Poor agreement attributed to undersampling of small oxide grains, many of which were likely rejected due to low totals. See Laboratory Methods for additional information on methodology.]

Sample No.	SiO ₂	Al ₂ O ₃	FeTO ₃	MgO	CaO	Na ₂ O	K ₂ O	TiO ₂	MnO	Total
<u>SH315-4 host¹</u>										
758 point average	62.11	17.54	2.82	1.36	4.83	4.30	1.25	0.34	0.04	94.57
Normalized to 100%	65.67	18.54	2.98	1.44	5.10	4.55	1.32	0.36	0.05	100.00
SH315-4 host by XRF	65.16	17.24	4.38	1.87	4.75	4.49	1.41	0.61	0.07	100.00
Correction factors ²	0.99	0.93	1.47	1.30	0.93	0.99	1.07	1.72	1.53	1.00
<u>SH315-4 inclusion³</u>										
724 point average	58.95	16.47	5.95	4.06	6.40	3.54	1.19	0.87	0.06	97.50
Normalized to 100%	60.47	16.89	6.10	4.17	6.56	3.63	1.22	0.89	0.06	100.00
Corrected analysis	60.00	15.71	8.98	5.43	6.11	3.59	1.31	1.54	0.10	100.00
<u>SH321-1 inclusion⁴</u>										
523 point average	64.31	16.99	4.30	1.85	5.09	4.07	1.23	0.52	0.05	98.42
Normalized to 100%	65.34	17.27	4.37	1.88	5.17	4.14	1.25	0.53	0.05	100.00
Corrected analysis	64.84	16.06	6.43	2.45	4.81	4.09	1.34	0.92	0.07	100.00

¹263 analyses rejected from 1,021 total points analyzed.

²Correction factors are abundance ratios of microprobe to XRF data, used to correct microprobe analyses.

³236 analyses rejected from 960 total points analyzed.

⁴213 analyses rejected from 736 total points analyzed.

Modal compositions and textures of the dacite lava

Microcrystalline dacite

The spines are composed of remarkably crystal-rich hornblende-hypersthene dacite; microbeam mapping of three microcrystalline dacite samples (SH304-2A, SH305-1A, SH315-4) yields total crystal contents that range from 69 percent to 87 percent (phenocrysts+microlites) on a void-free basis. Phenocryst content of the microcrystalline dacite averages 46.0 percent (± 4.3 percent), also on a void-free basis (table 2). The high total crystal content is a result of extensive groundmass crystallization, which produced fine-grained mosaics of microlites, residual glass, and vesicles. For consistency with previous work (Cashman, 1992) a cutoff of approximately 30 μm is used to

distinguish microlites from phenocrysts in modes. The microlite-rich groundmass texture of the 2004–2006 dacite is referred to as *microcrystalline* to distinguish it from the more typical hyalopilitic textures of the 1980s lavas.

Samples collected from spine 3 during the early stages of the eruption (table 1), when the eruption rate was high (that is, greater than 5 m³/s; Schilling and others, this volume, chap. 8; LaHusen and others, this volume, chap. 16), and from the exterior margin of the spines are relatively glassy. For example, interior sample SH304-2A has, by microbeam map analysis, approximately 45 percent phenocrysts of plagioclase, amphibole, hypersthene, and Fe–Ti oxides set in a microcrystal-rich matrix that contains approximately 33 percent microlites and 22 percent glass on a vesicle-free basis (table 2). Exterior sample SH305-1A is also relatively vesicular (37 percent) and glassy (30 percent

Table 6. Fourier-Transform Infrared (FTIR) spectrographic analyses of matrix glass in samples SH304-2G1 and SH304-2G2.

[Abs, absorbance at the indicated wavenumber (for example, 4500 cm⁻¹). Absorbance at wavenumber 2350 cm⁻¹ was below detection level of 20 ppm as CO₂. Water and hydroxyl groups all reported in weight percent; H₂Ot, total dissolved water; H₂Om, molecular water; OH⁻, dissolved water as hydroxyl groups. For data reduction purposes, standard values from Newman and others (1986) used for molar absorptivity, ε, for water in rhyolitic glass. They are ε₃₇₅₀ cm⁻¹=68; ε₁₆₃₀ cm⁻¹=55; ε₅₂₀₀ cm⁻¹=1.61; ε₄₅₀₀ cm⁻¹=1.73.]

Sample	Abs 4500 cm ⁻¹	Abs 5200 cm ⁻¹	Abs 3570 cm ⁻¹	Abs 1630 cm ⁻¹	Thickness cm	Density g/l	H ₂ Ot 3570 cm ⁻¹	H ₂ Om 1630 cm ⁻¹	H ₂ Om 5200 cm ⁻¹	OH ⁻ 4500 cm ⁻¹	H ₂ Ot ¹ 4500 + 5200 cm ⁻¹	H ₂ Ot 4500 + 1630 cm ⁻¹
SH304-2G1-s1	0.0045	0.0069	0.520	0.248	0.00372	2317	1.598	0.942	0.896	0.544	1.439	1.486
SH304-2G1-s2	0.0057	0.0070	0.672	0.307	0.00372	2317	2.066	1.167	0.909	0.689	1.597	1.855
SH304-2G1-s3	0.0041	0.0075	0.469	0.230	0.00372	2317	1.442	0.874	0.974	0.495	1.469	1.369
SH304-2G1-s4	0.0062	0.0070	0.649	0.285	0.00372	2317	1.995	1.083	0.909	0.749	1.658	1.832
SH304-2G1-s5	0.0056	0.0066	0.639	0.289	0.00372	2317	1.964	1.098	0.857	0.677	1.533	1.775
SH304-2G1-s6	0.0070	0.0090	0.837	0.369	0.0053	2317	1.806	0.984	0.820	0.594	1.414	1.578
SH304-2G1-s7	0.0080	0.0100	0.879	0.406	0.0053	2317	1.896	1.083	0.911	0.590	1.590	1.761
SH304-2G1-s8	0.0077	0.0098	0.859	0.382	0.0053	2317	1.853	1.019	0.893	0.653	1.546	1.672
SH304-2G1-s9	0.0088	0.0100	1.020	0.436	0.0062	2317	1.881	0.994	0.779	0.638	1.417	1.632
SH304-2G1-s10	0.0090	0.0110	1.028	0.462	0.0062	2317	1.896	1.053	0.857	0.652	1.509	1.706
SH304-2G1-s11	0.0049	0.0079	0.662	0.292	0.00372	2317	2.035	1.110	1.026	0.592	1.618	1.702
SH304-2G1-s12	0.007	0.0066	0.778	0.347	0.005	2317	1.779	0.981	0.637	0.629	1.267	1.610
SH304-2G1-s13	0.005	0.0070	0.645	0.315	0.00372	2317	1.983	1.197	0.909	0.604	1.513	1.801
SH304-2G1-s14	0.0064	0.0067	0.544	0.256	0.00372	2317	1.672	0.973	0.870	0.773	1.643	1.746
SH304-2G1-s15	0.008	0.0110	0.876	0.396	0.0053	2317	1.890	1.056	1.002	0.678	1.681	1.735
SH304-2G1-s16	0.01	0.0130	1.148	0.516	0.0062	2317	2.117	1.177	1.013	0.725	1.737	1.901
Average							1.867	1.049	0.891	0.648	1.539	1.698
Standard deviation							0.178	0.090	0.096	0.072	0.121	0.139
SH304-2G2-s1	0.0097	0.0137	1.069	0.484	0.0052	2323	2.345	1.312	1.269	0.836	2.105	2.149
SH304-2G2-s2	0.0084	0.0127	1.053	0.488	0.0052	2323	2.309	1.323	1.176	0.724	1.901	2.047
SH304-2G2-s3	0.0145	0.0172	1.558	0.651	0.0078	2323	2.278	1.177	1.062	0.833	1.896	2.010
SH304-2G2-s4	0.0095	0.0155	1.149	0.514	0.0052	2323	2.520	1.394	1.436	0.819	2.255	2.213
SH304-2G2-s5	0.017	0.0160	1.685	0.767	0.0078	2323	2.464	1.387	0.988	0.977	1.965	2.364
SH304-2G2-s6	0.0129	0.0172	1.601	0.723	0.0078	2323	2.341	1.307	1.062	0.741	1.804	2.048
SH304-2G2-s7	0.0092	0.0110	0.988	0.445	0.0052	2323	2.167	1.207	1.019	0.793	1.812	2.000
SH304-2G2-s8	0.0142	0.0163	1.619	0.733	0.0078	2323	2.367	1.325	1.007	0.816	1.823	2.141
SH304-2G2-s9	0.0106	0.0165	1.357	0.612	0.0078	2323	1.984	1.106	1.019	0.609	1.628	1.716
SH304-2G2-s10	0.013	0.0162	1.549	0.716	0.0078	2323	2.265	1.294	1.000	0.747	1.748	2.041
Average							2.304	1.283	1.104	0.790	1.894	2.073
Standard deviation							0.150	0.092	0.147	0.095	0.180	0.168

Table 7A. Major elements and Zr by XRF and selected trace-element analyses by ICP-MS for bulk samples from 2004–06 Mount St. Helens lava dome and sample of lava erupted in October 1986.

[Oxide abundances in wt. percent, elemental abundances in parts per million. Numbers in parentheses represent number of analyses in average (AVG) and standard deviation (SD). Complete analyses of all samples are given in Thorber and others (2007b), and additional geochemical data for bulk analyses of samples from past 500 years of eruptive activity at Mount St. Helens are summarized in Pallister and others (1992).]

Spine No.	2004-06 dacite		Glassy fragments			Roof of Spine 1		Roof of Spine 3		1986 dacite
	3-7		3	1	1	1		3		1
Sample			SH304-2G1	SH300-1A3A	SH300-1C2	SH300 (dense)		SH301		SH226
	AVG	SD				AVG(3)	SD(3)	AVG(3)	SD(3)	
XRF	(23)	(23)								
SiO ₂	64.93	0.09	66.85	64.64	64.65	63.43	0.35	63.38	0.29	63.78
Al ₂ O ₃	17.21	0.08	16.77	17.12	17.23	17.45	0.12	17.49	0.02	17.35
FeTO ₃	4.40	0.05	3.87	4.65	4.43	4.93	0.03	4.97	0.13	4.89
MgO	1.85	0.05	1.24	2.01	1.85	2.17	0.05	2.16	0.08	2.02
CaO	4.73	0.03	3.99	4.86	4.77	5.30	0.09	5.26	0.08	5.04
Na ₂ O	4.61	0.08	4.64	4.50	4.73	4.56	0.05	4.55	0.04	4.60
K ₂ O	1.42	0.02	1.83	1.34	1.44	1.24	0.01	1.27	0.02	1.37
TiO ₂	0.62	0.01	0.52	0.63	0.62	0.66	0.01	0.67	0.01	0.67
P ₂ O ₅	0.15	0.02	0.21	0.17	0.21	0.19	0.00	0.17	0.01	0.18
MnO	0.07	0.00	0.07	0.07	0.07	0.08	0.00	0.08	0.00	0.08
Total	100.00	0.00	100.00	100.00	100.00	100.00	0.00	100.00	0.00	100.00
LOI	0.09	0.10	2.21	0.41	0.35	0.06	0.03	0.25	0.15	1.16
ICP-MS	AVG	SD								
	(23)	(23)								
Ba	340	18	335	335	373	290	2	312	3	333
Be	1.35	0.11	1.50	1.30	1.70	1.20	0.00	1.30	0.10	1.42
Cd	0.10	0.09	0.07	0.07	0.09	0.04	0.00	0.08	0.06	0.07
Ce	24.61	1.05	25.70	25.40	28.10	21.75	0.49	23.80	0.10	26.00
Co	11.50	0.73	13.40	12.60	7.70	12.90	0.42	13.57	0.45	13.10
Cr	8.91	1.14	24.10	11.40	13.80	12.40	1.56	12.00	2.15	14.00
Cs	1.56	0.10	1.50	1.50	2.10	0.66	0.18	1.37	0.15	1.49
Cu	33.30	3.16	30.80	41.00	25.80	38.20	5.94	37.60	2.19	23.80
Ga	19.50	0.81	20.00	19.40	20.00	17.70	0.14	19.00	0.00	19.90
La	12.69	0.43	13.00	12.50	14.30		0.14	11.83	0.06	13.00
Li	24.66	1.98	28.30	25.00	11.90	11.45	2.05	18.43	4.15	22.70
Mn	544	23	591	581	529	561	14	590	12	618
Mo	0.75	0.09	1.10	0.69	1.50	0.82	0.04	0.78	0.09	0.95
Nb	5.38	1.26	6.40	7.00	7.60	7.75	2.76	4.50	0.20	7.02
Ni	8.28	0.97	16.90	8.10	7.00	10.20	0.85	12.73	1.94	11.40
P	616	41	720	659	690	563	15	613	6	684
Pb	7.63	0.62	7.80	7.28	8.50	5.24	0.08	6.97	1.34	7.04
Rb	33.65	1.14	32.60	31.40	41.10	23.45	3.46	29.07	0.76	32.40
Sb	0.17	0.12	0.20	0.20	0.26	0.10	0.00	0.20	0.00	<0.02
Sc	9.38	0.64	9.90	10.80	6.00	10.25	0.35	10.50	0.50	10.50
Sr	471	11	462	462	447	457	10	473	9	489
Th	2.75	0.24	2.90	2.55	3.00	2.21	0.01	2.40	0.00	2.56
Tl	0.33	0.34	0.20	0.28	0.40	0.13	0.00	0.11	0.08	0.29
U	1.05	0.11	1.20	1.10	1.20	1.06	0.01	0.97	0.01	1.07
V	75.17	6.12	90.20	83.30	42.00	87.30	3.39	86.43	2.51	86.90
Y	11.79	0.73	12.90	11.70	13.20	12.40	0.00	13.37	0.25	13.30
Zn	60.35	3.40	68.70	66.40	64.00	66.70	6.93	70.10	1.61	65.20
ED-XRF										
Zr	119	19		136				119	1	149

Table 7B. Trace-elements, by instrumental neutron activation analysis, of bulk samples from 2004–06 Mount St. Helens lava dome and sample of lava erupted in October 1986.

[Elemental abundances in parts per million except Au, in parts per billion (ppb). Numbers in parentheses indicate number of analyses in average (AVG) and standard deviation (SD). Standard deviation for SH300-1A3A and SH226 are based on multiple counts for the same element. Normalization to chondrite abundance uses chondritic composition reported by Sun and McDonough (1989). Complete analyses of all samples are given in Thornber and others (2007b), and additional geochemical data for bulk analyses of samples from past 500 years of eruptive activity at Mount St. Helens are summarized in Pallister and others (1992).]

Spine No. Sample	2004-2006 dacite Average 3-7		2004-06 dacite glassy fragments 1 SH300-1A3A		Roof of spine 1 1 SH300 (dense)		1986 dacite SH226	
	AVG (5)	SD (5)		SD	AVG (3)	SD (3)		SD
Rb	35.38	1.22	33.80	1.39	27.60	1.73	33.20	0.80
Sr	463	42	472	19.82	475	18.23	485	14.07
Cs	1.65	0.05	1.51	0.04	0.70	0.13	1.53	0.04
Ba	350	6	357	7.85	284	1.15	329	4.94
Th	2.61	0.07	2.51	0.04	2.17	0.01	2.53	0.03
U	1.23	0.02	1.26	0.05	1.11	0.05	1.20	0.04
La	11.92	0.16	11.60	0.10	10.80	0.00	12.10	0.08
Ce	24.36	0.94	22.90	0.23	23.13	0.15	25.30	0.23
Nd	12.84	0.47	12.80	0.45	12.20	0.20	13.30	0.39
Sm	2.80	0.09	2.78	0.02	2.67	0.02	2.92	0.02
Eu	0.85	0.01	0.89	0.02	0.87	0.02	0.90	0.02
Gd	1.01	1.38	2.56	0.29	2.50	0.06		
Tb	0.35	0.02	0.34	0.01	0.37	0.01	0.39	0.01
Ho	0.41	0.02	0.43	0.08	0.46	0.01	0.47	0.06
Tm	0.06	0.09	0.16	0.02	0.18	0.00		
Yb	0.99	0.04	0.98	0.03	1.06	0.03	1.12	0.02
Lu	0.15	0.01	0.15	0.004	0.15	0.00	0.16	0.003
Zr	119	15	107	10	115	2.52	143	16.16
Hf	3.10	0.10	2.95	0.04	2.99	0.08	3.28	0.04
Ta	0.35	0.01	0.37	0.01	0.36	0.01	0.40	0.01
W	0.47	0.38	0.77	0.77	0.79	0.16	0.79	0.13
Sc	8.89	0.15	9.61	0.07	10.07	0.31	9.81	0.07
Cr	8.40	0.61	12.20	0.35	12.10	0.98	10.70	0.24
Co	11.44	0.13	12.70	0.11	13.63	0.55	12.40	0.12
Ni	9.96	4.52	8.48	1.26	16.67	0.86	14.60	1.59
Zn	55.08	1.68	58.30	1.69	67.97	1.10	57.90	1.22
As	0.94	0.11	1.07	1.07	0.56	0.08	1.28	0.08
Sb	0.17	0.01	0.19	0.01	0.12	0.02	0.18	0.01
Au, ppb	4.84	8.87	0.82	0.49	8.83	5.96	0.56	0.33
Chondrite-normalized REE abundances (ppm)								
La	50.30	0.69	48.95	0.22	45.57	0.00	51.05	0.18
Ce	39.80	1.54	37.42	0.14	37.80	0.25	41.34	0.15
Pr								
Nd	27.49	1.00	27.41	0.26	26.12	0.43	28.48	0.24
Sm	18.27	0.57	18.17	0.02	17.45	0.13	19.08	0.03
Eu	14.58	0.20	15.38	0.04	14.94	0.39	15.50	0.04
Gd	4.91	6.72	12.46	0.18	12.18	0.27		
Tb	9.36	0.56	8.98	0.03	9.90	0.22	10.45	0.02
Dy								
Ho	7.25	0.27	7.60	0.11	8.15	0.15	8.32	0.09
Tm	2.49	3.42	6.27	0.05	7.15	0.08		
Yb	5.81	0.24	5.79	0.01	6.24	0.16	6.59	0.01
Lu	5.75	0.20	5.87	0.01	6.05	0.18	6.38	0.01

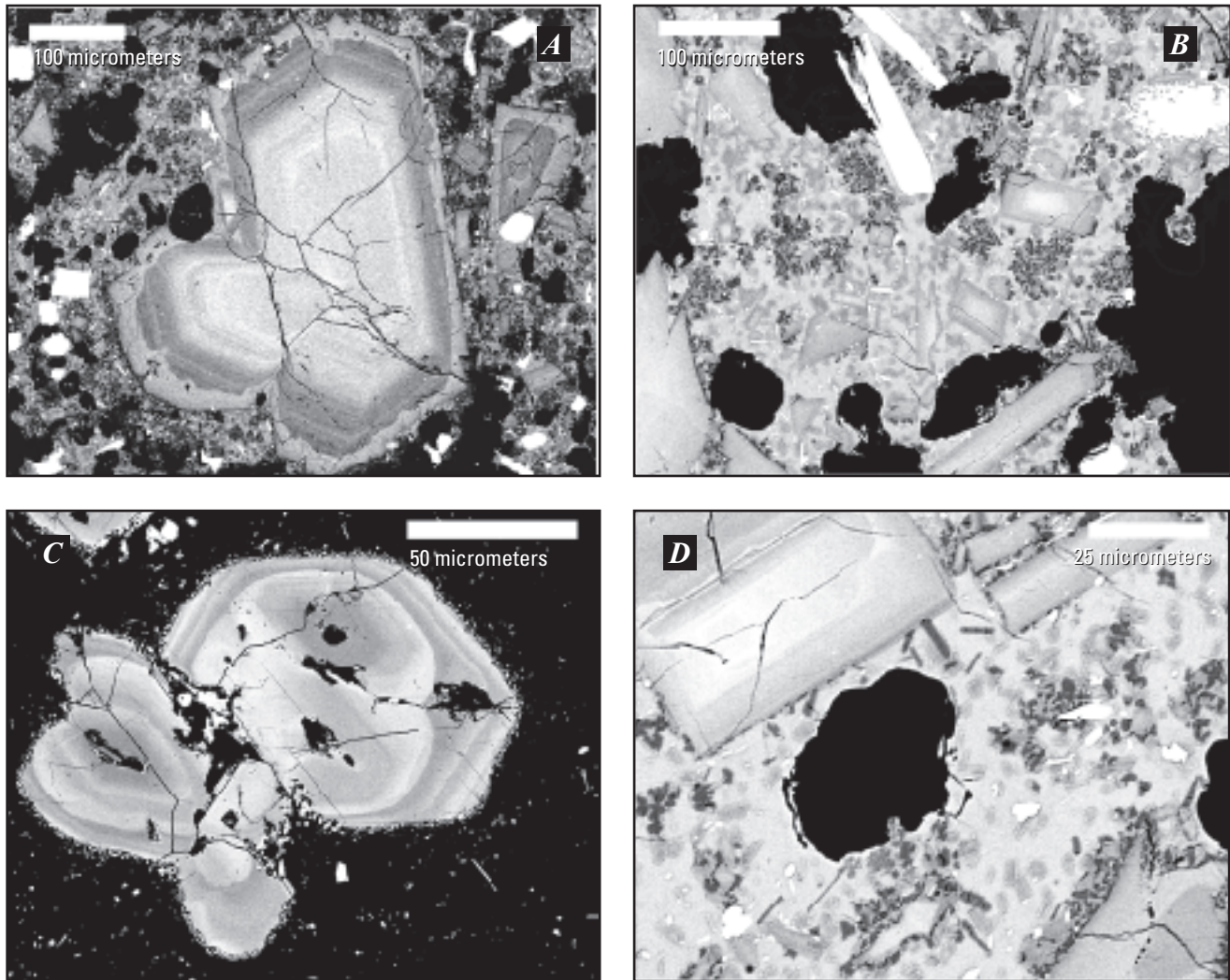


Figure 5. SEM backscattered electron images of microcrystalline dacite sample SH305-1. This early 2004 sample (eruption date, November 20, 2004, table 1) has relatively glass-rich groundmass and shows early stages of shallow cotectic groundmass crystallization. *A*, Plagioclase phenocryst. Note irregular, cusped margins, indicative of rapid growth. *B*, Groundmass. Visible in *A* and *B* are two size populations of vesicles: large (irregular) and smaller (oval to spherical). *C*, Zoned amphibole with thin (5 μm) reaction rim. *D*, Small plates of tridymite (dark gray). Magnification varies; scale bars labeled on images.

on a vesicle-free basis). However, samples erupted subsequently have less glass. For example, sample SH315-4 from spine 4 (erupted approximately April 1, 2005) has only about 13 percent glass (table 2), and samples collected later in 2005 and in 2006 have only trace amounts of glass. The presence of two populations of vesicles in the microcrystalline dacite, one with larger (100–500- μm long) irregular vesicles, and a second with small (1 μm) spherical vesicles implies continued degassing during microlite crystallization (figs. 5*A*, *B*).

A detailed look at SH305-1A shows several features that are characteristic of the 2004–2006 dacite. First, plagioclase phenocrysts commonly have overgrowth rims that are partly irregular in form and appear to have grown rapidly (fig. 5*A*). Amphibole crystals are complexly zoned and have thin, fine-grained breakdown

rims (fig. 5*C*) that average 5 μm in thickness (Thornber and others, this volume, chap. 32). The groundmass contains abundant plagioclase microphenocrysts and microlites in a glassy matrix (figs. 5*B*, 5*D*). The matrix of this sample shows the onset of very late stage cotectic precipitation of Na- and K-rich feldspar and quartz, which commonly nucleate at the margins of larger plagioclase crystals. Additionally, there is a minor component of tridymite (acicular dark gray crystals in fig. 5*D*), as also reported by Blundy and Cashman (2001) for slowly cooled samples of the March 1983 Mount St. Helens dacite.

Later-erupted samples preserve noticeably less glass in the matrix. For example, sample SH315-4 from spine 4 (erupted approximately April 1, 2005) has only about 13 percent glass (table 2; fig. 6*A*). The groundmass has

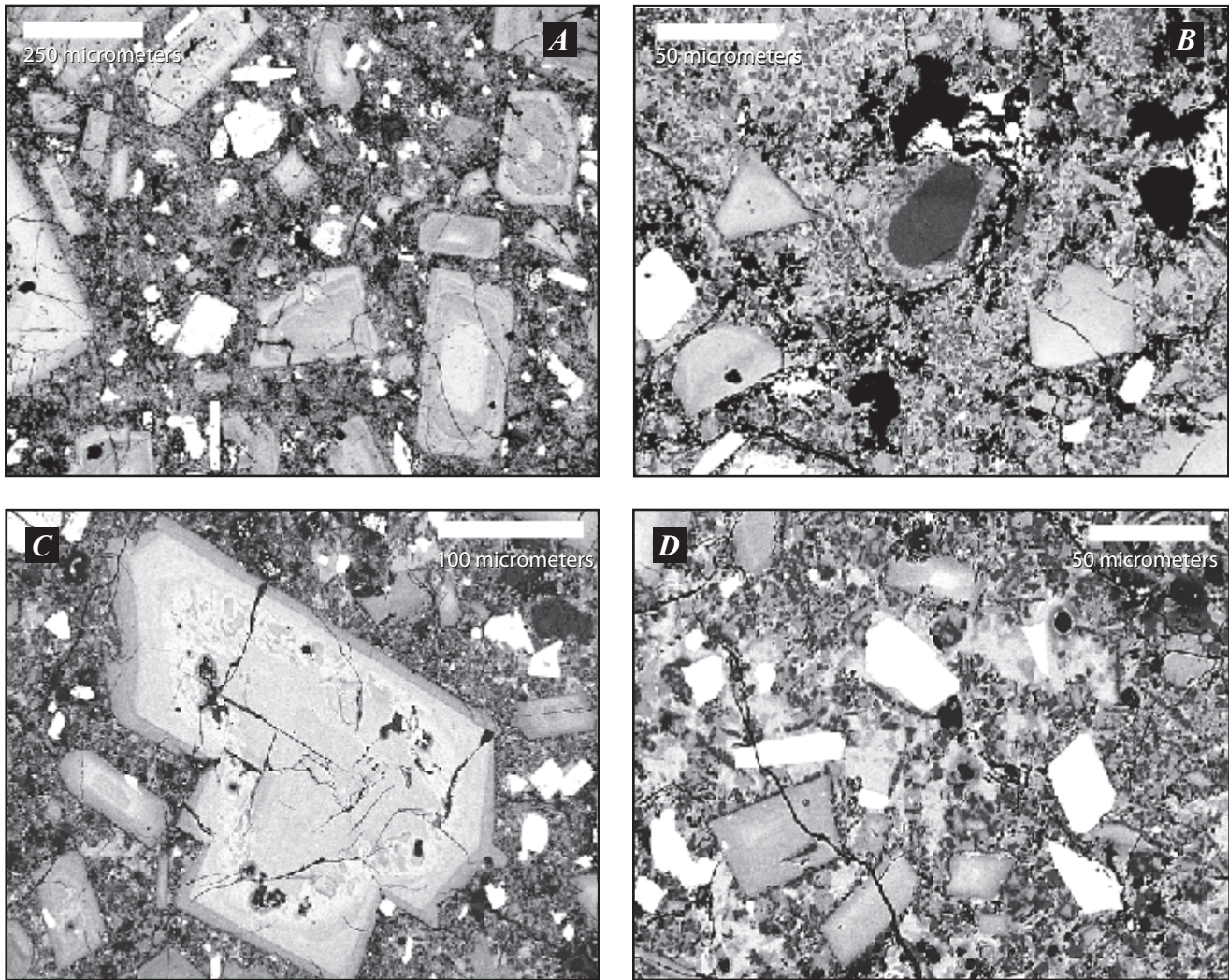


Figure 6. SEM backscattered electron images of microcrystalline dacite samples emplaced in April 2005. These samples have experienced rapid and extensive groundmass crystallization, producing a nearly holocrystalline groundmass. A and B, Sample SH315-4, erupted April 1, 2005. In B note dark-gray quartz grain (center) and micrographic intergrowth of feldspar and quartz forming the groundmass. C and D, Sample SH316, erupted April 15, 2005. Magnification varies; scale bars labeled on images.

some still-distinguishable plagioclase microlites, but they have been largely subsumed into a near-holocrystalline matrix (fig. 6B). Also common in this sample are fairly large, discrete crystals of quartz (fig. 6B). Sample SH316 from spine 5 shows similar features to samples from spines 3 and 4, with evidence of rapid rim growth on many plagioclase phenocrysts (figs. 6C) and small patches of preserved glass in a near-holocrystalline matrix (fig. 6D). Sample SH315 also contains broadly folded, vesicular, pink-colored veins a few millimeters to a few centimeters in cross section and extending for tens of centimeters across large blocks (fig. 7A). Scanning electron micrograph images from within one of the veins display an irregular network of matrix phases between the phenocrysts, formed by finely intergrown tridymite, quartz, Na- and K-rich feldspar, and void space (fig.

7B). Where larger cavities are transected by the plane of the thin section, the silica-feldspar intergrowth is seen to extend into the vesicle space (fig. 7C), exposing delicate networks of tridymite and feldspar (figs. 7D, 7E). Magnetite grains in the vein zones have undergone oxidation exsolution (fig. 7F). These features document a continuum of matrix crystallization, extending from a fluid-saturated magma into a vapor-dominated phase of crystallization.

Samples collected later in 2005 and in 2006 have only trace amounts of glass and even more extensive groundmass and vapor-phase crystallization. An examination of SH321 and SH322, from spine 6 (samples erupted on approximately August 10 and August 15, 2005, respectively), reveals groundmasses composed entirely of microlites (figs. 8A–D) and

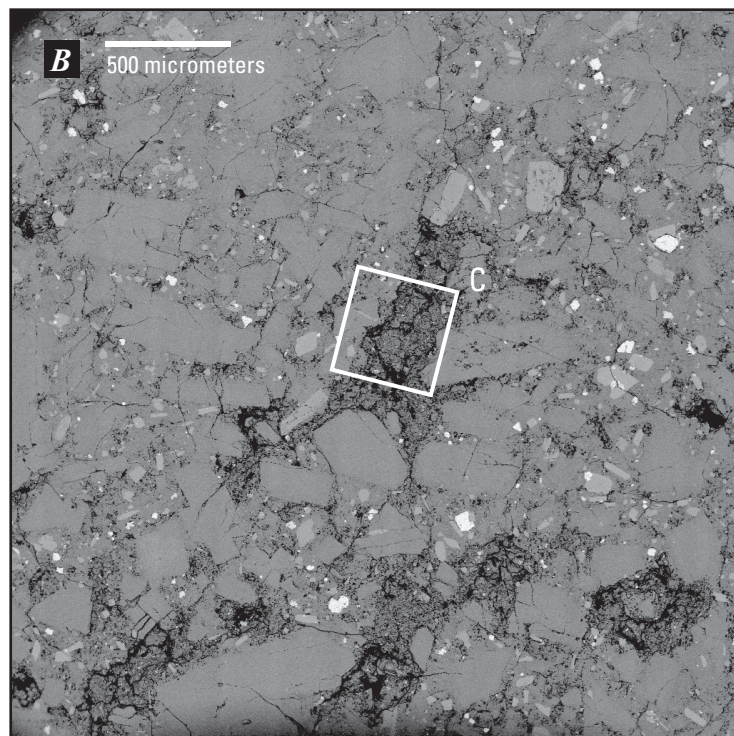
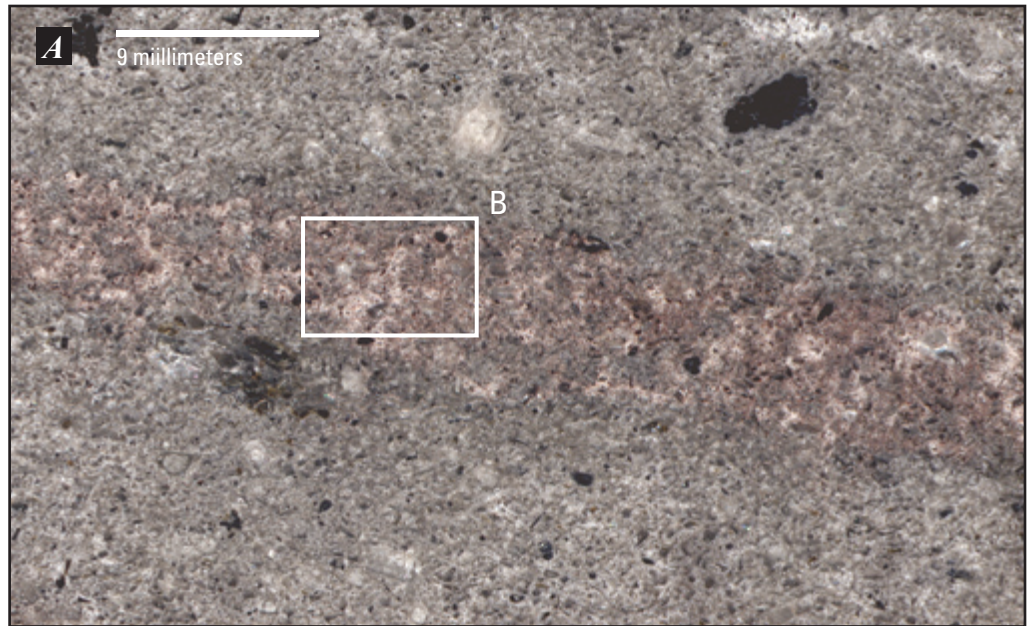


Figure 7. Photograph and SEM backscattered-electron (BSE) images of microcrystalline dacite sample SH315-5. Sequence shows progressive increase in magnification, and locations are mapped on preceding images. A, Polished thin section, 5 cm in long dimension, showing pink-colored vesicular vein. B and C, BSE images showing network of fine-grained microlite-rich matrix between phenocrysts. D and E, BSE images showing phases identified by morphology and EDS analysis: Fsp = Na+K-rich feldspar; Mt = titanomagnetite; Opx = orthopyroxene (hypersthene). F, BSE image of titanomagnetite grains in the vein zone showing development of oxidation-exsolution lamellae.

consisting of graphic intergrowths of a “granite minimum” assemblage of sodic plagioclase (An_{20–30}), quartz, tridymite, and a more potassic feldspar (anorthoclase to sanidine). Quartz and the feldspars occur as subhedral crystals within the intergrowths. Tridymite occurs within the graphic intergrowths and protrudes into vesicle space (fig. 8A), attesting to crystallization from both melt and fluid phases. Microprobe analyses of representative groundmass phases are given in table 3, and many are keyed to figure 8.

Cristobalite is a common groundmass phase in samples from each of the spines. It displays a characteristic microbotryoidal texture and commonly fills vesicles and interstices in the dacite, as well as within rare diktytaxitic quenched inclusions. The occurrence is indicative of late-stage vapor-phase crystallization, similar to that described for cristobalite in the 1980 Mount St. Helens cryptodome (Hoblitt and Harmon, 1993).

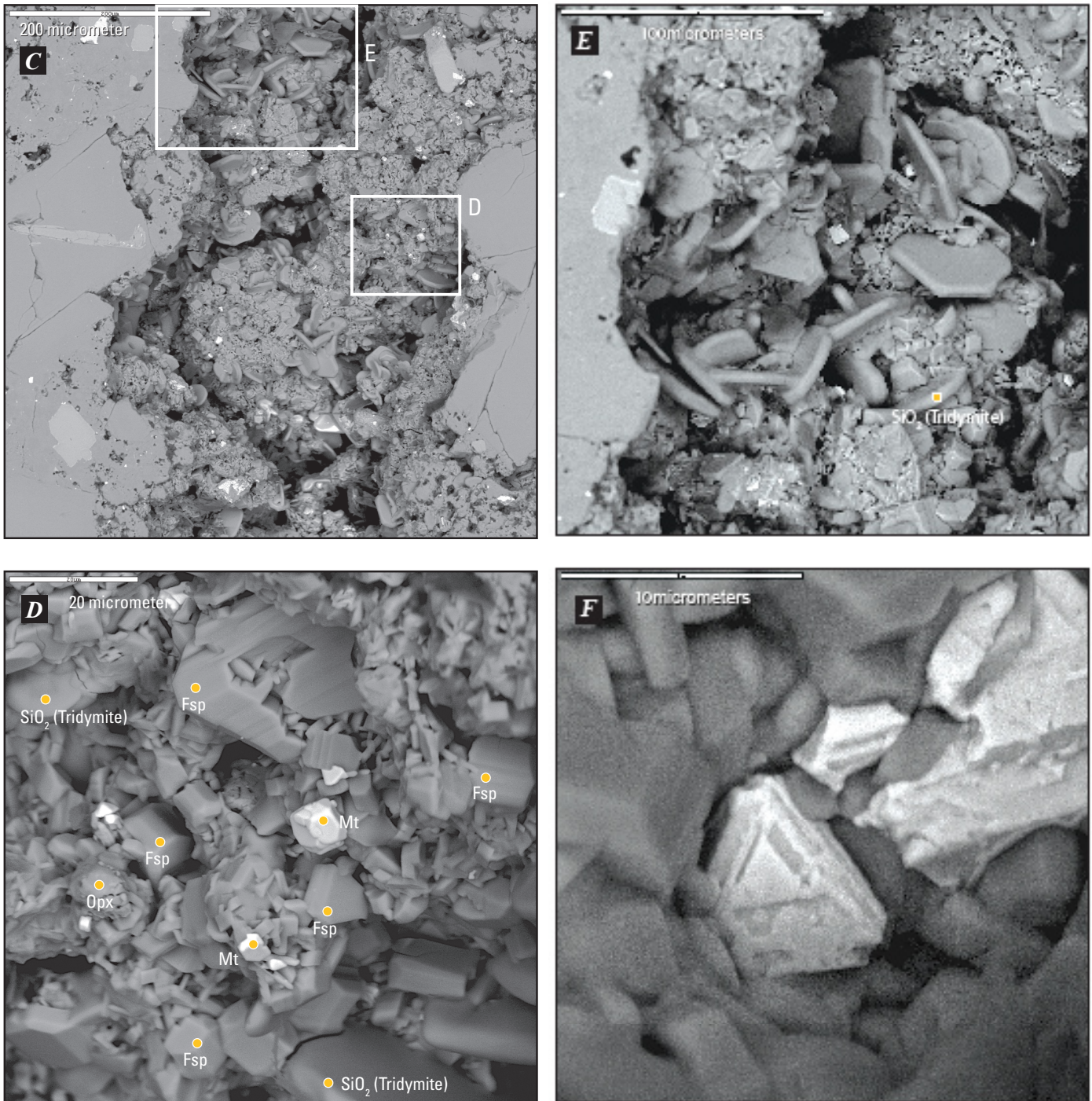
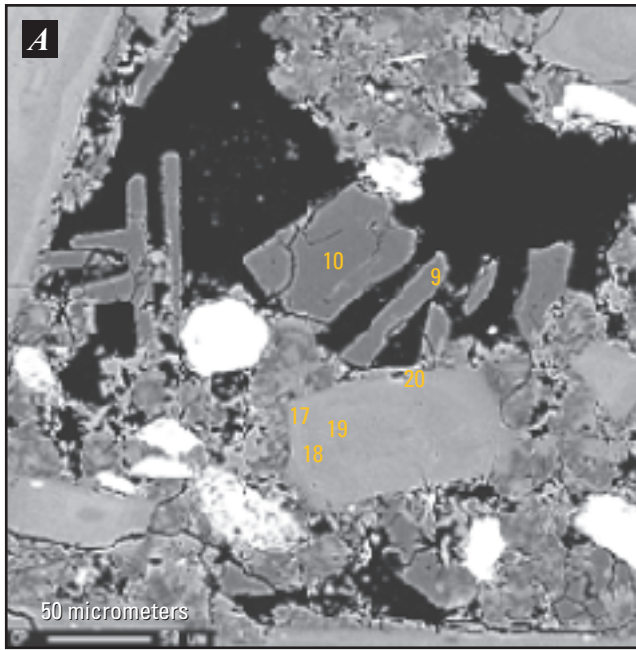
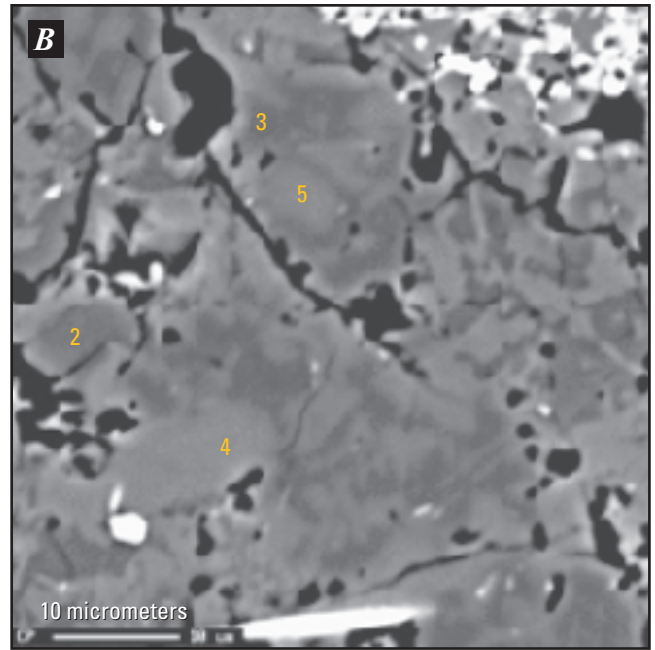


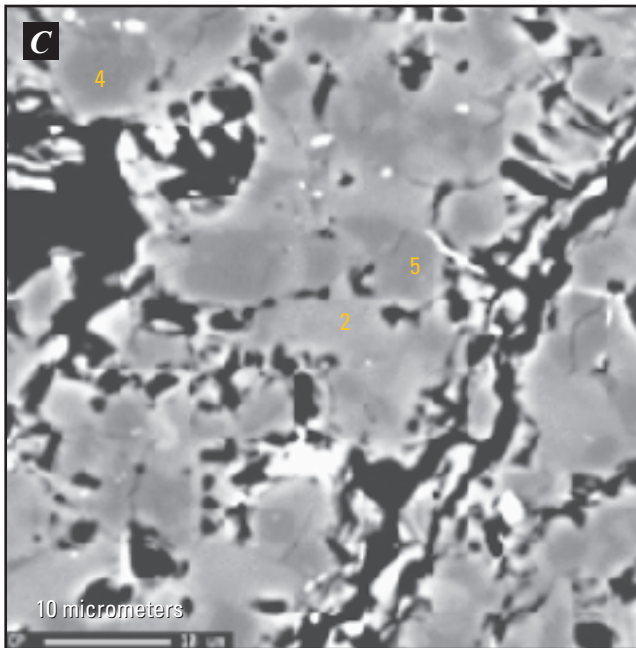
Figure 7. Photograph and SEM backscattered-electron (BSE) images of microcrystalline dacite sample SH315-5. Sequence shows progressive increase in magnification, and locations are mapped on preceding images. A, Polished thin section, 5 cm in long dimension, showing pink-colored vesicular vein. B and C, BSE images showing network of fine-grained microlite-rich matrix between phenocrysts. D and E, BSE images showing phases identified by morphology and EDS analysis: Fsp = Na+K-rich feldspar; Mt = titanomagnetite; Opx = orthopyroxene (hypersthene). F, BSE image of titanomagnetite grains in the vein zone showing development of oxidation-exsolution lamellae.



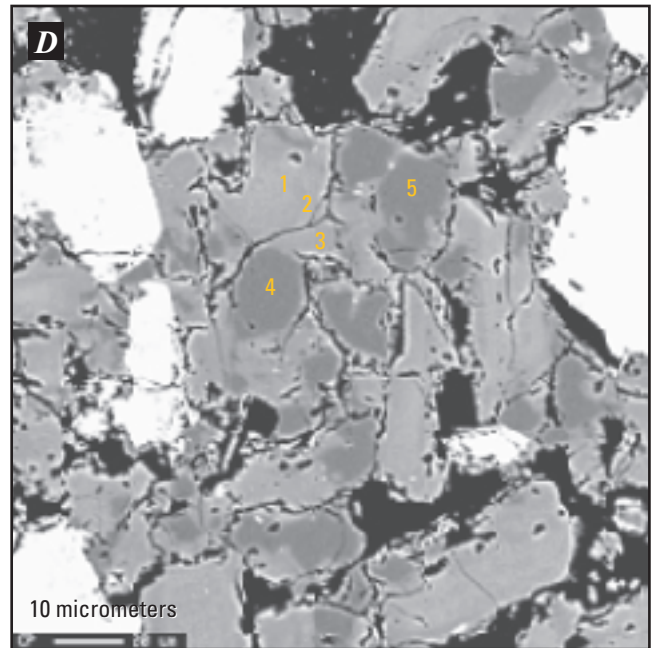
SH322-1-b



SH322-1-d



SH321-C-7b



SH321-C-7d

Figure 8. SEM backscattered electron images of microcrystalline dacite samples, documenting continued matrix crystallization. Microprobe analysis points keyed by number to table 4 (final suffix numbers in sample number list of table 3 refer to locations shown here). A and B, Sample SH322-1. C and D, Sample SH321-C. Minerals probed include tridymite with approximately 1 percent Al_2O_3 (A, 9–10; B, 2), quartz with less than 0.7 percent Al_2O_3 (B, 3; C, 4; D, 4–5), $\text{An}_{19-39}/\text{Or}_{3-9}$ plagioclase microlites (B, 4; D, 1–3; C, 2) and $\text{An}_{33-36}/\text{Or}_{1-4}$ plagioclase microphenocryst (A, 17–20), anorthoclase (B, 5), and cristobalite with more than 3 percent Al_2O_3 (C, 5).

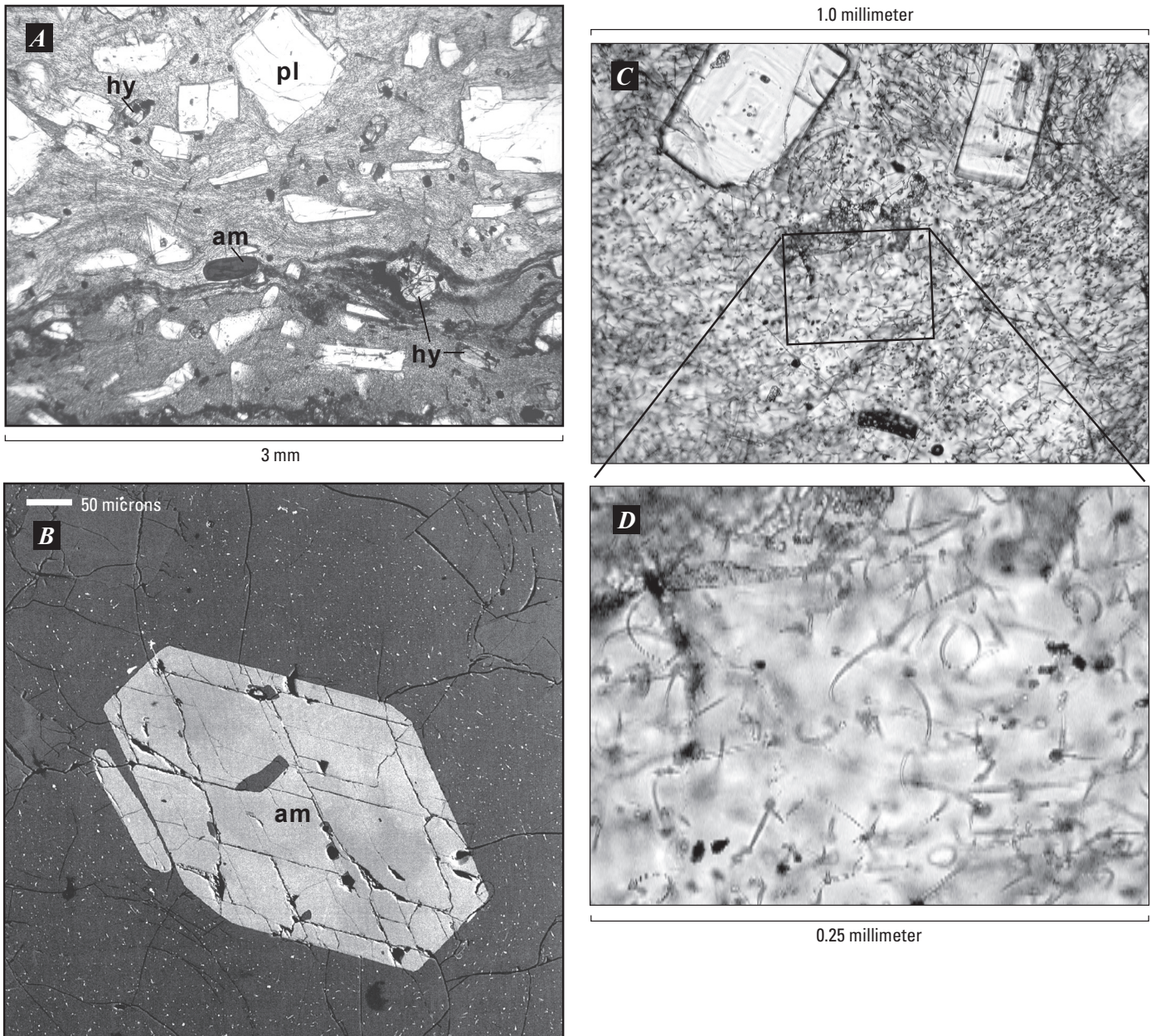


Figure 9. Photomicrographs and SEM backscattered image of glassy fragment SH304-2G1, collected on November 4, 2004. A, Phenocrysts of plagioclase (pl), hypersthene (hy), and amphibole (am) lie within a flow-foliated groundmass marked by dark bands bearing micron-size oxides. B, Microlites of hypersthene and oxides appear as bright specks in backscattered images, and subhedral to euhedral amphibole microphenocryst lacks reaction rims. C and enlargement D, Glass-rich matrix is peppered with submicron-size curvilinear hypersthene microlites and oxide grains.

Glassy dacite

The dredge haul from spine 3 on November 4, 2004, (SH304 sample series, Thornber and others, 2007b) contained principally blocks of still-hot, pink to gray, microcrystalline dacite. However, the haul also contained several small (2–5-cm diameter) dark glassy dacite fragments. Most of these have bulk compositions, phenocryst assemblages, Fe–Ti oxide temperatures, and

textures that indicate they are derived from uplifted parts of the 1980–1986 lava dome. However, one flow-banded glassy fragment (SH304-2G) has characteristics that suggest it may be juvenile (for example, overlapping Fe–Ti oxide temperature and similar bulk composition compared to the microcrystalline dacite). Sample SH304-2G is a hornblende-hypersthene dacite with 72 percent glass (fig. 9, table 2). The ratio of K_2O in the glass compared to that of the whole rock is indicative

of a glass content of only 54 percent and suggests that the sample is enriched in glass and depleted in crystal components (table 2), such as would occur by flow segregation or filter-pressing, an effect that is consistent with the flow-banded character of the fragment (fig. 9A). Although there is some uncertainty in establishing that this sample is juvenile, it is investigated in more detail here as a possible analogue for the melt phase of the 2004 magma prior to the extensive groundmass crystallization. Unlike the amphibole phenocrysts in the microcrystalline dacite, which have reaction-rim thicknesses that cluster at about 5 μm (Rutherford and Devine, this volume, chap. 31; Thornber and others, this volume, chap. 32), the amphibole phenocrysts in SH304-2G lack reaction rims (fig. 9B), indicating more rapid ascent, as might be expected during the earliest phase of the eruption. The glass in this sample contains swarms of very small (less than 1 μm diameter) hypersthene microlites (figs. 9C, 9D), similar to those found in the outer zones of plagioclase phenocrysts in the 2004–2006 dacite (Streck and others, this volume, chap. 34).

Inclusions

Inclusions in volcanic rocks provide glimpses of country rock surrounding magma reservoirs and conduits, plutonic equivalents or cumulates from host magmas, quenched blebs of other magmas, and potentially even partially melted source rocks for the magmas (Bacon, 1986; Costa, 2002; Jackson, 1968; Smith, 2000). Mount St. Helens dacites contain a rich suite of inclusions, consisting primarily of dioritic to gabbroic plutonic rocks, and the 2004–2006 lava dome is no exception.

Plutonic and metamorphic inclusions

The 2004–2006 dacite contains relatively abundant medium-grained gabbroic to dioritic inclusions as well as minor banded and granoblastic amphibolite inclusions. They are present in both dome lava and gouge samples; we estimate their abundance at 1–5 percent. Although not yet studied in detail, in hand sample the inclusions appear to be similar to the gabbroic and metamorphic inclusions that make up 3–5 percent of the 1980–86 lava dome (Heliker, 1995; Pallister and others, 1991). We previously thought that some of the gabbroic inclusions represented cumulates from the Mount St. Helens magma reservoir, but U–Pb ion-probe zircon ages of about 25 Ma for several samples (our unpublished SHRIMP data) suggest that many of these may instead be derived from a Miocene gabbroic to quartz diorite

intrusive complex inferred from gravity data to underlie the volcano (Williams and others, 1987).

Dacite inclusions

Some samples collected from the later spines of the 2004–2006 eruption contain small (1–5 cm) inclusions of dacite with slightly different textures or degrees of alteration compared to the host dacite. Petrographic examination and electron microprobe analyses of one of these inclusions in sample SH321-C shows little difference in mineralogy or composition across the inclusion boundary. Another (SH316-1A) has a bulk composition distinct from the host dacite, with 63.4 percent SiO_2 , and it likely represents a xenolith entrained in the conduit magma and derived from the root of the 1980–86 lava dome. We suspect that many such “dacite-in-dacite” inclusions are fragments of shallow conduit lava and wall rocks, incorporated as the conduit shifted slightly to feed subsequent spines. Consistent with this idea, an examination of inclusions in the gouge carapace and variations in bulk composition of the gouge (Cashman and others, this volume, chap. 19) indicate that the conduit margins incorporated a range of crater floor rocks as the gouge formed.

Quenched magmatic inclusions

Two small (<1-cm diameter) inclusions, composed of diktytaxitic networks of plagioclase and amphibole crystals and containing variable amounts of glass and void space, were found in samples SH315-4 (figs. 10A, 10B) and SH321-A. As magma mixing has been involved in the evolution of magmas erupted at Mount St. Helens during the past 4,000 years (Pallister and others, 1992; Smith and Leeman, 1996) and has been implicated as a trigger for explosive eruptions (Pallister and others, 1996), we searched the 2004–2006 rock collection for additional examples, and we examined these two inclusions in detail. Our search indicates that although dacite-in-dacite inclusions are relatively common, quenched inclusions are exceedingly rare in the suite of 2004–2006 samples. Of the approximately 500 kg of samples collected to date (Thornber and others, 2007b), we have found only the two small quenched inclusions, with a total mass less than 5 g.

A more-detailed examination of inclusion sample SH315-4 reveals elongate and hopper-shaped crystals of amphibole and plagioclase (figs. 10C, 10D), as would be produced by rapid growth during undercooling of a hotter and more mafic magma in the dacite host magma. The amphiboles are high in Al_2O_3 (to 14 percent)

and they lack reaction rims, except at the margins of the inclusion, where they reacted with the host dacite during decompression to produce thin breakdown rims (Thornber and others, this volume, chap. 32). Plagioclase phenocrysts have normally zoned An_{60-40} cores bounded by cusped dissolution zones, which are rimmed by much more sodic plagioclase (to An_{20} , Or_9). These sodic rims extend into the 75–76 percent SiO_2 rhyolitic matrix and groundmass glass as angular and hopper-form crystals (figs. 10D, 10E). Cristobalite, with a characteristic microbotryoidal texture, is relatively abundant as a late, vesicle-filling, vapor-phase product.

To determine the bulk compositions of the inclusions, we used a microprobe to analyze 736 and 960 points distributed over the polished surface of each of the two inclusions and 1021 points over a similar area of the host dacite (fig. 10A; table 5). Averages of these analyses reveal that the inclusion in sample SH315-4 is andesitic (60.0 percent SiO_2), consistent with the relatively high An content of plagioclase cores. It is regarded as a bleb of a more mafic magma that mingled with the dacite at some point in the past (see “Discussion”). The second

inclusion, SH321-1, has a bulk composition that overlaps with the host dacite, at 64.8 percent SiO_2 (table 5). However, this sample has a similar quench texture and phenocryst assemblage to the inclusion in SH315-4. It probably represents an entrained bleb of hotter dacite that quenched in the cooler host dacite. However, we cannot rule out the possibility that formerly it was a more mafic magma that quenched in the dacite and then accumulated late-stage rhyolite melt in its matrix through filter pressing (to account for its higher silica content). Quenched inclusions are often heterogeneous in composition due to the effects of post-entrainment crystallization (Bacon, 1986). During crystallization of a more mafic inclusion in a cooler and more silicic melt, the melt reaches vapor saturation; it vesiculates, and pressure in the inclusion increases. This process may force residual melt toward the margins of the inclusion as the interior gains void space (vesicles). Thus, inclusions may autofractionate, some parts gaining high-silica residual melt and some parts losing residual melt.

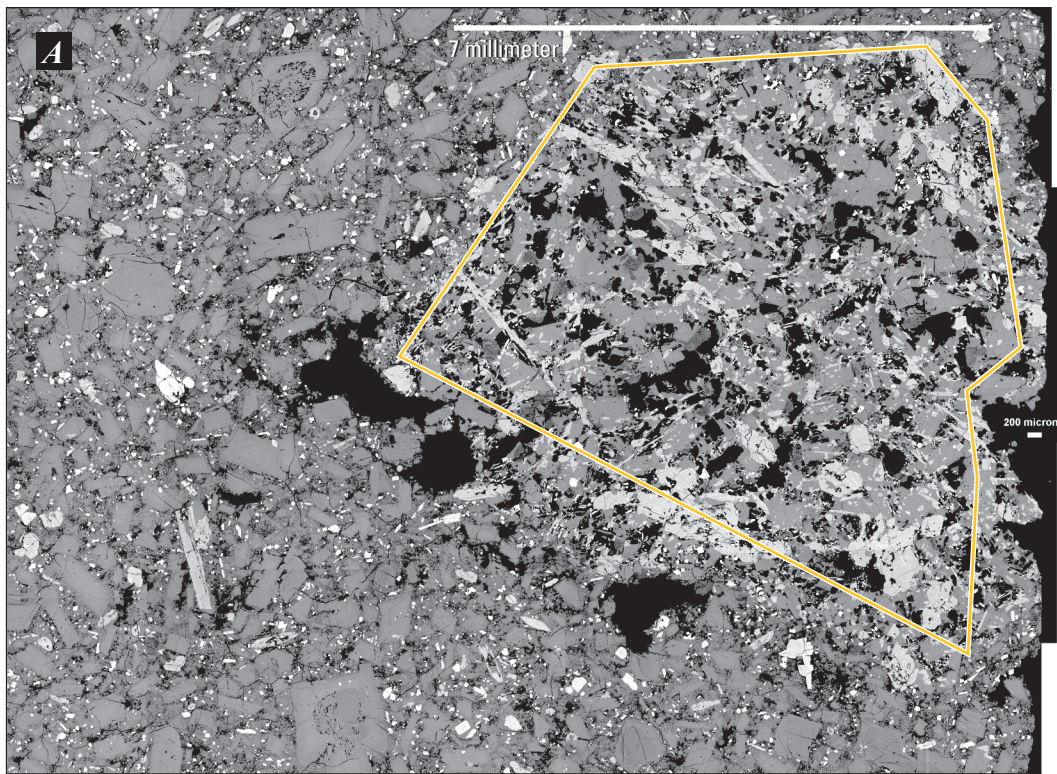
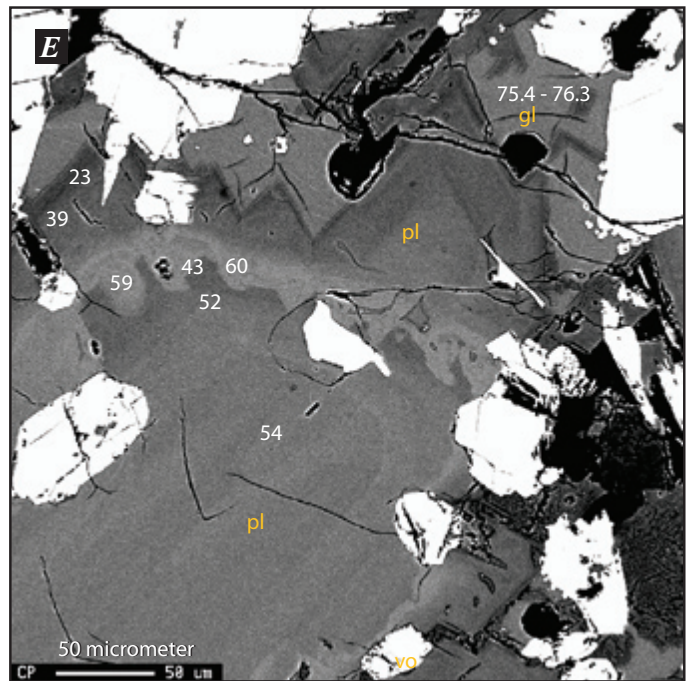
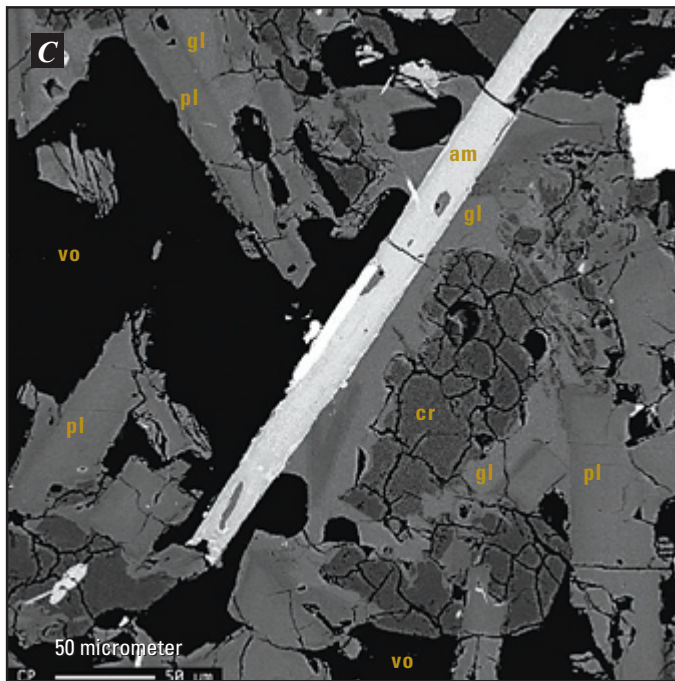
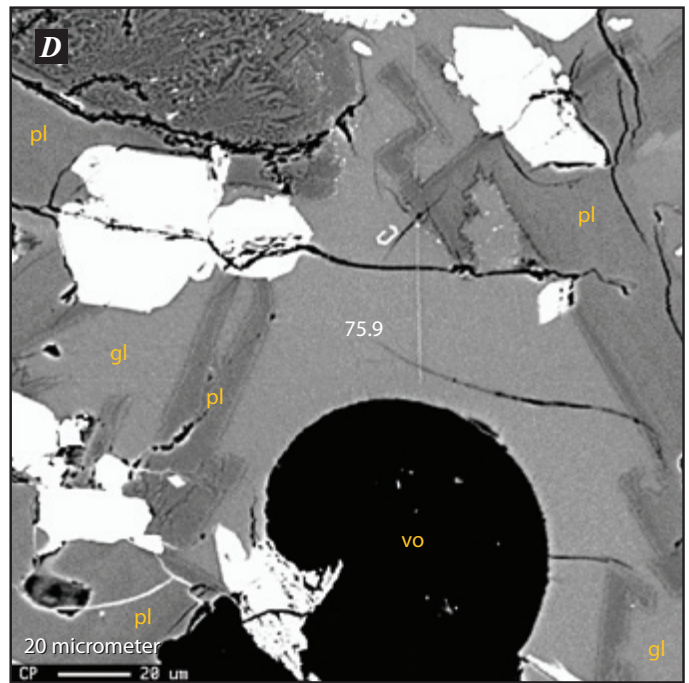
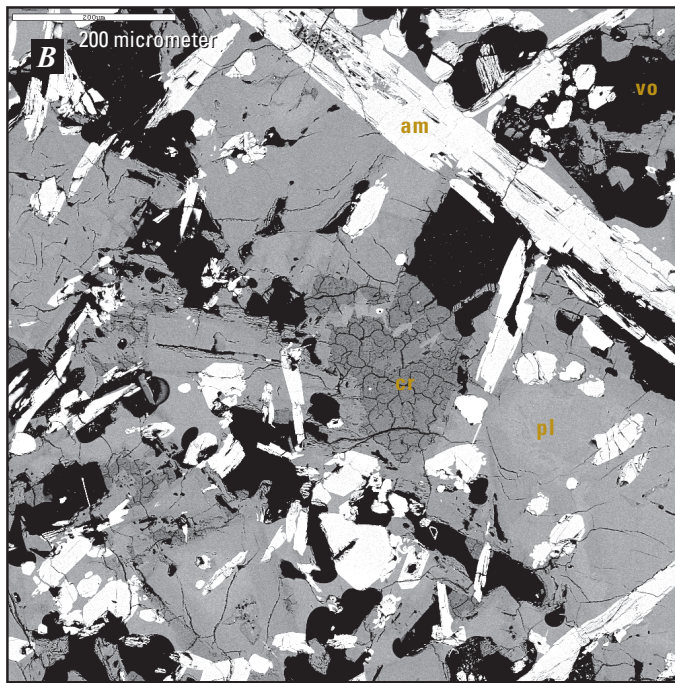


Figure 10. SEM backscattered-electron stage raster-map images of sample SH315-4. A, Composite of 24 smaller images, shows a mafic (60 percent SiO_2) quenched inclusion at upper right, with acicular amphiboles (light gray) and glassy vesicular groundmass. Irregular box encloses an area that was analyzed using a grid pattern to determine inclusion’s bulk composition (table 5). B, Enlargement of inclusion, showing diktytaxitic texture (visible also in A) and void-filling cristobalite (cr) with microbotryoidal texture. C, D, and E, differing views and magnification showing cristobalite (in image C), elongate and hopper crystals of amphibole and plagioclase (C,D,E), brown high-silica rhyolite glass (D, E) and irregular dissolution and overgrowth textures in plagioclase (E). Numbers in images D and E refer to An content of plagioclase and percent SiO_2 in glass (the latter determined by broad-beam microprobe analysis). Abbreviations: am, amphibole; cr, cristobalite; pl, plagioclase; gl, glass; vo, void space,



Compositions of matrix phases and oxides

Silicate minerals

Matrix silicate minerals include hypersthene, plagioclase, anorthoclase, quartz, tridymite, and cristobalite. The compositions of phenocrysts in the dacite are the subject of other reports in this volume

(Rutherford and Devine, chap. 31; Thornber and others, chap. 32; Streck and others, chap. 34; Kent and others, chap. 35). Here we focus only on the compositions of mineral grains in the microcrystalline groundmass of samples—grains that have textures indicative of late and shallow crystallization. These include microlites (grains <30 μm in diameter), matrix silica phases, and edge compositions of plagioclase phenocrysts. Compositions of these minerals are listed in table 3, and textures of

the matrix phases are illustrated in figures 5 through 8. Cristobalite is a common minor phase in all but the most glassy dome rocks. The cristobalite grains have a distinctive botryoidal texture and multiple contraction fractures. They commonly occur at the margins of irregular void space, indicating deposition from a late-stage, silica-rich vapor phase. This occurrence is similar to that seen in the 1980 cryptodome (Hoblitt and Harmon, 1993). Bladed crystals of tridymite are present in low abundance in most samples, although they are common in one of the samples, SH309-1. Quartz microlites occur as anhedral intergrowths with anorthoclase and sodic plagioclase, in some cases forming a patchy texture extending into small glass pools at the margins of plagioclase grains, which have experienced rapid edge growth. The compositions of plagioclase microlites and the final few microns of some phenocryst rims extend to An₂₀, well below the average rim composition of An₃₅ measured in hundreds of zoning profiles (Rutherford and Devine, this volume, chap. 31; Streck and others, this volume, chap. 34) and thought to represent the late stages of plagioclase equilibration at depth. A second feldspar, which ranges from anorthoclase to sanidine in composition with as much as 43 percent Or component (table 3), is also present in the matrix of some samples, where it is intergrown with sodic plagioclase and quartz, forming a “granite minimum” assemblage (Tuttle and Bowen, 1958).

Glasses

Microprobe analyses of matrix glass and glass inclusions reveal mostly dry high-silica rhyolite compositions (table 4). Most of our analyses of matrix glasses come from early phases of spine 3. In subsequent samples, matrix glass occurs only as thin films that are difficult or impossible to analyze with the electron microprobe without exciting nearby mineral grains. Available matrix glass compositions are all rhyolitic, ranging from 73 to 78 percent SiO₂ and containing <0.5 to 2.2 wt. percent H₂O (fig. 11). Most glass inclusions also have low water-by-difference values. A single inclusion in amphibole from SH304 has about 3.6 percent H₂O (by difference), all others are <3 percent and many have <0.5 percent H₂O. Secondary ion mass spectrometric (SIMS) analyses of glass inclusions in samples SH305 and SH315 range from 0.03 to 0.20 wt. percent (Jon Blundy, written commun., 2005), confirming the dry character of the inclusions.

Two sections of the glassy fragment SH304-2G were analyzed using FTIR spectroscopy. These measurements of total dissolved water in the matrix glass of sample

SH304-2G2, based on the intensity of the absorbance at 3570 cm⁻¹, yielded 1.9±0.18 weight percent H₂O (16 spots, table 6) with a range from 1.4 to 2.1 weight percent, overlapping the microprobe water-by-difference value reported here for the same sample (fig. 11). Total water in matrix glass of SH304-2G1 is 1.7±0.14 wt. percent on the basis of summation of water dissolved as hydroxyl groups determined from the absorbance peak at 4500 cm⁻¹ and molecular water determined from the intensity of the absorbance peak at 1630 cm⁻¹, in agreement with the value determined from the 3570 cm⁻¹ peak. Total dissolved water concentration in the matrix glass of sample SH304-2G2, estimated from the measured intensity of the absorbance peak at 3570 cm⁻¹, is 2.3±0.15 percent (10 spots, table 6) and ranging from 2.0 to 2.5 percent. Total dissolved water in SH304-2G2 matrix glass, determined from summation of water dissolved as hydroxyl and molecular components, is 2.1±0.17 percent, in agreement with the value from the 3570 cm⁻¹ peak (table 6).

In matrix glass from samples SH304-2G1 and SH304-2G2, the concentration of dissolved water present as molecular H₂O slightly exceeds that of water dissolved as hydroxyl groups (table 6). The observed water speciation in SH304-2G matrix glasses is in contrast to that observed in rapidly quenched (cooling by hundreds of degrees per minute) experimental glasses or in silicate melts at high temperature and pressure with similar total dissolved water concentrations (Dixon and others, 1995; Mandeville and others, 2002; Nowak and Behrens, 1995; Shen and Keppler, 1995; Silver and Stolper, 1989; Sowerby and Keppler, 1999) and most likely reflects species reequilibration during slower cooling and magma ascent. In all acquired spectra from SH304-2G1 and SH304-2G2 matrix glass, a CO₂ absorbance peak above background was not observed. Dissolved CO₂ concentration is below our detection limits (<20 ppm).

Most matrix glasses and glass inclusions have sulfur abundances less than detection limits (70–86 ppm, table 4). However, four glass inclusions from dacite erupted in October 2004 have between about 80 and 130 ppm S, and one inclusion contains about 250 ppm S (table 4, fig. 12). Chlorine abundances in glass inclusions reach a high of 1450 ppm and average 829±309 ppm in microcrystalline sample SH305-1 and 1155±142 ppm in microcrystalline sample SH304-2A9b. Chlorine abundance in matrix glasses averages 278±53 ppm in the high-silica rhyolite glass of the microcrystalline dacite; in contrast, it averages 852±47 ppm in low-silica rhyolite glasses from the flow-banded glassy sample SH304-1G and in glassy fragments from the January 16, 2005, tephra. As the high-silica rhyolite is a differentiation

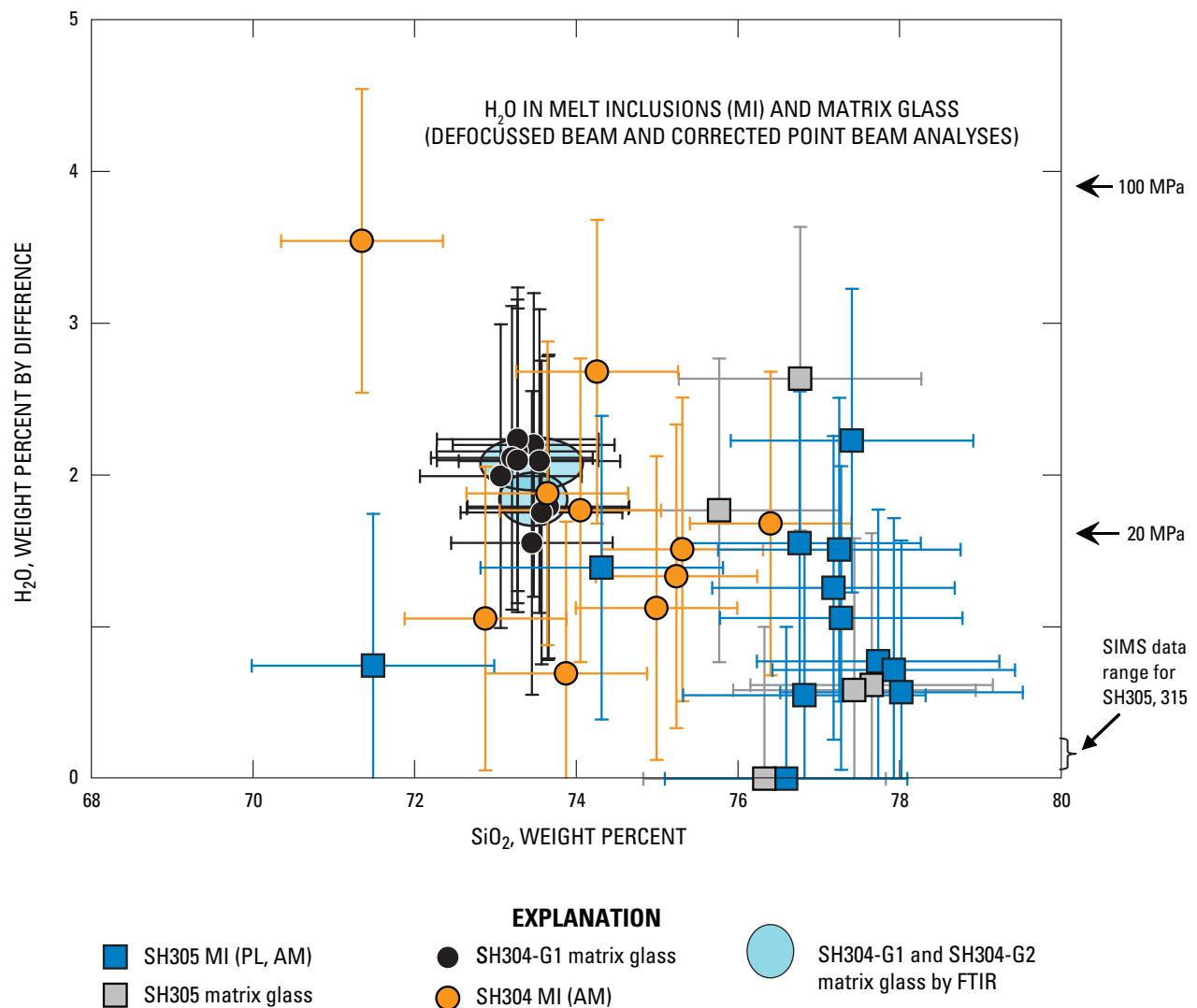


Figure 11. Abundance of H₂O in matrix glass and glass inclusions from spine 3, determined by differencing the totals of microprobe analyses from 100 percent and plotted against SiO₂. Circled field represents average and standard deviation for FTIR analyses of matrix glass in SH304-2G-1 and SH304-2G-2, which overlap with microprobe analyses of same sample. Concentrations of water at saturation in silicate melts at 20 and 30 MPa (Moore and others, 1995) are shown for comparison, as is range of secondary ion mass spectrometer (SIMS) data for matrix glass (J. Blundy and K. Cashman, written commun., 2005).

product of decompression-driven matrix crystallization, the lower Cl in these glasses is consistent with very shallow degassing of Cl during the latest stages of solidification, accompanied by development of fracture permeability in the conduit (Edmonds and others, this volume, chap. 27).

Oxides

Equilibrium temperatures and oxygen fugacities were calculated using a spreadsheet routine (Lepage, 2003), which yields results from multiple solution models for the Fe–Ti exchange thermometer and oxygen barometer (Andersen and Lindsay, 1988). Results

calculated using the solution model of (Stormer, 1983) are most consistent with experimental calibrations and are given in table 8 and displayed in figure 13. Only analyses of touching Fe- and Ti-rich oxide pairs were used for thermobarometry and individual analyses of oxide minerals in the dacite are given in the appendix. Typically 5 to 25 analyses were made of each grain pair. For unzoned grains or for grain pairs that were too small to demonstrate zoning, the average compositions of each phase are plotted, along with error bars for temperatures and fO_2 (figs. 13A, 13B). The error bars were calculated from the maximum and minimum of the ± 1 standard deviation ranges for Ti and Fe in each grain pair. As shown in figure 13C, all of the grain pairs used

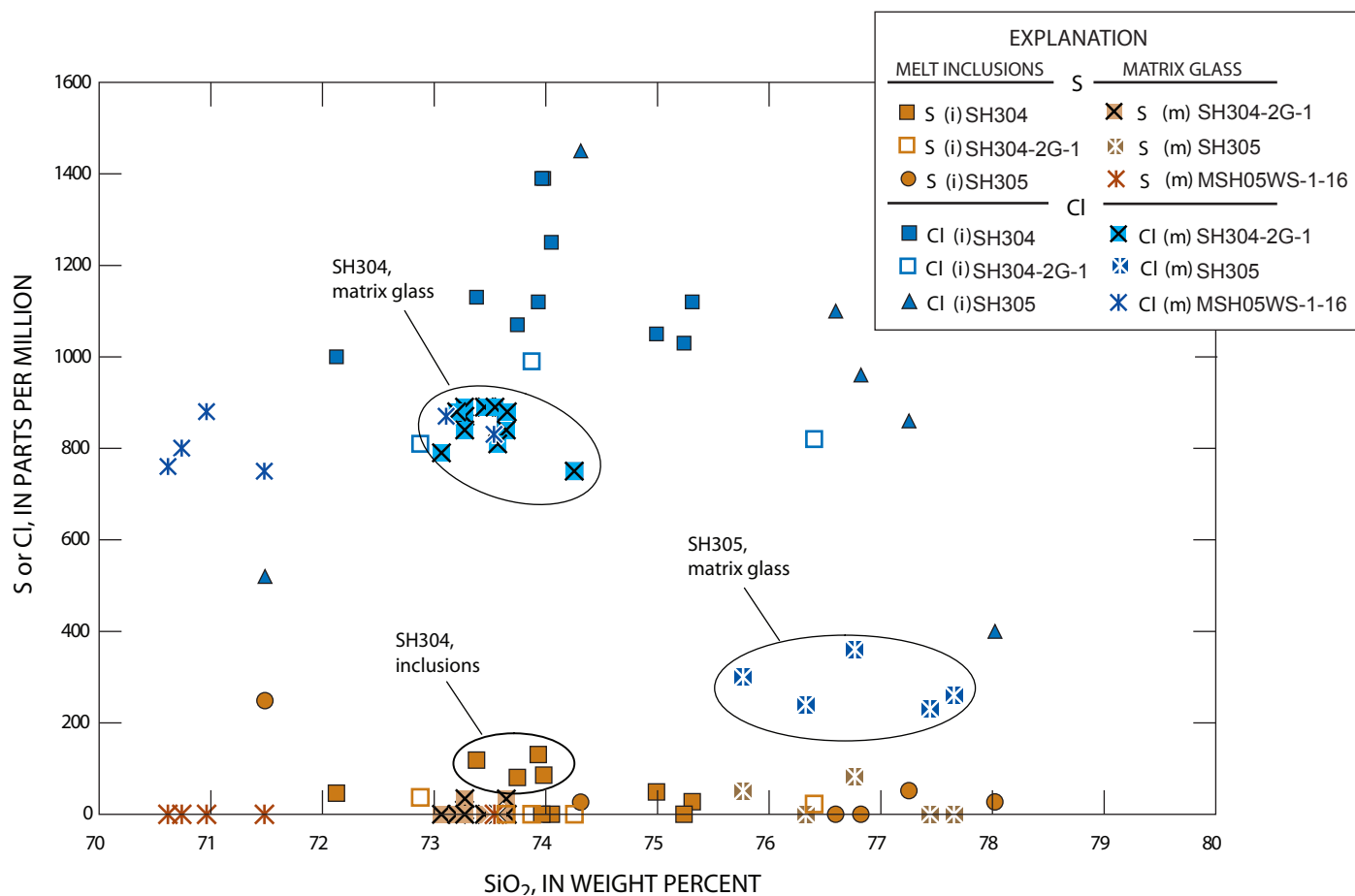


Figure 12. Abundance of S and Cl in matrix glass and glass inclusions from spine 3 plotted as function of SiO₂. Note low concentrations for S in matrix glass and most glass inclusions. Only glass inclusions in sample SH304 (eruption date, 18 October, 2004), and one inclusion from SH305 have more than 200 ppm SO₂. Chlorine abundances in glasses show a wider range, with early matrix glass of the glassy fragment SH304-2G1 having more than 800 ppm Cl; whereas matrix glass in SH305, erupted later, is depleted, with less than 400 ppm Cl, consistent with more extensive degassing of microcrystalline SH305. The matrix glass with the lowest SiO₂ is in a fragment from tephra sample MSH05WS-1-16, collected from the January 16 ash explosion deposit.

for thermobarometry in this study have Mg/Mn ratios within error limits of the equilibrium line of Bacon and Hirschmann (1988).

We have observed apparent zoning in both the titanomagnetite and ilmenite with respect to distance from the boundary between these two phases (fig. 14), although the abrupt increase in Ti in the ilmenite near the boundary has been attributed to submicron-scale recrystallization of the ilmenite (Devine and others, 2003; Rutherford and Devine, this volume, chap. 31). For grain pairs in which zoning is apparent in one phase but not the other, we calculated multiple apparent temperatures and oxygen fugacities using each individual analysis of the zoned phase and the average composition of the unzoned phase. Temperatures for the first seven months of the eruption are plotted against eruption dates and permissive date ranges (from table 1) in figure 15.

The early sample of microcrystalline dacite (SH304-2a9; eruption date approximately October 18, 2004; table 1) yields a temperature of 850±5°C at an oxygen

fugacity of 10^{-12.29 ± 0.07} (table 8), which we take to be the conditions of last equilibration of the magma prior to ascent in 2004. Zoning in oxides erupted subsequently yield Fe–Ti oxide thermometer results that range to apparent temperatures of 950°C or more before plunging to less than 800°C in April 2005. Our samples that were erupted since April 2005, after the eruption rate slowed substantially, all contain titanomagnetite with oxidation lamellae of titanohematite, such that we have been unable to obtain meaningful thermometry results for the later part of the eruption.

Bulk-Rock geochemistry

No significant variation in average major- and trace-element whole-rock compositions of the 2004–2006 dome samples is apparent in the major-element data; standard deviations for more than 20 samples are close to the range of uncertainty expected for replicate analysis

Table 8. Fe-Ti oxide thermobarometry results for 2004–2005 eruptive products.

[Temperatures and oxygen fugacities calculated using Fe-Ti exchange thermometer and oxygen barometer of Andersen and Lindsay (1988) and the solution model of Stormer (1983). Complete oxide analyses, by electron microprobe, are presented in digital appendix. Grain number indicates each of successive individual grains analyzed by electron microprobe; “c” indicates composite grain, typically with two or more magnetite crystals attached to single ilmenite. Grain pair size shows maximum dimension of combined grains. Zoning coded as follows: U, unzoned; Z (IL), zoned ilmenite; Z (MT), zoned titanomagnetite; Z (B), zoning in both oxide grains; (ZR), reversely zoned with lower Ti in magnetite near contact with ilmenite; (S) = slight zoning detected but inadequate to warrant separate calculations of temperature and oxygen fugacity (fO_2); Ux = unzoned, but partially exsolved; broad beam analyses used. Eruption dates and related uncertainty described in table 1.

Averages and standard deviation (std. dev.) calculated only for unzoned or weakly zoned grains. For zoned grains, temperature (T) and oxygen fugacity (fO_2) calculated for individual spot analyses of zoned phase vs. average composition of the unzoned phase, or for near-contact single ilmenite-magnetite pairs. Column for analyses/grain pairs refers to total number of analyses used in calculation, followed by number of grain pairs for samples with homogeneous distributions of oxide temperatures. Samples SH300 and SH304 yield results that are tightly clustered, reflecting primary magmatic equilibration conditions in the Mount St. Helens magma reservoir at depth. All other samples of the 2004–2006 dacite have heterogeneous oxide mineral populations that show evidence of disequilibrium, attributed mainly to transient heating.]

Grain No.	Sample No. and notes	Grain pair size	Zoning	Eruption date	T, °C	Std. dev.	fO_2	Std. dev.	Analyses/grain pairs
SH300-1A3			U	1980-86?	904	4	-11.50	0.08	21/3
SH304-2A9			U	10/18/04	850	5	-12.29	0.07	65/4
SH304-2Gg1			U	10/18/04	844	2	-12.43	0.07	61/6
SH305-1									
1	Average (40 μ m)		Z (MT)	11/20/04	883	3	-12.11	0.06	5
1	$\pm 3 \mu$ m from contact	40 μ m	Z (MT)	"	953		-11.05		2
2	43 μ m from IL	65 μ m	Z (MT)	"	898		-11.48		2
2	32 μ m from IL	"	Z (MT)	"	903		-11.41		2
2	26 μ m from IL	"	Z (MT)	"	907		-11.35		2
2	18 μ m from IL	"	Z (MT)	"	921		-11.17		2
2	10 μ m from IL	"	Z (MT)	"	938		-10.95		2
2	4 μ m from IL	"	Z (MT)	"	928		-11.07		2
2	Average	"	Z (MT)	"	915	13	-11.25	0.15	11
3	Average interior	20 μ m	Z (MT)	"	880	3	-12.41	0.02	10
3c	$\pm 3 \mu$ m from contact	"	Z (B)	"	998		-10.77		2
4c	weakly zoned	20 μ m	S (MT)	"	912	12	-11.71	0.13	6
5	small grain pair	8 μ m	Z (MT)	"	1019	83	-10.65	1.07	4
6	Average	40 μ m	U	"	908	2	-11.72	0.03	6
7c	first mt grain (6 μ m)	15 μ m	U	"	858	9	-12.79	0.25	5
7c	second mt grain (4 μ m)	"	U	"	935		-11.66		4
8	Average	25 μ m	U	"	891	1	-12.09	0.04	10
9	Average	25 μ m	U	"	883	1	-12.03	0.01	9
10c	Average	40 μ m	S (MT)	"	871	10	-12.50	0.19	10
11	Average	40 μ m	U	"	857	1	-12.80	0.02	10
SH305-1 (kc)									
1	Average	14 μ m	S (MT)	11/20/04	873	7	-12.30	0.18	5
2	Average	12 μ m	U	"	862	6	-12.53	0.15	6
SH305-2A									
1	Average	30 μ m	Z (MT)	11/20/04	936	23	-11.42	0.31	16
2	Average	40 μ m	S (MT)	"	791	14	-14.91	0.33	8
3	Average	30 μ m	U	"	858	12	-13.19	0.27	11
4	<20 μ m from IL	100 μ m	Z (MT)	"	944	8	-11.06	0.10	9
4	Core of mt. vs. IL	"	"	"	842		-12.43		7

Table 8. Fe-Ti oxide thermobarometry results for 2004–2005 eruptive products. ContinuedMSH05JV-1-19 (1/16/05 grains in ash)

1	Average	100 µm	Ux	1980-86?	884	14	-11.38	0.19	9
3	Average	100 µm	U	"	888	5	-11.61	0.09	8
4	Interior of grains	100 µm	S (MT)	"	912	9	-11.01	0.13	8
4	5 µm from IL	"	S (MT)	"	931		-10.78		5
5	Average	130 µm	Ux	"	895	13	-11.46	0.17	6
6	Average	100 µm	U	"	778	6	-13.80	0.15	10
7	Average grain interiors	120 µm	Z(B)	"	938	8	-10.66	0.12	12
7	Average ±15 µm of contact	"	"	"	830	13	-13.28	0.40	8
8	Average	120 µm	U	"	873	13	-12.09	0.20	18
9	Average	70 µm	U	"	833	6	-12.57	0.12	10
10	Average	35 µm	U	"	750	5	-14.73	0.22	9

MSH05WS-1-19 (1/16/05 grains in ash)

9b	Average grain interiors	200 µm	Z(MT)	"	833	6	-12.57	0.12	7
9b	Average ±8 µm of contact	"	"	"	929	6	-11.27	0.12	8

SH308-3A

1	Average	12 µm	U	02/22/05	865	6	-13.04	0.01	8
2	Average	20 µm	U	"	909	9	-11.86	0.23	9
3	Average	40 µm	S (MT)	"	891	2	-12.08	0.06	17
4	Average	25 µm	U	"	882	1	-12.05	0.01	11
5	Average	17 µm	U	"	863	6	-12.50	0.10	8
6	Average	40 µm	U	"	882	1	-12.05	0.01	13
7	Average	40 µm	U	"	863	6	-12.50	0.09	12

SH308-3A (CT)

1	Grain 3-4	40 µm	?	02/22/05	850		-13.40		2
2	Grain 7-8	30 µm	?	"	898		-12.01		2
3	Grain 9-10	30 µm	?	"	844		-13.26		2
4	Grain f2 1-2	40 µm	?	"	850		-13.40		2
5	Grain f2 3-4	30 µm	?	"	857		-12.49		2
	Average of above				860	22	-12.91	0.63	

SH309-1 (CT)

1	Grain 7-5	50 µm	?	02/22/05	958		-10.35		2
2	Grain 8-9	60 µm	?	"	990		-10.07		2

3-08-05 grains in ash (CT)

1	DRS4g1 1-2	15 µm	?	03/08/05	868		-12.86		2
2	DRS4g1 3-4	15 µm	?	"	887		-12.42		2
3	DRS4g1 5-6	30 µm	?	"	842		-13.75		2
4	DRS4g2 1-2	25 µm	?	"	846		-13.31		2
5	DRS4g2 3-4	40 µm	?	"	825		-13.85		2
6	DRS4g2 5-6	50 µm	?	"	828		-13.85		2
7	DRS4f3g1-2	50 µm	?	"	871		-12.66		2
8	DRS4f51 1-2	25 µm	?	"	846		-13.51		2
	Average of above				852	22	-13.28	0.56	

SH312-1

1	Average	40 µm	Z (MT)	03/08/05	894	2	-11.86	0.03	11
1	±5 µm from contact	"	"	"	957		-10.98		2
2	Average grain interiors	80 µm	Z (MT)	"	871	2	-11.92	0.04	13
2	5 µm from IL	"	"	"	898		-11.57		7
2	12 µm from IL	"	"	"	913		-11.38		7
2	18 µm from IL	"	"	"	910		-11.41		7
2	25 µm from IL	"	"	"	898		-11.57		7

Table 8. Fe-Ti oxide thermobarometry results for 2004–2005 eruptive products. Continued

2	32 μm from IL	"	"	"	890		-11.68		7
2	40 μm from IL	"	"	"	880		-11.82		7
3c	Average	40 μm	U	"	878	8	-12.42	0.17	20
4c	first mt grain (15 μm)	55 μm	U	"	929	5	-11.07	0.07	11
4c	second mt grain (10 μm)	"	"	"	921	1	-11.29	0.04	6
5	SH312 gr5	30 μm	U	"	920	17	-11.33	0.33	4
8	SH312 gr5c	25 μm	U	"	857	2	-12.47	0.05	3
6	SH312 gr6	50 μm	U	"	903	4	-11.44	0.02	10
7	SH312 gr7	50 μm	U	"	895	3	-11.85	0.08	12
<u>SH314-2</u>									
1	Average	20 μm	U	04/17/05	794	14	-14.21	0.48	5
2	Average	50 μm	U	04/17/05	813	2	-13.51	0.01	8
3	Average grain interiors	50 μm	ZR(MT)	04/17/05	872	3	-12.55	0.07	11
3	SH314-2 gr3 ct	"	"	04/17/05	840		-13.03		6
3	4 μm from IL	"	"	04/17/05	847		-12.92		6
3	8 μm from IL	"	"	04/17/05	853		-12.83		6
4	SH314-2 gr4 sm	25 μm	U	04/17/05	794	1	-13.51	0.03	5
5	Average	45 μm	U	04/17/05	855	11	-12.75	0.16	11
7	Average	40 μm	U	04/17/05	764	38	-15.23	1.34	8
8	Average grain interiors	30 μm	Z (MT)	04/17/05	736	1	-16.62	0.02	8
8	5 μm from IL	"	"	04/17/05	815	7	-13.56	0.18	5
<u>SH315-2</u>									
1	Average	300 μm	Z (IL)	04/01/05	739	24	-16.29	0.83	6
1	High Fe IL core vs. avg. MT	"	"	04/01/05	828		-13.39		4
2	Average grain interiors	60 μm	Z (MT)	04/01/05	838	1	-13.79	0.05	8
2	4 μm from IL	"	"	04/01/05	805	1	-14.34	0.07	9
3	Average	50 μm	S (IL)	04/01/05	807	9	-14.23	0.27	7
4	Average	25 μm	U	04/01/05	791	33	-14.75	1.14	6
5c	Average	30 μm	U	04/01/05	742	98	-16.40	3.81	9
6	Average	30 μm	U	04/01/05	817	3	-13.86	0.12	7
7	Average	35 μm	U	04/01/05	813	40	-14.08	1.22	7

of standard rocks (table 7). The 2004–2006 dacite has 64.93 ± 0.09 percent SiO_2 and relatively high $\text{Na}_2\text{O}/\text{K}_2\text{O}$ of 3.2, a ratio that is similar to other Mount St. Helens dacite. The lack of variation in SiO_2 with eruption date is evident in figure 16, which also shows SiO_2 abundances for gouge and dacite collected from the roof of spine 3 (SH300, SH301), when it first breached glacial ice in the southeastern crater on October 27, 2004. These roof-rock samples have distinctly lower SiO_2 and alkalis and higher MgO, CaO, and FeTO_3 (total iron expressed as Fe_2O_3), and their compositions overlap with those of lava erupted in 1985–1986 (table 7, fig. 17), suggesting that they are crater-floor rocks uplifted by the 2004 dacite as it punched through the crater floor. Analyses

of several small glassy fragments that were collected in dredge samples from the early spines (spines 1 and 3) are also listed in table 7. These are higher in silica than samples from the 1980–1986 dome and may represent fragments of dacite that were intruded early in the 2004 eruption.

Compositions of the 2004–2006 samples lie along the high- SiO_2 projections of most major- and minor-element variation trends from the 1980–1986 dome lavas (Pallister and others, 1992). However, they lie off the trend for TiO_2 , which is present in higher abundance than in 1980–86 dacites (fig. 17). High-precision analyses of Cr (by INAA) are diagnostic of the presence of basaltic mixing components within Mount St. Helens

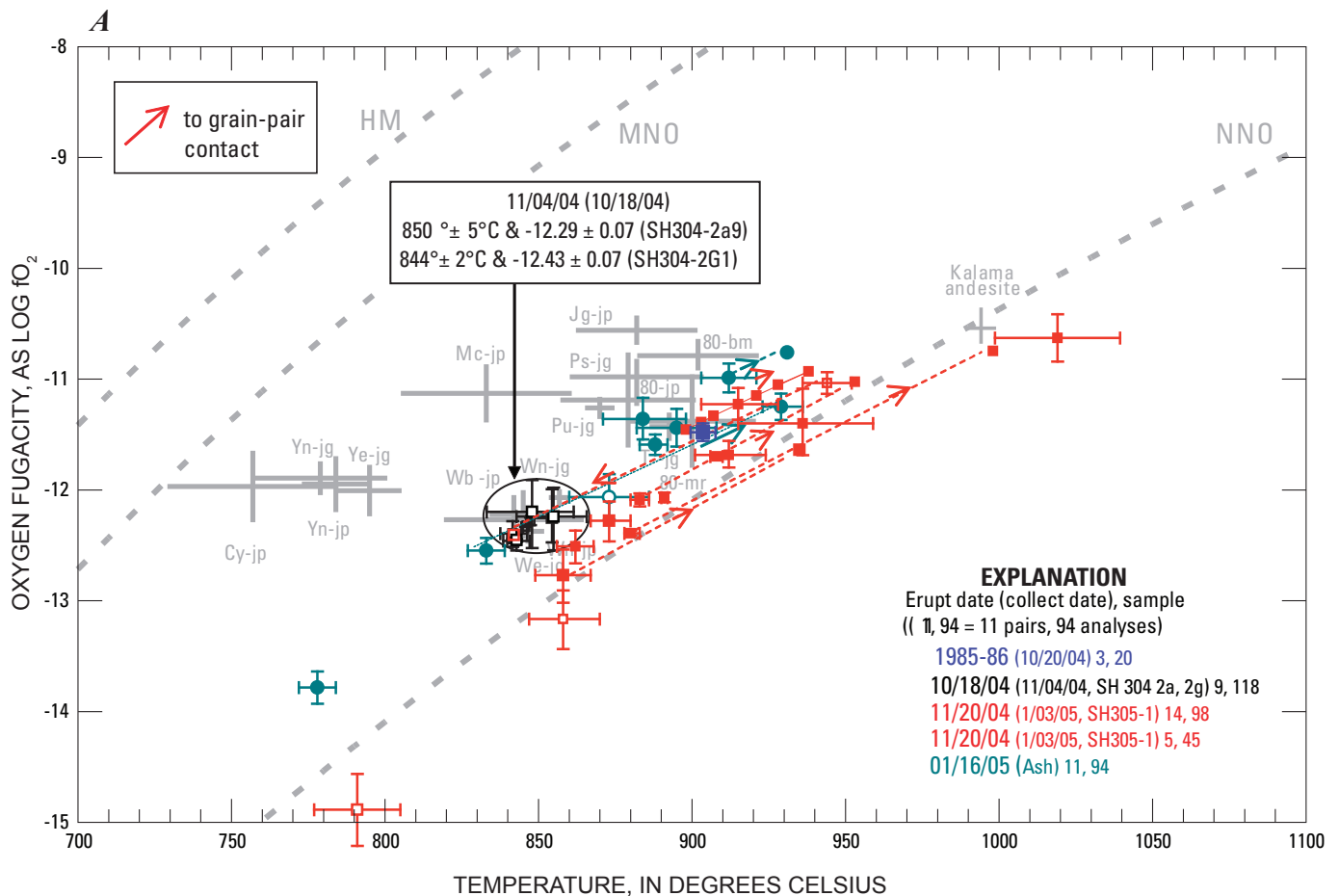
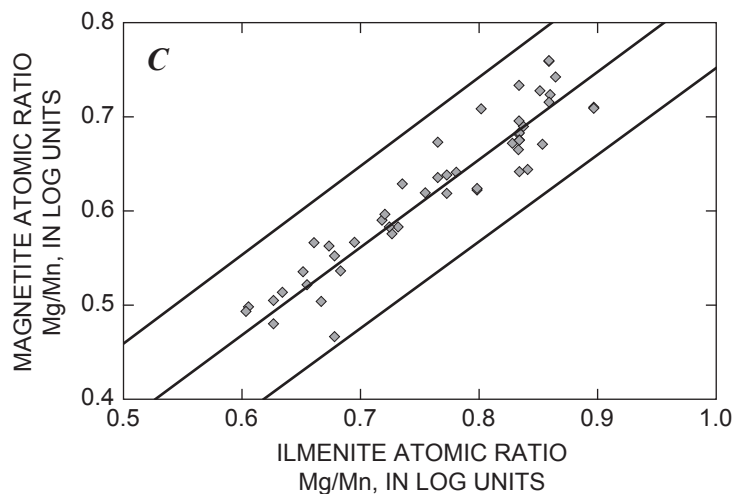
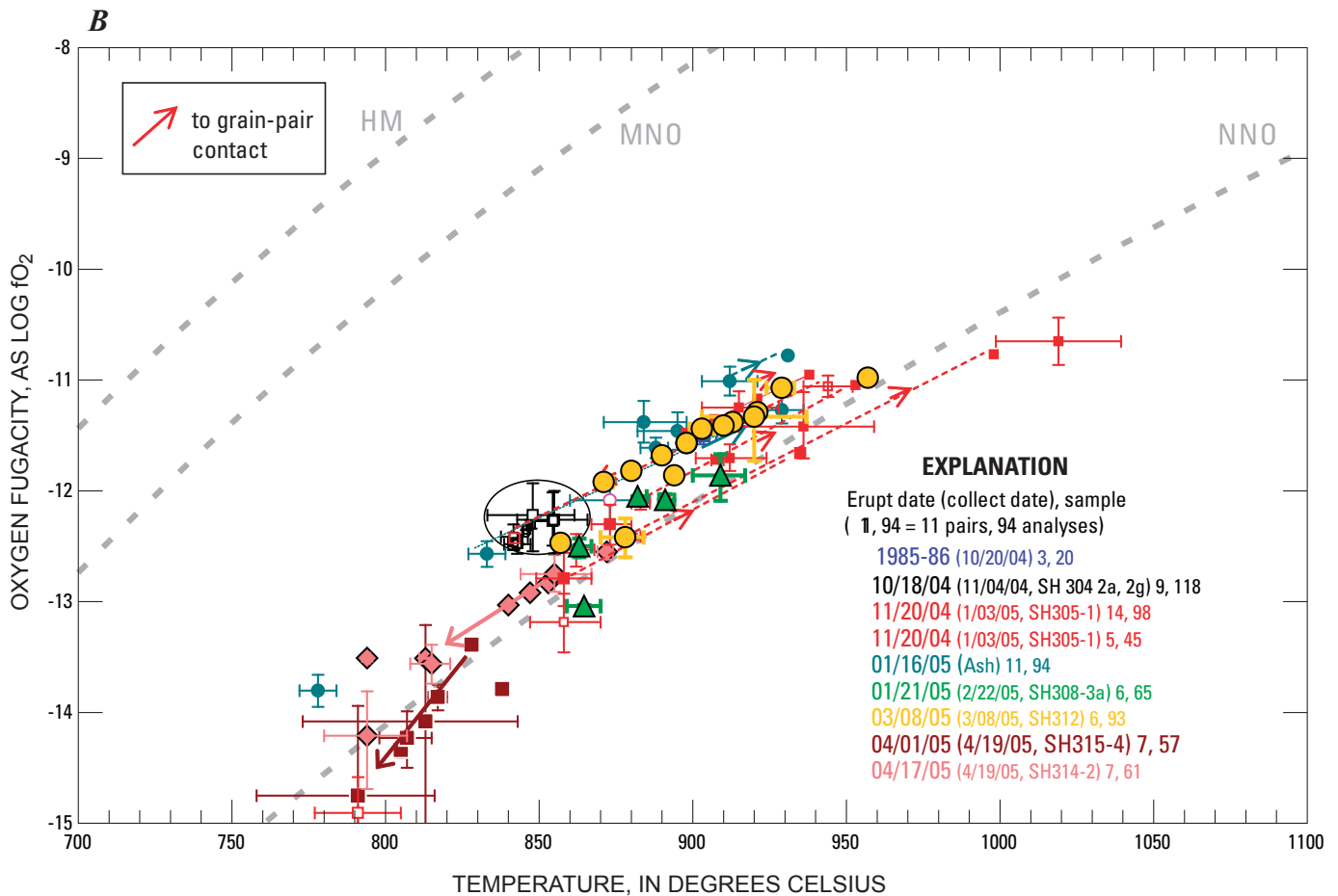


Figure 13 (A, B). Results of Fe-Ti oxide thermobarometry for 2004–2006 lava dome, plotted with respect to oxygen fugacity and temperature. Buffer curves for nickel-nickel oxide (NNO), manganese-manganese oxide (MNO) and hematite-magnetite (HM), and results for samples from earlier eruptive episodes at Mount St. Helens plotted for comparison. (A) data from samples erupted between October 18, 2004, and January 16, 2004, as well as data from 1980 and previous eruptions at Mount St. Helens. Two letter symbols such as “Cy” refer to tephra units of Mullineaux (1996), suffixes refer to source of data as follows: -jg =Jim Gardner (Gardner and others, 1995a, 1995c), -mr = Malcolm Rutherford (Rutherford, 1985), -jp =John Pallister (unpublished). (B) data from samples erupted between January 21 and April 17, 2005. Samples color coded by eruption date. Number of grain pairs of the two solid-solution series ilmenite (FeTiO_3)–hematite (Fe_2O_3) and magnetite (Fe_3O_4)–ulvöspinel (Fe_2TiO_4) for each sample are indicated in the explanation box. In cases in which temperatures and oxygen fugacities cluster, error bars represent ranges derived from the thermobarometer by using maximum and minimum values of standard deviations of Fe and Ti. In cases in which zoning was apparent from analytical profiles, backscattered-electron imagery, or stage mapping, temperatures and oxygen fugacities are plotted for each analyzed point in the zoned phase. Vectors show trends as contact between the two oxide grains is approached. Most zoned grains show increasing apparent temperature and oxygen fugacity toward grain contact, indicative of recent heating, although latest erupted samples analyzed (April 2005) show apparent cooling and reduction in oxygen fugacity. (C) Shows average atomic Mg/Mn ratios for ilmenite-magnetite pairs used in generating thermobarometric results presented in (A) and (B). Also shown are equilibrium line and error limits (2σ) for oxide pairs from volcanic rocks (Bacon and Hirschmann, 1988).

andesites and dacites (Pallister and others, 1992). Chromium abundances in 2004–2006 dome rocks are compared to those of Kalama (A.D. 1479–1750), Goat Rocks (A.D. 1800–1857), and the 1980–86 eruptive cycles in figure 18 (full INAA analyses and uncertainties are reported in Thornber and others, 2007b). As with TiO_2 , the 2004–2006 dacites have higher Cr abundances than would be expected from a continuation of the Goat Rocks and 1980–86 trends, as well as lower Cr at 65 percent SiO_2 than the early Kalama dacites. Analyses were conducted at the same laboratory using the same procedures and standards to ensure reproducibility, and

duplicate samples from 1985 and 1986 dome rocks were re-run to verify the differences.

A characteristic feature of Mount St. Helens dacite, including 2004–2006 lava, is the lack of europium anomalies and a decrease in total rare-earth element (REE) abundance with increasing SiO_2 , thereby ruling out progressive crystal fractionation in their origins (table 7, fig. 19). The 2004–2006 dacite is distinct in having the lowest heavy-REE abundances of any of the dacites we have analyzed from eruptive products of the last 500 years at Mount St. Helens.



Discussion

Petrology of the 2004–2006 dacite provides constraints on both shallow and deep magmatic processes, insights into the roles that degassing and crystallization play in controlling the explosivity of volcanic eruptions, and how the past history of the volcano helps in forecasting the

future course of the eruption. Accordingly, the discussion is presented in four parts: (1) shallow conduit processes, (2) deep reservoir processes, (3) implications for magmatic plumbing, explosivity, and eruption triggering, and (4) lessons from the past and implications for the future.

Shallow conduit processes

Field relations, petrography, volatile contents of glasses, and oxide thermobarometry help us understand the processes that were operative in the shallow conduit beneath the 2004–2006 vent. Together with geophysical and gas geochemical monitoring data they show that magma within the conduit solidified at shallow levels beneath the vent, producing a nearly solid seismogenic plug (Iverson and others, 2006) that has fed the series of spines that constitute the new lava dome.

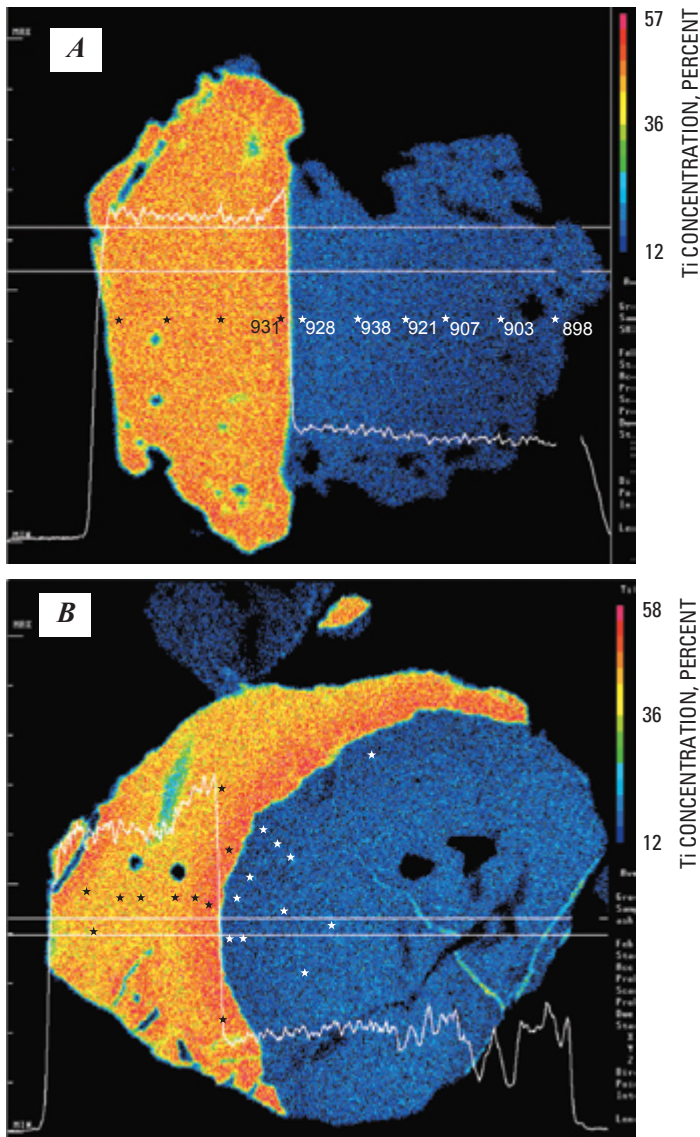


Figure 14. Electron microprobe stage maps showing abundance of TiO_2 in oxide grain pairs from samples SH305-1 (A) erupted approximately November 20, 2004, and MSH05JV-1-19 (B) from a dacite fragment in the ash deposit from the January 16, 2005, explosion. Maps are 100 X 100 μm in dimension. The SH305-1 grain pair (A) shows a relatively uniform or slightly decreasing TiO_2 trend across ilmenite grain (orange) with a steep increase in abundance within 10 μm of the contact with the adjacent titanomagnetite grain (blue) and a gradual increase in TiO_2 across the titanomagnetite grain toward the ilmenite grain. Apparent temperatures, calculated for individual analytical points in the titanomagnetite (as indicated by the asterisks and numbers in the figure) compared to the average composition of the ilmenite show a decrease from 928° C at the grain contact to 898° C at the rim. The apparent temperature for the two analytical points closest to the grain boundary yielded 931° C. The MSH05JV-1-19 grain pair (B) displays the same abrupt decrease in Ti in the ilmenite with distance from the titanomagnetite, but the opposite trend in the titanomagnetite, which shows a gradual decrease in TiO_2 abundance as the grain boundary is approached. The superimposed line graphs show the relative abundance of TiO_2 in the band outlined by the two horizontal lines in each image. The MSH05JV-1-19 grain pair (#7 in Table 8) shows a decrease from an average of 830° C for points within 10 microns of the grain boundary to 938° C for the average compositions of the two grain interiors.

Constraints from field geology

The 2004–2006 eruption of Mount St. Helens represents a nonexplosive end member in the range of eruptive behavior of dacitic magmas. By the spring of 2006 the volume of the new dome exceeded $80 \times 10^6 \text{ m}^3$ (Schilling and others, this volume, chap. 8), a volume similar to the 1980–1986 lava dome ($74\text{--}77 \times 10^6 \text{ m}^3$ (Swanson and Holcomb, 1990). Eruption rates have ranged from as high as 9 m^3/s in the initial phase to less than 1 m^3/s (Schilling and others, this volume, chap. 8). The style of eruption, with continued extrusion of solid dacite spines, contrasts with most of the 1980–1986 dome-forming eruptions at Mount St. Helens, as well as with most other dome-forming eruptions worldwide. The development of gouge-mantled spines is unusual but not unique. Photographs of the Showa-Shinzan lava dome (extruded in a Japanese wheat field on the flank of Mount Usu in 1944–45) show spines with striations that look remarkably like those on the Mount St. Helens dome (Mimatsu, 1995). The 200-m-diameter cylindrical and striated spine of Mount Pelée, Martinique, is another example. The original Peléan spine rose at rates of 3–6 m per day and reached a height of 115 m above the crater

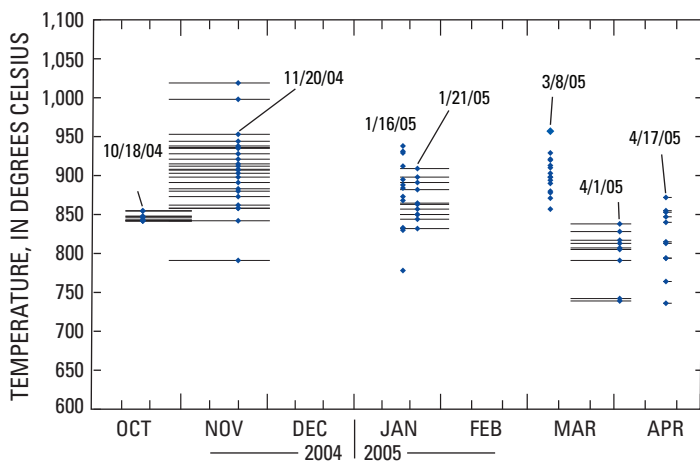


Figure 15. Fe-Ti oxide temperatures for 2004–2005 Mount St. Helens dacite lava samples plotted against eruption dates; diamonds indicate best estimate of eruption dates, bars show full range of permissible eruption dates (table 1). Wide range in apparent temperatures result from zoned oxide pairs (figure 14).

rheologically solid dacite lava hundreds of meters beneath the vent.

The “megaspines” of the early (1995–1998) eruptive phase of the Soufrière Hills volcano, Montserrat, also had striated surfaces and cataclastic textures, based on observations by one of us (K.V.C.). As their morphologies are correlated with eruption rate and character of seismicity (Watts and others, 2002), it is instructive to compare these with the Mount St. Helens examples. At Montserrat, vertical spines and whaleback structures dominated at rates of $<1 \text{ m}^3/\text{s}$, and their emplacement was accompanied by periodic hybrid earthquake swarms. Megaspines were emplaced aseismically at $1\text{--}2 \text{ m}^3/\text{s}$. Broad shear-lobe spines were emplaced aseismically at $2\text{--}5 \text{ m}^3/\text{s}$, but their collapse was accompanied by intense hybrid swarms. Blocky shear-lobes were emplaced at $2\text{--}5 \text{ m}^3/\text{s}$, accompanied by repetitive hybrid swarms and tremor. Pancake lobes were emplaced at $7\text{--}9 \text{ m}^3/\text{s}$, also with repetitive hybrid swarms and tremor. Explosions at Montserrat occurred at eruption rates greater than $9 \text{ m}^3/\text{s}$ and commonly followed large dome-collapse events.

The Mount St. Helens spines are similar to the vertical spines, whaleback structures, and megaspines of Montserrat. But instead of being restricted to eruption rates of less than $2 \text{ m}^3/\text{s}$, these morphologies have occurred over the full range of eruption rates, and collapse events have been small—rockfalls and sparse rock avalanches that have not triggered substantial pyroclastic flows. These differences are likely related to compositional differences (andesite at Soufrière Hills, dacite at Mount St. Helens), and to a much larger vent diameter of $100\text{--}200 \text{ m}$ at Mount St. Helens, compared to about 30 m at Soufrière Hills. The larger vent diameter allows slower ascent rates and more extensive shallow crystallization for similar volumetric rates of extrusion.

Compared with activity at Soufrière Hills, Montserrat, collapse events at Mount St. Helens have been minor. Limited disintegration of collapsing blocks during short runouts onto the low-relief crater floor at Mount St. Helens is likely due to a drier composition and the more solid (microlite-rich and glass-poor) character of the Mount St. Helens dacite lava compared to the more glass- and water-rich matrix glasses of the Montserrat andesite lava (Couch and others, 2003; Harford and others, 2003). Furthermore, greater topographic relief at Soufrière Hills has contributed to greater runout distances.

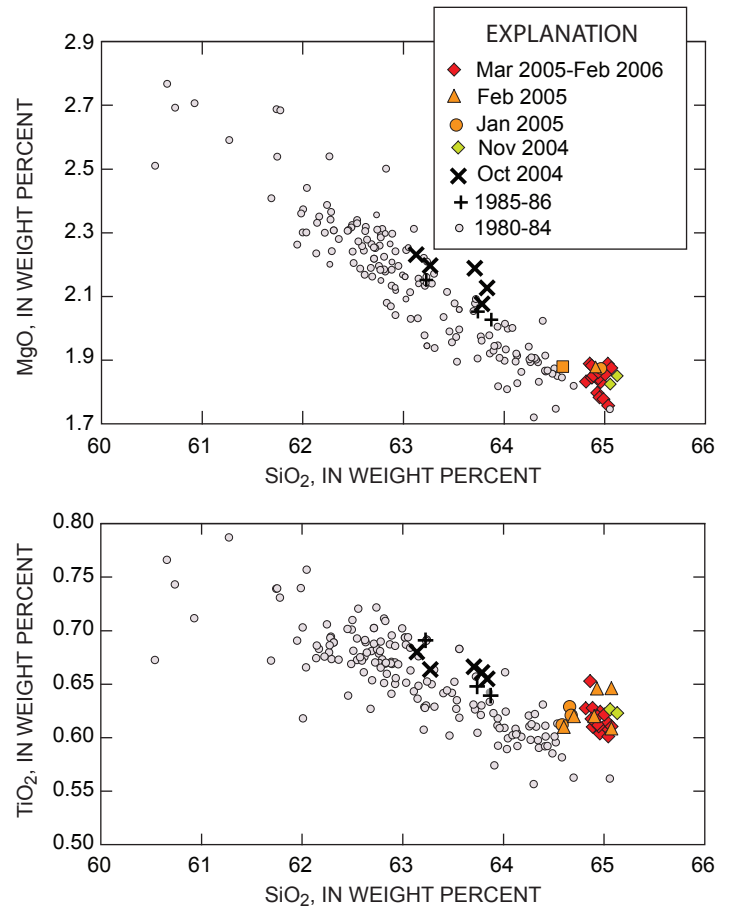


Figure 17. MgO- and TiO₂-silica variation diagrams, showing trends in juvenile eruptive products from 1980-1986 eruption at Mount St. Helens (Pallister and others, 1992) and 2004-2006. Note that 2004–2006 samples lie at high-SiO₂ projection of the linear arrays except for TiO₂, which is distinctly higher for given SiO₂ content in the 2004–2006 lavas than in previous eruptive episodes.

Constraints from petrography and major-element compositions of matrix glasses and microlites

As shown in figures 4 through 8, the matrix of the 2004–2006 dacite is remarkably rich in microlites, even compared to the dome lava of the 1980s (with the exception of spine samples from 1983 and 1985, which are also highly crystalline). We interpret these matrix textures to result from extensive depressurization-driven crystallization during ascent of the magma through the conduit, similar to the process envisioned for the 1980–86 dome (Blundy and Cashman, 2001; Cashman, 1988, 1992). In contrast to the episodes of the 1980s, we see no evidence for stagnation of magma at multiple levels of the conduit. Instead, an analysis of eruptive volumes and likely conduit dimensions (discussed below) and

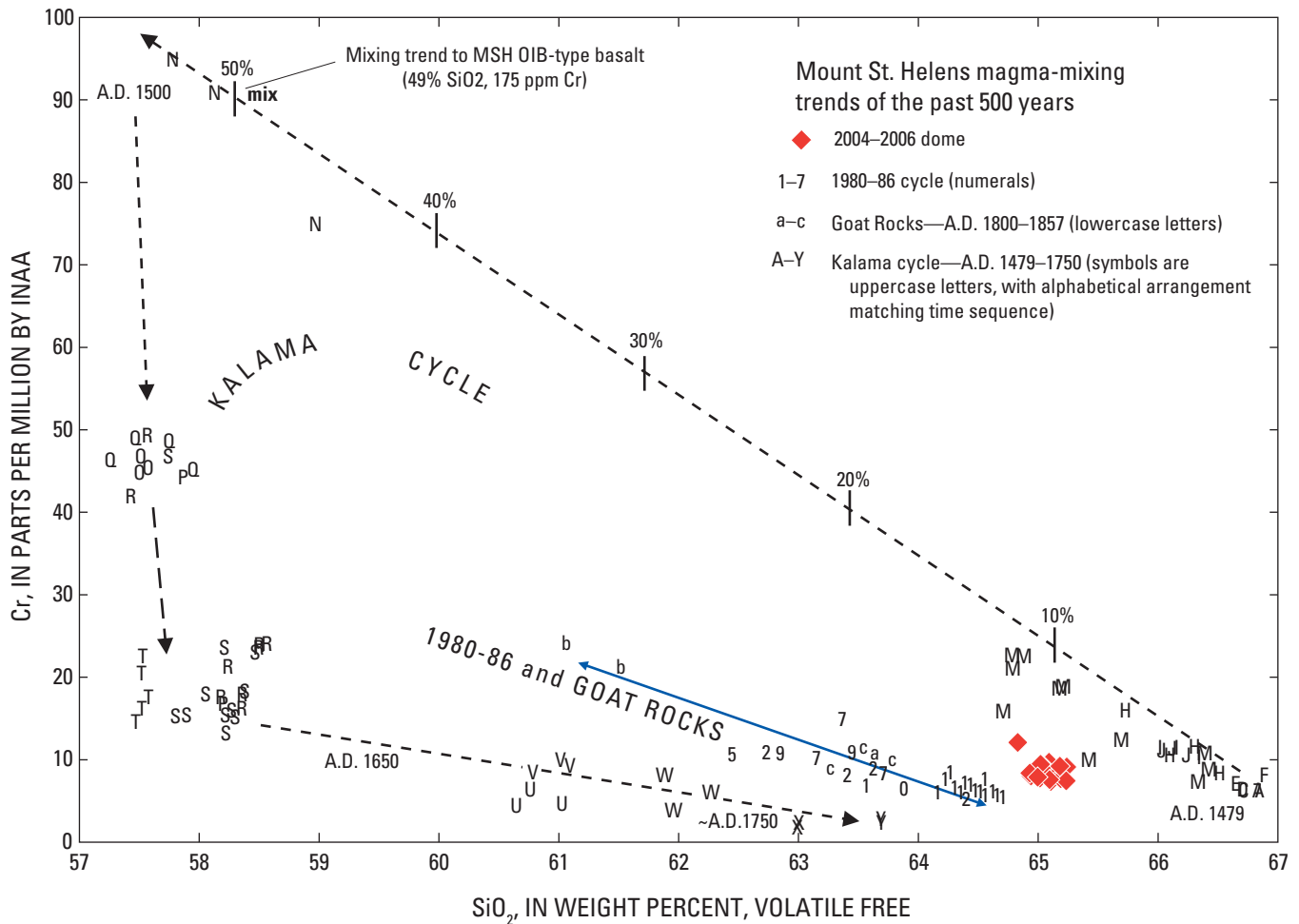


Figure 18. Cr-SiO₂ variation for juvenile eruptive products from Mount St. Helens erupted during past 500 years (Pallister and others, 1992). Note that 2004–2006 samples have higher Cr abundance than the projection of the Goat Rocks and 1980–1986 trend but lower abundance than the early phase of the Kalama chemical cycle (A.D. 1479–1750). Analytical uncertainty for Cr is ± 3 ppm at the 10 ppm level (INAA data) and ± 0.2 percent SiO₂ (XRF data) on basis of counting statistics and replicate analyses. Magma mixing with basaltic magmas at Mount St. Helens is called on to explain the cyclic trends (Pallister and others, 1992). Letters and numbers refer to stratigraphic sequence, and percentages refer to proportions of a basaltic mixing endmember as explained in Pallister and others (1992).

consistency of amphibole reaction-rim thicknesses (Rutherford and others, this volume, chap. 31; Thornber and others, this volume, chap. 32) indicates that dacite lava of the current eruption is a product of continuous ascent of magma through a conduit that taps the top of the deeper reservoir at about 5 km depth. We see a continuum in the degree of matrix crystallization, from early 2004–early 2005 samples with variable fractions of matrix glass to late 2005–2006 samples, which have only trace amounts of glass remaining. Such a pattern is consistent with more rapid ascent and eruption rates during the early phase of the eruption.

The crystallization of a granite-minimum microlite assemblage of tridymite or quartz, An_{20–30} plagioclase, and anorthoclase (table 4) is consistent with extensive

groundmass crystallization. The high-silica rhyolite composition of residual glass is indicative of very shallow final crystallization. Following the arguments of Blundy and Cashman (2001), the presence of quartz and the projection of glass compositions onto the modified Qz-Ab-Or ternary diagram of Blundy and Cashman (2001) yield crystallization pressures for the most evolved matrix glasses between 50 MPa and 0.1 MPa (fig. 20). This result indicates crystallization at a depth considerably less than 2.2 km, on the basis of a density model (Williams and others, 1987, section B–B') in which the crustal column consists of 1.5 km with density of 2.15 g/cm³ overlying an extensive diorite to gabbroic pluton with average crustal density of 2.7 g/cm³. The presence of tridymite in some samples further restricts

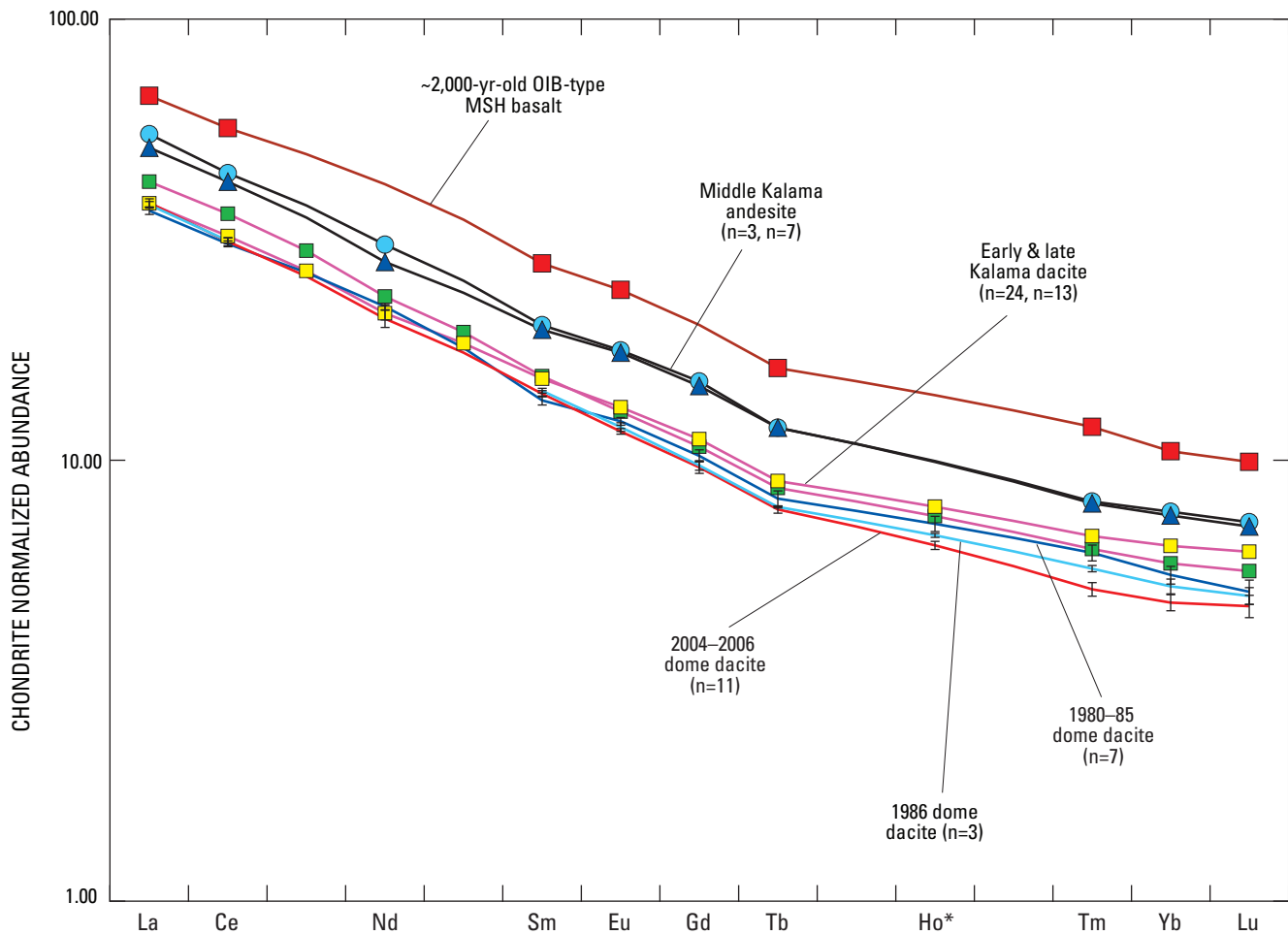


Figure 19. Chondrite-normalized rare-earth element (REE) abundance patterns for juvenile eruptive products from Mount St. Helens erupted during the past 500 years. Note that the 2004–2006 lavas have the lowest heavy-REE abundances.

the pressure for matrix crystallization and solidification to the range 11–25 MPa (depth 0.5–1.0 km) at temperature 885–915°C (Blundy and Cashman, 2001), consistent with the shallow location of earthquakes that have accompanied the eruption (Thelen and others, this volume, chap. 4).

Constraints from SO₂, Cl, and H₂O abundances in glasses

The abundance of H₂O in glasses can also be used to constrain depths owing to the variation in solubility of water in silicate melts with pressure (Moore and others, 1995, 1998). Matrix and inclusion glasses show a decline in water content from approximately 2.3 wt. percent H₂O at 73.5 percent SiO₂ to less than 0.1 percent at 77 percent SiO₂ (fig. 11). The upper end of this H₂O range is indicative of quenching at a pressure of about

30 MPa (1.4 km) followed by decompression-driven crystallization and quenching of residual melt, which continued to pressures of less than 10 MPa (depth about 0.5 km). Most of the glass inclusions analyzed so far have water and SO₂ contents that overlap with the matrix glasses, indicating that most of the inclusions have leaked (fig. 11).

Total dissolved water concentrations determined in the matrix glass of samples SH304-2G1 and SH304-2G2 were also used to constrain the pressure and depth at which residual melt in this glassy sample passed through the glass transition. Water solubility in the melt at 850°C was computed from electron microprobe determinations of the matrix glass bulk composition and the 0–300-MPa water solubility model of Moore and others (1998). Given saturation, the total water concentration in matrix glass of sample SH304-2G2, which has the most microlite-free matrix glass and the greatest water

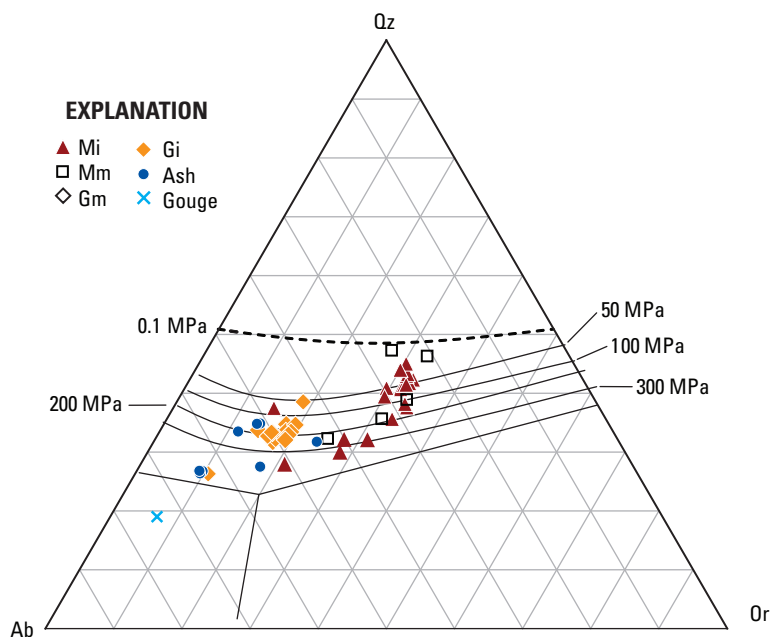


Figure 20. Projection of glass compositions from SH304 and SH305 samples onto modified Quartz-Albite-Orthoclase haplogranite ternary diagram of (Blundy and Cashman, 2001). Cotectic lines and water-saturated minima and eutectics are plotted as function of pressure for comparison. Dashed line is approximate position of the 1-atmosphere cotectic. Solid symbols refer to melt inclusions, open symbols to matrix melt. Other labels as follows: Mi, melt inclusion in dacite lava; Mm, matrix melt in dacite lava; Gi, melt inclusion in dacite fragment in gouge; Gm, matrix glass in dacite fragment in gouge; Ash, melt inclusion within tephra fragment in ash; Gouge, matrix melt within dacite fragment in gouge.

content (2.3 ± 0.15 wt. percent), indicates quench to glass from approximately 33 to 41 MPa or approximately 1.5 to 2 kilometers depth, on the basis of the density distribution in crustal section B–B’ of Williams and others (1987). Assuming this unusual glassy sample represents a quenched equivalent of the microcrystalline 2004 dacite, these results would indicate incipient matrix crystallization at a depth of 1.5–2 km, although, as noted above, most of the groundmass crystallization and solidification is constrained by the microlite phase assemblage in the more typical microcrystalline dacite to depths of less than 1 km.

The abundance of sulfur in glass inclusions (table 4, fig. 12) is lower than that in glass inclusions from the 1980 Mount St. Helens dacite (Blundy and Cashman, 2006; Devine and others, 1984; Gardner and others, 1995a; Melson, 1983), indicating that the magma was depleted in sulfur before eruption and consistent with the hypothesis that the 2004–2006 magma was residual from the reservoir of the 1980s. The highest sulfur contents (as well as Cl and H₂O) are found in the earliest erupted samples, coincident with the highest SO₂ and CO₂ emissions (Gerlach and others, this volume, chap. 26). This suggests more rapid ascent, less matrix crystallization, and less gas loss as the initial magma made its way relatively rapidly to the surface.

Abundance of Cl in matrix glass is lower than that in glass inclusions (table 4, fig. 12) and decreases with increasing SiO₂ and K₂O (indicators of increasing matrix crystallization), consistent with degassing accompanying decompression crystallization at shallow levels, as also seen at Soufrière Hills volcano (Edmonds and others,

2001; Harford and others, 2003). The abundance of Cl in glass inclusions and matrix melts can be used to calculate emission rates of Cl for the eruption. We use our average Cl abundance of 1155 ± 142 ppm in glass inclusions as representative of the dacite at magma reservoir depths (4–5 km) (Rutherford and Devine, this volume, chap. 31), 852 ± 47 ppm for the magma at a depth of 1.4 km (as inferred from the water content of the glass in SH304-2G1), and 278 ± 53 ppm for the residual Cl in the microcrystalline dacite lava (table 4). The average Cl value for glass inclusions (1155 ± 142 ppm) is based on inclusions in amphibole crystals (a Cl-bearing phase) from sample SH305-2A9b. Although exchange of Cl with the host crystal is a possibility, the average abundance is similar to the higher Cl abundances in plagioclase and hypersthene inclusions, which range widely from 400 to 1450 ppm; the lower abundances likely result from leakage. The differences between the abundance in the glass inclusions and that in the matrix glasses, multiplied by the dacite density (approximately 2400 kg/m³) yields emissions of 400 ± 249 metric tons per million cubic meters of dacite for the ascent interval from 5 to 1.4 km depth and 758 ± 132 metric tons for the interval from 1.4 km to the surface. The total emission is 1158 ± 381 metric tons per million cubic meters of dacite extruded, or about 100×10^3 metric tons for the 85×10^6 m³ extruded through August 2006. On the basis of this analysis, we would predict Cl emissions between 100 ± 33 and 700 ± 231 metric tons per day for extrusion rates of 1 m³/s and 7 m³/s, respectively, exclusive of any contribution from a separate fluid phase. This value is greater than that the rate of 12–25 metric tons per

day measured on August 31, 2005, by open-path FTIR (Edmonds and others, this volume, chap. 27). The discrepancy may be due to (1) precipitation of chlorides in dome rocks (yellow efflorescence has been common near fumaroles and attributed to deposition of iron chlorides), (2) shallow scrubbing of Cl into groundwater (however, only 5.2 tons per day of dissolved Cl was measured in water from Loowit and Step springs at the crater mouth, and no spike in Cl abundance has yet been detected, (Bergfeld and others, this volume, chap. 26) or (3) a lower Cl abundance in the August 2005 dacite compared to that from late 2004, when our glass inclusion-bearing samples were erupted. We consider the latter possibility most likely.

Constraints from oxide thermobarometry

Zoned oxides similar to those in the 2004–2006 dacite are known to occur in volcanic rocks that have undergone recent heating due to magma mingling, and the time scales for preservation of zoning in oxide minerals have been determined experimentally to be on the order of a few days to a few months, depending on the size of the oxide grains and degree of heating (Devine and others, 2003; Gardner and others, 1995a; Nakamura, 1995; Pallister and others, 1996; Venezky and Rutherford, 1999). Although there is clear petrographic and geochemical evidence for magma mixing in older rocks from Mount St. Helens (Pallister and others, 1992; Smith and Leeman, 1996), there is little such evidence in the 2004–2006 dacite, which is uniform in bulk-rock composition and has only extremely rare and small (less than 1-cm diameter) quenched mafic inclusions.

In several cases, the source of the heating to produce zoned oxides is evident, such as in the case of the June 7–12, 1991, andesites at Mount Pinatubo, which show clear petrographic and geochemical evidence of derivation by mingling of basalt with dacite in proportions of about 1:2 (Pallister and others, 1996). In other cases, the physical evidence of heating by a hotter and more mafic magma is only evident as a small proportion of quenched mafic inclusions, such as in the andesite of Soufrière Hills volcano (Murphy and others, 2000). In the Soufrière Hills case, the zoned oxides indicate apparent heating of about 30°C, which led Devine and others (2003) to propose a model in which underplated basalt heated a boundary zone in an andesitic reservoir. The boundary layer was then mobilized and erupted, with only minor entrainment of the underlying basalt, as seen in ubiquitous blade-shaped laths of pargasite in the groundmass of all samples.

In their study of microlite formation in the Soufrière Hills andesite, Couch and others (2003) calculated that a temperature rise of as much as 45°C would be expected from latent heat evolved during the extensive (32 percent), shallow (less than 2 km), and relatively rapid (1–2 day) decompression-driven groundmass crystallization, given the measured extrusion rates and estimated conduit diameter (Melnik and Sparks, 2002). However, neither Couch and others (2003) nor Devine and others (2003) concluded that latent heating at shallow levels was responsible for the zoned oxides, because it was not possible to experimentally produce the zoning profiles of the Soufrière Hills titanomagnetites in short-duration (2 day) heating experiments without extensive amphibole breakdown, which was not seen in natural samples. However, longer-duration (2 week) heating experiments at magma reservoir pressure of 130 MPa (5–6 km depth) did reproduce the natural zoning profiles without amphibole breakdown.

The zoned oxides in the Mount St. Helens samples share some features with those from Soufrière Hills. First, the earliest samples from October 2004, when eruption rates were high (greater than 5 m³/s) have oxide pairs that lack zonation. Second, the Mount St. Helens oxide pairs erupted during the winter of 2004–2005 are zoned in a sense that indicates heating (fig. 14). As was also seen in a sample from the explosive eruption of September 29, 1997, at Soufrière Hills (Devine and others, 2003), the zoning in the winter 2004–2005 oxides is best developed at the grain boundary between the titanomagnetite and ilmenite phases, with little zonation developed at melt-crystal boundaries. As is evident from the range of temperature-fO₂ trends for grain pairs in figure 13, the Mount St. Helens thermobarometric results are parallel to the common buffer curves, a characteristic of heating with melt present (Devine and others, 2003). The above features could be interpreted as indicating a similar process of heating by hot magma underplating. However, there is considerable variation in degree of zoning from grain pair to grain pair in the Mount St. Helens samples, even within the same thin section. These features indicate that heating was of relatively short duration and was variable at the scale of millimeters. That the zoning is best developed at the two-crystal grain boundaries indicates redistribution of Ti and Fe within the crystal structures of titanomagnetite and ilmenite, but with little, if any, redistribution between the oxide minerals and the adjacent groundmass glass.

We believe that these small-scale relations are best explained by latent heating during groundmass crystallization, as also suggested for 1980–1986 pumice

and lava samples (Blundy and others, 2006). Variation of heating at the millimeter scale is most readily explained by inhomogeneity in rate and extent of groundmass crystallization and localized variability in transport of heat by vapor expansion, conduction, and access to the hydrothermal system at shallow conduit levels. The fact that zoning is developed with respect to distance from the titanomagnetite-magnetite phase boundary, and not at grain-melt boundaries, is probably a result of the rapidly changing composition and crystallinity of the adjacent groundmass, such that consistent zoning of Fe–Ti oxides by diffusive exchange with melt was not possible. In contrast to the situation at Soufrière Hills, where transport from 2 km to the surface is thought to have been too rapid for latent heating, by the beginning of 2005 the eruption rate at Mount St. Helens had slowed to less than $2.5 \text{ m}^3/\text{s}$ (Schilling and others, this volume, chap. 8) and the conduit at shallow levels was of much larger diameter—100 to 200 m, as opposed to about 30 m for Soufrière Hills (Melnik and Sparks, 2002). Consequently, the ascent time through the shallow interval of groundmass crystallization was longer at Mount St. Helens. Using our estimate that most groundmass crystallization took place mainly in the uppermost 500 m, a near-surface conduit diameter of 200 m, and an ascent rate of $2.5 \text{ m}^3/\text{s}$, we derive an ascent rate of 7 m/d, which is consistent with the measured rates of linear extrusion of spines; (Dzurisin and others, this volume, chap. 14; LaHusen and others, this volume, chap. 16) and an ascent time of about 2.5 months. Allowing the conduit to decrease in diameter with depth, such that it averages 100 m diameter over the uppermost 0.5–1 km, would yield an average rate of 28–56 m/d and an ascent time of 2.6–5.2 weeks. These ascent times are in the appropriate range for development and preservation of zoning in oxides (Devine and others, 2003).

We can estimate the maximum amount of latent heating that is theoretically possible from the amount of groundmass crystallization in the 2004–2006 dacite using thermodynamic data, much as was done by Couch and others (2003) for the Soufrière Hills dacite. Latent heat is equal to the enthalpy of melting divided by the heat capacity at the temperature of interest. As the microlite population is dominated by plagioclase, we can use the range of enthalpies of melting of plagioclase, from 59,280 J/mol for albite to 81,000 J/mol for anorthite, to approximate the amount of latent heat available and the maximum temperature rise. At an initial temperature of about 850°C , the heat capacity of albite would be about 318 J/mol per K; and of anorthite, about 328 J/mol per K. Therefore,

isenthalpic crystallization of 30–40 percent of the dacite would produce a temperature rise of about $30\text{--}45^\circ\text{C}$. A more complete analysis, by Mark Ghiorso using the thermodynamic modeling program pMELTS (Ghiorso and others, 2002) for decompressing a water saturated 2004–2006 dacite composition at 855°C and $f\text{O}_2 = 10^{-12}$ from 20 MPa to 0.1 MPa, estimates a temperature rise of 30°C and results in a magma with 0.5 g ilmenite, 2.5 g magnetite, 7.6 g orthopyroxene, 13 g quartz, 84 g of An_{31} plagioclase, and 12.3 g of 76.6 percent SiO_2 melt with 80 ppm H_2O (Mark Ghiorso, written commun., 2005)—a reasonable match to the natural assemblage. Loss of some of the heat would result in appearance of alkali feldspar in the assemblage, an increase in the abundance of quartz, and a decrease of the melt fraction remaining. Further discussion of the role of latent heating in decompression crystallization of volcanic rocks is available in Blundy and others (2006).

The maximum quantity of latent heat available from groundmass crystallization is less than the degree of apparent heating recorded by the zoned oxides in the dome rocks. We attribute this discrepancy to the fact that the zoned oxides can only give *apparent* temperatures. They indicate heating, but the extent of heating must be less than the maximum indicated by the zoning. If the diffusion rates were fast enough, the distribution of Ti and Fe in the grains would rehomogenize to a value intermediate between the minimum and maximum ranges seen in the zoned crystals and would also reequilibrate with the melt; consequently, the actual temperatures would be less than the maximum apparent temperatures in figure 13.

The analyses from samples collected later in 2005 and 2006 offer additional insights into the process responsible for the oxide zoning (fig. 13B, table 8). Samples erupted during April 2005, when the extrusion rate was less than $2 \text{ m}^3/\text{s}$ show a wide range in apparent temperature and oxygen fugacity. Six grain pairs in sample SH314-2 are unzoned or weakly zoned; three of these yield average temperatures of $794\text{--}814^\circ\text{C}$, two of $840\text{--}874^\circ\text{C}$, and two grain pairs yield a wide range of temperatures ($726\text{--}821^\circ\text{C}$). The titanomagnetite of one grain pair appears to be reversely zoned (cooled), with lower Ti near the boundary with ilmenite, yielding an apparent temperature for the two core areas of about 872°C but decreasing to 840°C at the boundary. Sample SH315-4 shows an even wider and cooler range in apparent temperatures, with reverse zoning of both titanomagnetite and ilmenite and apparent temperatures ranging from a low of 644°C to a high of 839°C . Sample SH315-4 is also distinct from most of the other samples with respect to a lower oxygen fugacity, extending below

the NNO buffer curve at temperatures below 800°C. As previously noted, we have been unable to obtain meaningful oxide thermobarometry results samples erupted after April 2005 owing to presence of extensive oxidation lamellae.

The lower apparent oxidation state of April 2005 samples may be the result of extensive degassing driving precipitation of oxides and extraction of Fe⁺³ from the melt, thereby lowering fO₂. In addition, as the liquid gains more SiO₂, the increased concentrations of Na₂O and K₂O in the melt would complex with Fe⁺³ and lower its activity, having the same effect of lowering the fO₂. This explanation is consistent with a predicted decrease in oxidation accompanying extensive crystallization at less than 10 MPa pressure by pMELTS modeling (Mark Ghiorso, written commun., 2005).

The progression in time from (1) tightly clustered temperatures and oxygen fugacities for the early erupted samples to (2) zoned oxides indicative of heating to (3) wide-ranging apparent temperatures, reverse zoning, and low oxygen fugacities to (4) development of oxidation lamellae is coincident with a decrease in eruption rate from more than 5 m³/s to less than 2 m³/s and with a decrease in the abundance of glass from as much as 30 percent to less than 10 percent. Consequently, we attribute the changes in the oxides to result from latent heating due to groundmass crystallization, coupled with, and then dominated by, heterogeneous heat loss and vapor transport, and finally by oxidation at the shallowest levels of the conduit and vent.

To answer questions about the source of the explosions of January 16 and March 8, 2005, (Moran and others, this volume, chap. 2; Rowe and others, this volume, chap. 29) we analyzed oxide grain pairs in 11 small tephra fragments from the January 16, 2005, tephra deposit (table 8). All but two of these grain pairs are unzoned, and they each produce tightly clustered temperatures and oxygen fugacities ranging from 780°C at 10^{-13.8} to 930°C at 10^{-11.3}. None of these overlap with the temperature and oxygen fugacity of the initial 2004 dacite samples; however, two of the grain-pairs have zoned titanomagnetite indicative of heating. With grain size about 100 μm, they are larger than the range of 20–40 μm that is typical of the 2004–2006 dacite. From these data, we conclude that most of the dacite tephra fragments in the January 16 tephra are not juvenile, suggesting that this explosion emanated from the margins of the conduit and favoring a phreatic rather than magmatic explosion source. However, the story may be different for the March 8, 2005, explosion. The analyses of oxide grain pairs from this ash result in

temperatures that average 852±22°C, indistinguishable from the initial 2004 dacite temperature of 850±5°C.

Shallow conduit processes – a petrologic synthesis

In figure 21 we summarize petrologic features that explain how and where the conduit magma solidified to become a plug. Viscous and relatively melt-rich dacite magma with approximately 55 percent melt ascended from depth, decompressed, lost volatiles, and began to undergo rapid groundmass crystallization at a depth of about 1 km. The earliest-erupted dacite preserved equilibrium Fe–Ti oxide temperatures of about 850°C, which we assume is the temperature at the top of the source reservoir. With increasing crystallization and decreasing melt fractionation, plagioclase became more sodic (reaching An_{20–25} at final stages), and the crystallizing assemblage was joined by anorthoclase and quartz or tridymite (table 3) at depths of less than 0.5 km. Latent heat evolved during decompression-driven groundmass crystallization raised temperatures above 850°C until magma approached the surface. During the earliest stages of the eruption, when extrusion rates were high, the residual high-silica rhyolite matrix melt quenched through the glass transition, especially near the more rapidly cooling conduit margins, and locally preserved as much as 30 percent glass. However, within the spine interior and during later stages of the eruption when eruption rates were slower, groundmass crystallization continued virtually to completion, producing microcrystalline groundmasses with a granite-minimum composition, and latent heating produced zoned oxides. The petrologic constraints outlined here helped define the pressure and depth of solidification used in the quantitative dynamical model for seismogenic stick-slip extrusion of the solid Mount St. Helens dacite plug of Iverson and others (2006) and Iverson (this volume, chap. 21).

Constraints from petrography, textures, and Fe–Ti oxide thermobarometry

Isotopic data elsewhere in this volume (Kent and others, chap. 35; Cooper and others, chap. 36; Reagan and others, chap. 37) indicate a complex history for the 2004–2006 magma. For example, U–Th series phenocryst model ages vary over time scales of decades to thousands of years, and some crystals have variable initial Sr isotopic ratios. The dacite contains amphiboles with widely varying Al and Fe content, which indicate derivation over a wide range in temperature and

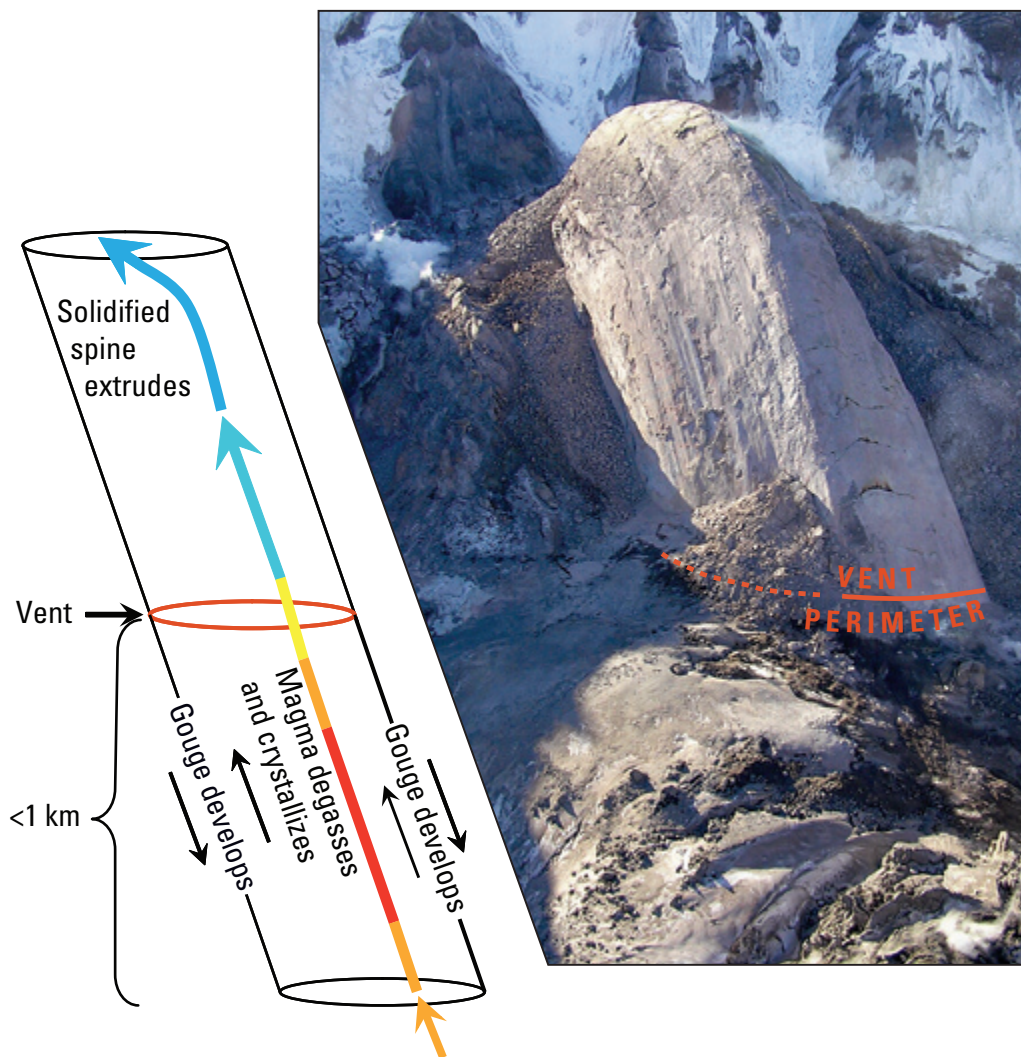


Figure 21. Diagram showing stages in development of a solid spine, drawn approximately to scale, using oblique aerial photograph of spine 4, February 22, 2005. View in photograph is to south-southwest from above east margin of 1980–1986 lava dome. Spine is inclined and is being extruded parallel to slickenside striations, which are formed in meter-thick gouge carapace. Blocky talus flanks spine on east and west and was derived from areas where dome is disintegrating. Bracket indicates depth range of solidification, estimated to be less than 1 km. Colors of arrows represent interval of decompression crystallization, latent heating, and subsequent cooling at the surface.

depth—most readily explained by crystallization during convection of magma over a depth range of about 5 to more than 12 km within the source reservoir (Rutherford and Devine, this volume, chap. 31). In addition, normal and reverse zoning of plagioclase phenocrysts and entrainment of hypersthene microlites in the outer zones of plagioclase resulted from changes in temperature and pressure as magma cycled within a convecting reservoir (Streck and others, this volume, chap. 34). It seems clear that many of the phenocrysts were recycled from previous crystallization episodes and from crystal mush resident in the reservoir.

Modal data and textures described previously (table 2; figs. 4, 5), in combination with isotopic, phase equilibria, and phenocryst relations described above,

indicate multiple stages in the history of the dacite. The phenocryst assemblage of oxides, amphibole, hypersthene, and plagioclase grew slowly in the deep convecting reservoir. Our earliest samples of the 2004 dacite, erupted in October, provide our best constraints on temperature, oxygen fugacity, P_{H_2O} , and depth of magma at the roof of the deep reservoir ($850 \pm 5^\circ\text{C}$ at $fO_2 = 10^{-12.4 \pm 0.1}$, 130 MPa, and about 5 km depth; see also Rutherford and Devine (this volume, chap. 31)). The equilibration depth for 2004 is significantly shallower than the equilibration depth for May 18, 1980, dacite, which by the same method yields a depth of 8.6 ± 1 km (220 ± 30 MPa) (Rutherford, 1993); these differences suggest that the roof of the reservoir became shallower after the 1980 eruption, perhaps related to

the shallowing of storage areas inferred from water contents of melt inclusions in pumice from eruptions in the summer of 1980 (Cashman and McConnell, 2005). A greater abundance of phenocrysts and more sodic plagioclase rims in the 2004–2006 dacite, along with shallower equilibration depths and more evolved bulk composition, is consistent with tapping a shallower and more phenocryst-rich part of the magma reservoir than was tapped in 1980–1986 (Cashman, 1992; Cashman and Taggart, 1983; Geschwind and Rutherford, 1995; Rutherford and others, 1985).

Glass-rich dacite sample SH304-2G initially had all major phenocryst phases, namely plagioclase, hypersthene, amphibole, and Fe–Ti oxides, coexisting with melt at $844\pm 2^\circ\text{C}$ and an oxygen fugacity of $10^{-12.43\pm 0.07}$, overlapping with the temperature and oxygen fugacity of the microcrystalline dacite SH304-2A9 (table 8). The presence of tiny, elongate, hypersthene and oxides (less than $5\ \mu\text{m}$ in diameter; fig. 9D) as the only microlite phases is therefore surprising. At pressures less than about 100 MPa, amphibole is unstable, and one would expect to see plagioclase on the liquidus and crystallizing in the groundmass. In contrast, at high temperatures, the Mount St. Helens dacite composition does have hypersthene first on the liquidus (Rutherford, 1993; Rutherford and Devine, this volume, chap. 31). Could the glassy sample SH304-2G represent magma that was heated during convection in the deep reservoir? Heating would preferentially melt the groundmass phases, such that subsequent cooling and rapid ascent would lead to nucleation of early hypersthene. However, late-stage heating is ruled out by tight clustering of Fe–Ti oxide thermobarometric data at low temperatures in SH304-2G ($844\pm 2^\circ\text{C}$ for 65 analyses of six equilibrium grain pairs) and overlap of these oxide temperatures with those in the microcrystalline dacite, SH304-2A9 ($850\pm 5^\circ\text{C}$). In addition, absence of resorbed margins on plagioclase and amphibole phenocrysts argues against an earlier stage of extensive heating. Consequently, we are left with the interpretation that the absence of plagioclase microlites is a kinetic effect and that SH304-2G is a fragment from the selvage of a vanguard dike that was emplaced to shallow levels and quenched during the earliest phase of the eruption in September 2004.

The presence of extremely rare mafic inclusions in two of the samples indicates mingling and quenching of andesite magma in the dacite at some time during its history. The lack of decompression rims on the high-Al amphiboles of the quenched inclusions, except where they were exposed to the dacite host magma, is consistent with quenching at depths where amphibole was stable ($>100\ \text{MPa}$). The difference in bulk

composition between inclusions SH315-4 and SH321-1, and their small sizes, suggests that these are fragments of larger inclusions, which may display a range in vesiculation and filter-pressing textures (Bacon, 1986). How long small fragments of quenched inclusions can be preserved in convecting, crystal-rich dacite magma is unknown. Their scarcity coupled with the remarkably uniform composition of the 2004–06 dacite suggest that they date from a past mingling event. As discussed later, geophysical and gas data suggest no new magma was added to the reservoir between the summer of 1980 and late 1987, nor between late 1997 and 2004 (Moran, 1994; Moran and others, this volume, chap. 2; Lisowski and others, this volume, chap. 15; Gerlach and others, this volume, chap. 26). However, it is possible that new magma was added during seismic swarms that took place during the period 1987–1997. Consequently, we suggest that these rare inclusions may have been entrained during a period of mingling with hotter and more mafic magma at depth preceding the 1980 eruption or during the repressurization of the reservoir recorded by seismicity between 1987 and 1997 (Moran, 1994).

Constraints from bulk-rock geochemistry

Upper regions of magma reservoirs, by virtue of lower temperature and higher viscosity, may be bypassed during eruptions (Sparks and others, 1984), such that hot, lower-viscosity plumes of magma from lower levels of a reservoir may intrude through overlying magma to be erupted first, only to be followed by higher viscosity magma entrained into the newly established conduit. Such a model was proposed to explain the cycle of initially decreasing and then increasing SiO_2 in 1980–1986 dome lava at Mount St. Helens (Carey and others, 1990; Pallister and others, 1992). However, the difference in minor and trace-element compositions of the 2004–2006 and 1980–1986 dacites, including lower HREE (fig. 19) and higher Ti and Cr (figs. 17, 18), indicate that this magma was not derived by continued closed-system crystallization of 1980 dacite magma. Instead, we suggest that the 2004–2006 magma was derived from a distinct batch of dacite, as explained below.

The rare-earth elements (REE) abundances in Mount St. Helens rocks are especially informative because they decrease in abundance with increasing SiO_2 . Owing to their overall incompatibility in major phenocryst phases, the decrease in abundance cannot be explained by major-phase crystal fractionation (Pallister and others, 1992; Smith and Leeman, 1987). The highest REE abundances in recent Mount St. Helens magmas are in mafic magmas

(basalts and basaltic andesites) erupted during the Castle Creek period, about 2,000 years ago (fig. 19). This factor, as well as other geochemical and petrologic trends in Mount St. Helens magmas, are most readily explained by variable amounts of mixing between dacite (derived by partial melting of lower crustal metabasaltic rocks) and mafic magma enriched in high field-strength elements (HFSE) and REE (Gardner and others, 1995b; Pallister and others, 1992; Smith and Leeman, 1987, 1996). The 2004–2006 dacites have the lowest heavy REE abundances seen at Mount St. Helens during the past 500 years. Consequently, they appear to be the least contaminated by mixing with REE- and HFSE-enriched basaltic magmas. Like other Mount St. Helens dacites, the 2004–2005 samples have several characteristics that have been attributed to adakites (Defant, 1993; Drummond and Defant, 1990), such as high SiO₂, Al₂O₃, and Na₂O, low Y and Yb, and relatively high Sr (about 400 ppm), and they lack or have only small Eu anomalies. However, they are not as enriched in LREE as adakites (with La/Yb ratios of about 10, as opposed to ratios greater than 20 in the archetypical adakite). The same residual phases responsible for depletion of the HREE (garnet, amphibole, and pyroxene) are also expected at the base of the crust, a source we prefer, as it does not require transport of the dacite through a hot mantle wedge without modification (Dawes and others, 1994). Consequently, we do not consider the Mount St. Helens dacites as partial melts of slab eclogites but more likely as melts of lower crustal metabasaltic rocks that have undergone variable amounts of crystallization and geochemical modification in the shallow crustal reservoir beneath the volcano (Smith and Leeman, 1987).

Regardless of the ultimate source of the 2004–2006 dacite, its distinct TiO₂, Cr, and HREE abundances suggest that either it is an entirely new batch of dacite magma from the deep crust or it is derived from a geochemically isolated region of a crustal reservoir. The question of new versus residual magma has implications for the long-term eruptive behavior of Mount St. Helens, as arrival of a new batch of dacitic magma from the deep crust could herald the beginning of a new long-term cycle of eruptive activity (Pallister and others, 2005). Despite the heterogeneity in phenocryst ages and zoning history, the erupted magma is remarkably homogeneous in bulk composition, indicating that this batch of magma is well mixed. Although we cannot rule out the possibility that a batch of dacite magma from the deep crust is involved in the current eruption, the low levels of gas emissions (Gerlach and others, this volume, chap. 26), U-series evidence for multiple ages of crystals (Cooper and others, this volume, chap. 36), and

the wide range in crystallization depths of phenocrysts, indicative of convection (Rutherford and Devine, this volume, chap. 31), leads us to favor the hypothesis that the 2004–2006 magma is derived from a geochemically distinct batch of magma that had accumulated recently at the apex of the crustal magma reservoir. This magma had been depleted in SO₂ and CO₂ during multiple cycles of reservoir convection, as explained in the section below on eruption triggering.

An updated reservoir and conduit model

In figure 22 we update a diagrammatic cross section of the Mount St. Helens magmatic system that was drawn on the basis of seismic, petrologic, and deformation data (Pallister and others, 1992; Scandone and Malone, 1985). The principal changes to the diagram from a 1980s interpretation are listed here.

(1) The top of the reservoir is raised from about 6 km to a depth of about 5 km on the basis of the equilibration pressure of 130 MPa for the 2004–2006 magma (Rutherford and Devine, this volume, chap. 31). Assuming that magma ascent was accompanied by an increase in pressure in the reservoir and not accomplished simply by collapse of the roof into the magma, this top-of-reservoir level is bracketed by seismic and deformation data to the time interval 1987–1997, as described below.

(2) The geometry of the conduit from 5 km to the surface is poorly constrained. It may consist of a complex of dikes and irregular intrusions that represent the conduit pathways of previous eruptions (suggested by textural and petrologic evidence that the 1980–86 dome lavas experienced a multi-stage decompression history; Cashman, 1992). However, because of the distinct and uniform dacite composition, consistency of amphibole reaction rim thicknesses, and continuous eruption, the 2004–2006 eruption is thought to have established a new conduit pathway, at least partly distinct from that of the 1980–86 dome-forming eruptions. But how was a new conduit emplaced without large-scale inflation prior to the eruption? One possibility is that uplift of the crater glacier during the period between September 23 and October 11, 2004, recorded extrusion under the glacier of solidified rock from the 1980–86 conduit. Uplift of 12×10^6 m³ was recorded during this period before the first spine emerged (Schilling and others, this volume, chap. 8). Such a model would help explain the presence “crater floor” samples that are geochemically similar to 1985 or 1986 dacite, bits of which were uplifted with the glacier and sampled on October 20 and 27, 2004 (table 1).

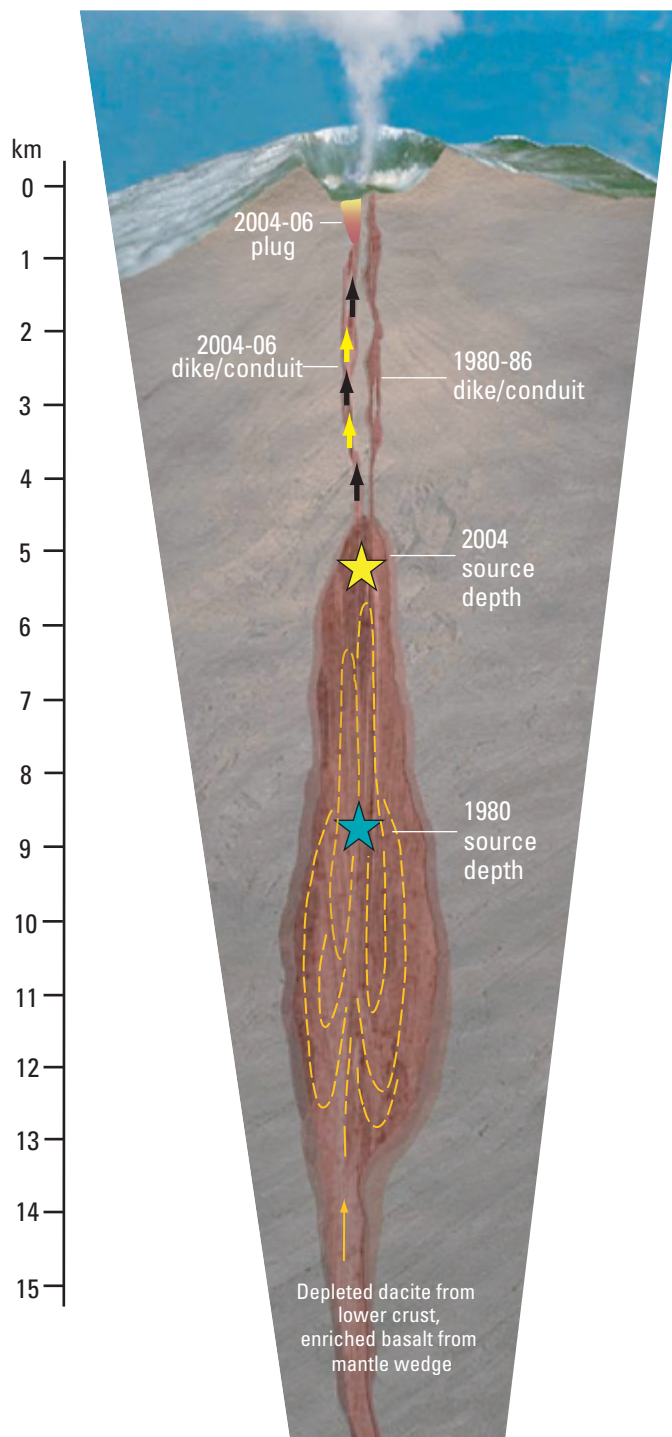


Figure 22. Schematic cross section of Mount St. Helens plumbing system, updated to include constraints from current eruption. Yellow dashed lines are inferred convection paths in reservoir (Rutherford and Devine, this volume, chap. 31) and are overlain by a stagnant crystal-rich mush zone considered as the source for the 2004–2006 eruption. Depth scale in kilometers below crater floor.

(3) We reduce the model size of the reservoir to a magma volume of about 4 to 5 km³, a compromise between the smaller volumes inferred from seismic data (Lees, 1992; Moran, 1994; Musumeci and others, 2001) and magma volumes of as much as 8 km³, which are suggested by eruptive volumes of the largest historical eruptions at Mount St. Helens. The largest plinian eruptions of the past 4000 years had magmatic volumes of 4 km³ (Yn tephra) and 2 km³ (Wn tephra) (Carey and others, 1995). We suggest that it is reasonable to at least double erupted volumes to derive reservoir volumes on the assumption that individual explosive (but noncaldera-forming) eruptions are unlikely to withdraw more than half of their shallow crustal reservoir volumes without extensive surface deformation or caldera collapse. The presence of a continuous magma reservoir within the seismically defined depth range between about 5 and greater than 12 km during the past 4000 years is based on variation in depths of equilibration of magmas erupted during this time span, including changes in equilibration depths of as much as 6 km in less than 3 years (Gardner and others, 1995c). In addition, conductive cooling models suggest cooling times on the order of several thousand years for magma reservoir volumes of these depths and volumes (see Hawkesworth and others, 2000). That the magma reservoir is spatially continuous over its depth range and convecting, rather than discontinuous as in Lees' (1992) model, is consistent with the petrologic evidence of large-scale convection cited above and with new seismic tomographic modeling, which indicates a continuous reservoir over the interval between 6 and at least 10 km³ (Waite, 2006).

We follow Gardner and others (1995c) in interpreting the rapid change in equilibration depths for successive eruptions at Mount St. Helens to reflect tapping of different levels of the reservoir at different times. Such would appear to be the case for the source regions for the 2004–2006 magma (130 MPa, about 5.2 km) compared to the 1980 magma (220 MPa, about 8.6 km) (Rutherford, 1993; Rutherford and Devine, this volume, chap. 31). An increase in seismicity at depths of 3 to 10 km, including an initial cluster at 4–6 km, and accompanying repressurization of the reservoir and conduit between 1987 and 1992 (Moran, 1994), may reflect foundering of the roof of the reservoir and migration of a batch of magma to the shallower equilibration depths. As noted above, we suggest that the 2004–2006 dacite was derived from the apical region of the reservoir. It originated from a geochemically distinct batch of crystal-rich magma not tapped during the 1980–86 eruptions that rose into the apical region after 1986.

The deep levels of the reservoir probably occupy a tensional dike-like structure within the St. Helens seismic zone (Musumeci and others, 2002), and the 1980–86 conduit may well consist of multiple intrusions and dikes (Cashman, 1992). However, unlike the situation at other volcanic centers (for example, Eichelberger and Izbekov, 2000), we see little surface geologic evidence for extensive dacitic dikes at shallow levels outside of the immediate crater area or alignment of older satellitic domes.

Studies of the plutonic substrate of volcanic arcs offer additional insights. Composite arc plutons and stocks with volumes of 10 km³ or more are common at paleodepths of 5–15 km, and arc batholiths, such as in the Sierra Nevada, are increasingly recognized to consist of multiple smaller magma bodies. However, many of these plutonic complexes developed over time spans measured in millions of years, not over a period of less than 300,000 years (Clynne and others, this volume, chap. 28; Crandell, 1987) in the tensional offset of a fault zone (Weaver and others, 1987). A better analogue for the Mount St. Helens plumbing system comes from a composite stratovolcano model based on ore deposits in the Andes (Sillitoe, 1973). Sillitoe's composite model is similar to figure 22, and consists of a complex composite stock of multiple feeder dikes and plugs of various ages overlying a shallow crustal pluton. We recognize that diagrams such as figure 22 are at best oversimplified cartoons compared to the complexity seen in eroded volcanic terranes, yet we believe they serve as useful constructs to evaluate volcano monitoring and petrologic data and to consider how magmas move through the crust.

Reservoir pressurization and eruption triggering

One of the most important questions in volcanology and hazard mitigation is to understand what triggers eruptions. But before addressing this question for the 2004–2006 Mount St. Helens eruption, we need to define what we mean by triggering. A pressurized reservoir-conduit system is a necessary condition for an eruption; but it is not a trigger, because pressure can be released slowly—for example, through passive degassing. A trigger requires a rapid increase in relative pressure of sufficient magnitude to fracture a new pathway to the surface (for a volcano with a solidified conduit or hydrothermal seal) or to raise the level of magma above the vent in an active magma-filled conduit. Accordingly, triggers can result by unloading from above or from a rapid increase in pressure or volume at depth. Candidates

for triggers from above include edifice collapse (as in 1980 at Mount St. Helens) or more subtle changes affecting an already pressurized system (an example: increased rainfall, Mastin, 1994). Indeed, Iverson and others (2006) calculate that once the system is pressurized, changes in pressure that are equivalent to a magma head of less than one meter are sufficient to start and stop the stick-slip cycles that they model for the current Mount St. Helens eruption.

Rapid addition of new magma and fluids to a crustal reservoir can increase pressure and trigger an eruption from below. This was the case for the eruption of Pinatubo in 1991, in which ascent of new hydrous mafic magma from depth entered a crystal-rich dacite reservoir, vesiculated, mingled, and created a buoyant plume, which rose through the viscous and crystal-rich upper part of the reservoir, increased pressure in the hydrothermal system, fractured a new pathway to the surface, and triggered the eruption (Pallister and others, 1996). In the Pinatubo case, deep long-period seismicity recorded and tracked ascent of basalt from 35 or 40 km to the crustal reservoir at depths of less than 14 km before the eruption (White, 1996).

For the 2004 Mount St. Helens eruption, the long-term pattern of seismicity since the 1980 eruption indicates that the reservoir and conduit system began to repressurize in late 1987 after the cessation of 1980–86 dome eruptions (Moran, 1994; Musumeci and others, 2001). Pressurization led to repeated seismic swarms at depths of less than about 8 km, and rainfall induced fracturing which weakened hydrothermal seals and triggered small gas explosions in 1989–1991 (Mastin, 1994). Only a few deep (>3 km) earthquakes were located in the months before the 2004 eruption, and there have been no deep earthquakes during the 2004–2006 eruptive period; the hundreds of thousands of small hybrid earthquakes that accompanied spine extrusion have been shallow (Moran and others, this volume, chap. 2; Thelen and others, this volume, chap. 4). These relations indicate that the reservoir-conduit system was already pressurized prior to the eruption. The highest rate of seismic energy release took place during the September 30–October 5, 2004, time period of shallow volcano-tectonic earthquakes and explosions that preceded extrusion of the initial spine (Moran and others, this volume, chap. 2). Given the small amount of pressure required for the hypothesized stick-slip cycles of spine extrusion (Iverson and others, 2006; Iverson, this volume, chap. 21), this initial period of greater energy release in early October 2004 indicates that the trigger for the eruption involved a somewhat larger pressure differential, which was accompanied by upward

migration and venting of overpressured hydrothermal fluids.

Pressurization of a magma reservoir may result either from addition of mass (replenishment) or by fluid exsolution and expansion (driven by cooling and/or decompression). Long-term magmatic replenishment and magma mixing is a characteristic of the past at Mount St. Helens (Pallister and others, 1992; Gardner and others, 1995a; Clynne and others, this volume, chap. 28). However, as previously noted, the paucity of mafic inclusions, homogeneity of the dacite composition, lack of deep seismicity, and the low levels of gas emissions argue against ongoing (2004–2006) replenishment, as does a lack of volcanic deformation during the period between at least as early as late 1997 (when continuous GPS monitoring was established) and late September 2004 (Lisowski and others, this volume, chap. 15).

Deformation data for the current eruption are best fit by an ellipsoidal reservoir with a centroid depth of 7 to 8 km (Lisowski and others, this volume, chap. 15) and are consistent with both recent seismic tomography models (Waite, 2006) and with the petrologic constraints outlined above. However, the volume of erupted dacite falls short of the modeled volume decrease at depth, requiring either magmatic replenishment or expansion of the reservoir (Lisowski and others, this volume, chap. 15). Geochemical modeling of gas emission data suggests about 1.2–1.4 vol. percent separate fluid phase at 220 MPa (about 8.6 km depth), which would increase to about 9–10 vol. percent at 130 MPa (5.2 km), near the apex of the magma reservoir (Gerlach and others, this volume, chap. 26). Modeling of magma and wall-rock physical properties (Mastin and others, this volume, chap. 22) to match the geodetically constrained rate of change in eruptive volume indicates only limited magma compressibility (low average volatile content of less than 2 volume percent) and a large magma reservoir (a few to as much as 10 km³), consistent with the recent seismic tomography (Waite, 2006). The modeling by Mastin and others of deformation data from the first 1.5 year (this volume, chap. 22) also favors ongoing magmatic replenishment at a rate of about 1–1.4 m³/s. On balance, and given the uncertainties in the models, at this time it remains uncertain if the reservoir is being recharged, if the fluid phase in the reservoir is expanding, or both. Furthermore, if the reservoir is being recharged from below and erupted from the top, any significant additions of SO₂ and CO₂ gases have not yet made their way through the >10-km vertical extent of magma in the reservoir and conduit system to the surface.

A petrologic explanation

Magma in the upwelling limbs of convection cells exsolves volatiles due to their reduced solubility in the silicate melt on ascent to lower pressures. Therefore, without addition of new volatile-rich magma at depth, magma in a convecting reservoir will be progressively depleted by multiple convection cycles as volatiles in upwelling magma are lost to overlying stagnant magma and reservoir roof rocks. Any nonconvecting magmatic mush present at the roof of the reservoir would either be enriched or depleted in volatiles, depending on the ratio of volatile addition from upwelling magma to volatile loss through wall and roof rocks. During periods of frequent or continuous magmatic replenishment of the deep reservoir by hot and gas-rich magmas, enhanced convection would tend to enrich an upper mush zone in volatiles. During such periods, undercooling of newly introduced magmas at depth could also produce highly gas-rich plumes of buoyant mingled magma. Energetic plumes would be capable of penetrating and mobilizing previously gas-enriched mush in the reservoir roof to trigger large explosive eruptions. Evidence for such a process is seen in the eruptive products of Pinatubo volcano (Pallister and others, 1996) and is suggested by the presence of mingled pumices found in the basal W-set tephra from the A.D. 1479 explosive eruption of Mount St. Helens, which initiated the Kalama eruptive period (Pallister and others, 1992). In contrast, in the absence of replenishment (or with diminished volumes of replenishment), continued convection would slowly deplete the reservoir in the lower-solubility volatiles, and the magmatic fluid phase would shift from relatively SO₂- and CO₂-rich to H₂O- and Cl-rich compositions.

This latter condition is what we propose for the current eruption of Mount St. Helens. Since 1980, the magma reservoir has seen minimal replenishment, such that convection has produced a batch of well-mixed, crystal-rich 65 percent SiO₂ magma near the reservoir roof. A slow increase in pressure was brought about beginning in late 1987 by convection-driven exsolution of a water-rich volatile phase (which outpaced volatile losses through roof rocks). Magmatic pressure finally exceeded lithostatic load in late September 2004, and the eruption ensued. As conduit pressures during the 2004–2006 eruption have not greatly exceeded lithostatic pressure and have been modulated by continuous crystallization of a shallow seismogenic plug (Iverson and others, 2006; Iverson, this volume, chap. 21), the eruption has been sustained at a low nonexplosive rate.

Lessons from the past, implications for the future

Of dacites erupted at Mount St. Helens during the past 500 years, the 17th-18th century summit dome dacite (63–64 percent SiO₂), which erupted at the end of the Kalama eruptive period and formed the pre-1980 summit of the volcano (Crandell, 1987; Mullineaux, 1996; Pallister and others, 1992), is most akin to the current dacite. Summit dome samples are characterized by extensive groundmass crystallization, resulting in a vesicle- and glass-poor microcrystalline groundmass. Although geochemically distinct from the 2004–2006 dacite and texturally finer grained, the summit dome dacite has numerous similarities with it. Like the 2004–2006 eruption, the summit dome eruptions were relatively low in explosivity, producing only one pumiceous pyroclastic flow down the Toutle River drainage in early summit dome time (R.P. Hoblitt, oral commun., 2006). The dominant deposits from the summit dome originated from small lithic pyroclastic flows and hot lahars, which were shed off the growing and collapsing lava dome, blanketed the upper slopes of the volcano, and fed multiple small lahars that spread out onto the flanks of the volcano. The nonpumiceous pink “z” ash (Mullineaux, 1996) is the only tephra layer associated with summit dome eruptions. It occurs as a thin (typically less than 1 cm) ash deposit on all flanks of the volcano and was likely derived from small ash clouds produced during dome collapse events over an extended period of time. And, like some of the 2004–2006 dome rocks, lithic fragments in summit dome deposits are characterized by red oxidation fractures and rinds.

The greater extent of summit dome deposits is a consequence of prolonged emplacement over 100 years or more (Clynne, 2005; Hoblitt, 1989; Yamaguchi and Hoblitt, 1995), large volume, and its location high atop the steep-sided cone. We do not know if the summit dome was built as a series of spines, for such features are rarely preserved in the geologic record. However, the summit dome was clearly built at a low mean eruptive rate. It spalled and disintegrated in place, forming the rubbly pre-1980 summit, and it shed multiple lithic pyroclastic flows and lahars. It produced only relatively small and diffuse ash clouds, similar to those produced during the 2004–2006 eruption. If the current eruption were to follow a similar path, it could produce continuous or intermittent dome-forming eruptions for decades. Although low eruption rates do not guarantee a long-duration episode, a global compilation of historical dome-forming eruptions indicates that only low-rate

eruptions last for many years or decades (Chris Newhall, written commun., 2005).

Acknowledgments

The authors wish to acknowledge the several dozen petrologists and geochemists from a variety of academic and government institutions who joined us during the ongoing eruption to form an informal Mount St. Helens petrology working group (Pallister and others, 2005; Rowe and others, in press). The contributions of these scientists are well represented in this volume and contribute greatly to our understanding of the ongoing eruption. We thank our USGS colleagues from the Cascades Volcano Observatory (CVO) and other USGS offices and from the Pacific Northwest Seismic Network at the University of Washington for sharing of data and a stimulating discussion of ideas and interpretations, which have made our work on this eruption scientifically stimulating and rewarding. We thank Bobbie Myers of CVO and Jeff Linscott of JL Aviation for their emphasis on safety as well as innovation during our helicopter missions at Mount St. Helens. And finally, we thank Charlie Bacon and Malcolm Rutherford for technical reviews of this manuscript.

References Cited

- Andersen, D.H., and Lindsay, J.R., 1988, Internally consistent solution models for Fe-Mg-Mn-Ti oxides: *American Mineralogist*, v. 73, p. 714–726.
- Bacon, C.R., 1986, Magmatic inclusions in silicic and intermediate volcanic rocks: *Journal of Geophysical Research*, v. 91, no. B6, p. 6091–6112.
- Bacon, C.R., and Hirschmann, M.M., 1988, Mg/Mn partitioning as a test for equilibrium between coexisting Fe-Ti oxides: *American Mineralogist*, v. 73, p. 57–61.
- Baedecker, P.A., and McKown, D.M., 1987, Instrumental Neutron Activation Analysis of geochemical samples, *in* Baedecker, P.A. ed., *Methods for geochemical analysis: U.S. Geological Survey Bulletin 1770*, p. H1–H14.
- Blundy, J., and Cashman, K., 2006, Rapid decompression-driven crystallisation recorded by melt inclusions from Mount St. Helens volcano: *Geology*, v. 33, p. 793–796.
- Blundy, J., Cashman, K., and Humphreys, M., 2006, Magma heating by decompression-driven crystallization beneath andesite volcanoes: *Nature*, v. 443, p. 76–80.

- Blundy, J., and Cashman, K.V., 2001, Ascent-driven crystallization of dacite magmas at Mount St. Helens, 1980–86: *Contributions to Mineralogy and Petrology*, v. 140, p. 631–650.
- Carey, S., Gardner, J., and Sigurdsson, H., 1995, The intensity and magnitude of Holocene plinian eruptions of Mount St. Helens volcano: *Journal of Volcanology and Geothermal Research*, v. 66, p. 185–202.
- Carey, S., Sigurdsson, H., Gardner, J.E., and Criswell, W., 1990, Variations in column height and magma discharge during the May 18, 1980 eruption of Mount St. Helens: *Journal of Volcanology and Geothermal Research*, v. 43, p. 99–112.
- Cashman, K.V., 1988, Crystallization of Mount St. Helens 1980–1986 dacite: A quantitative textural approach: *Bulletin of Volcanology*, v. 50, p. 194–209.
- Cashman, K.V., 1992, Groundmass crystallization of Mount St. Helens dacite, 1980–1986: a tool for interpreting shallow magmatic processes: *Contributions to Mineralogy and Petrology*, v. 109, p. 431–449.
- Cashman, K.V., and McConnell, S.M., 2005, Multiple levels of magma storage during the 1980 summer eruptions of Mount St. Helens, WA: *Bulletin of Volcanology*, v. 68, p. 57–75.
- Cashman, K.V., and Taggart, J.E., 1983, Petrologic monitoring of 1981 and 1982 eruptive products from Mount St. Helens: *Science*, v. 221, p. 1385–1387.
- Cashman, K., Thornber, C.R., and Pallister, J.S., 2007, From dome to dust: shallow crystallization and fragmentation of conduit magma during the 2004–2006 dome extrusion of Mount St. Helens, Washington, *in* Sherrod, D.R., Scott, W.E., and Stauffer, P.H., eds., *A volcano rekindled: the first year of renewed eruptions at Mount St. Helens, 2004–2006*: U.S. Geological Survey Professional Paper (this volume).
- Charlier, B.L.A., Wilson, C.J.N., Lowenstern, J.B., Blake, S., Van Calsteren, P.W., and Davidson, J.P., 2005, Magma generation at a large, hyperactive silicic volcano (Taupo, New Zealand) revealed by U–Th and U–Pb systematics in zircons: *Journal of Petrology*, v. 46, p. 3–32.
- Chrétien, S., and Brousse, R., 1989, Events preceding the great eruption of 8 May, 1902 at Mount Pelee, Martinique: *Journal of Volcanology and Geothermal Research*, v. 38, p. 67–75.
- Clynne, M.A., 2005, Pre-1980 eruptive history of Mount St. Helens, Washington: U.S. Geological Survey Fact Sheet 3045, 4 p.
- Clynne, M.A., Calvert, A.T., Wolfe, E.W., Evarts, R.C., Fleck, R.J., and Lanphere, M.A., 2007, The pre-Spirit Lake eruptive history of Mount St. Helens, Washington: A compilation of literature and new geochronologic and geochemical data integrated with stratigraphy, chap. 28 *in* Sherrod, D.R., Scott, W.E., and Stauffer, P.H., eds., *A volcano rekindled: the first year of renewed eruptions at Mount St. Helens, 2004–2006*: U.S. Geological Survey Professional Paper (this volume).
- Cooper, K.M., and Donnelly, C.T., 2007, ^{238}U - ^{230}Th - ^{226}Ra disequilibria in the 2004–2005 eruption of Mount St. Helens, *in* Sherrod, D.R., Scott, W.E., and Stauffer, P.H., eds., *A volcano rekindled: the first year of renewed eruptions at Mount St. Helens, 2004–2006*: U.S. Geological Survey Professional Paper (this volume).
- Costa, F., Dungan, M. A., and Singer, B. S., 2002, Hornblende- and phlogopite-bearing gabbroic xenoliths from Volcán San Pedro (36°S), Chilean Andes: evidence for melt and fluid migration and reactions in subduction-related plutons: *Journal of Petrology*, v. 43, no. 2, p. 219–241.
- Couch, S., Harford, C.L., Sparks, R.S.J., and Carroll, M.R., 2003, Experimental constraints on the conditions of formation of highly calcic plagioclase microlites at the Soufriere Hills Volcano, Montserrat: *Journal of Petrology*, v. 44, no. 8, p. 1455–1475.
- Crandell, D., 1987, Deposits of pre-1980 pyroclastic flows and lahars from Mount St Helens volcano, Washington: USGS Professional Paper 1444, 91 p.
- Dawes, R.L., Green, N.L., Defant, M.J., and Drummond, M.S., 1994, Mount St. Helens: potential example of the partial melting of the subducted lithosphere in a volcanic arc: *Comments and Reply: Geology*, v. 22, p. 187–190.
- Defant, M.J., 1993, Mount St. Helens: Potential example of the partial melting of the subducted lithosphere in a volcanic arc: *Geology*, v. 21, p. 547–550.
- Devine, J.D., Rutherford, M.J., Norton, G.E., and Young, S.R., 2003, Magma storage region processes inferred from Fe-Ti oxides in andesitic magma, Soufrière Hills Volcano, Montserrat, W.I.: *Journal of Petrology*, v. 44, no. 8, p. 1375–1400.
- Devine, J.D., Sigurdsson, H., Davis, A.N., and Self, S., 1984, Estimates of sulfur and chlorine yield to the atmosphere from volcanic eruptions and potential climatic effects: *Journal of Geophysical Research*, v. 89, no. B7, p. 6309–6325.
- Dixon, J.E., Stolper, E.M., and Holloway, J.R., 1995, An experimental study of H₂O and carbon dioxide solubilities in mid-ocean ridge basaltic liquids. Part I: Calibration and solubility results: *Journal of Petrology*, v. 36, p. 1607–1631.
- Drummond, M.S., and Defant, M.J., 1990, A model for trondhjemite-tonalite-dacite genesis and crustal growth via slab-melting: Archean to modern comparisons: *Journal of Geophysical Research*, v. 95, p. 21503–21521.
- Dzurisin, D., Lisowski, M., Poland, M.P., Sherrod, D.R., and LaHusen, R.G., 2007, Constraints and conundrums posed by ground deformation measurements during the 2004–2006 dome-building eruption of Mount St. Helens, Washington, chap. 14 *in* Sherrod, D.R., Scott, W.E., and Stauffer, P.H., eds., *A volcano rekindled: the first year of renewed eruptions at Mount St. Helens, 2004–2006*: U.S. Geological Survey Professional Paper (this volume).
- Edmonds, M., McGee, K.A., and Doukas, M., 2007, Chlorine

- degassing during the lava dome-building eruption of Mount St. Helens, 2004–2005, chap. 27 *in* Sherrod, D.R., Scott, W.E., and Stauffer, P.H., eds., *A volcano rekindled: the first year of renewed eruptions at Mount St. Helens, 2004–2006*: U.S. Geological Survey Professional Paper (this volume).
- Edmonds, M., Pyle, D., and Oppenheimer, C., 2001, A model for degassing at the Soufrière Hills Volcano, Montserrat, West Indies, based on geochemical data: *Earth and Planetary Science Letters*, v. 186, no. 2, p. 159–173.
- Eichelberger, J.C., and Izbekov, P.E., 2000, Eruption of andesite triggered by dyke injection: contrasting cases at Karymsky Volcano, Kamchatka and Mt Katmai, Alaska: *Philosophical Transactions of the Royal Society A: Mathematical, Physical and Engineering Sciences*, v. 358, no. 1770, p. 1465–1485.
- Gardner, J.E., Carey, S., Rutherford, M.J., and Sigurdsson, H., 1995a, Petrologic diversity in Mount St. Helens dacites during the last 4,000 years; implications for magma mixing: *Contributions to Mineralogy and Petrology*, v. 119, no. 2–3, p. 224–238.
- Gardner, J.E., Carey, S., Sigurdsson, H., and Rutherford, M.J., 1995b, Influence of magma composition on the eruptive activity of Mount St. Helens, Washington: *Geology*, v. 23, no. 6, p. 523–526.
- Gardner, J.E., Rutherford, M., Carey, S., and Sigurdsson, H., 1995c, Experimental constraints on pre-eruptive water contents and changing magma storage prior to explosive eruptions of Mount St Helens Volcano: *Bulletin of Volcanology*, v. 57, no. 1, p. 1–17.
- Gerlach, T.M., McGee, K.A., and Doukas, M., 2007, CO₂, SO₂, and H₂S emissions at Mount St. Helens, 2004–2005: Depletion of excess volatiles and the role of scrubbing, chap. 26 *in* Sherrod, D.R., Scott, W.E., and Stauffer, P.H., eds., *A volcano rekindled: the first year of renewed eruptions at Mount St. Helens, 2004–2006*: U.S. Geological Survey Professional Paper (this volume).
- Geschwind, C.-H., and Rutherford, M.J., 1995, Crystallization of microlites during magma ascent; the fluid mechanics of 1980–1986 eruptions at Mount St Helens: *Bulletin of Volcanology*, v. 57, no. 5, p. 356–370.
- Ghiorso, M.S., Hirschmann, M.M., Reiners, P.W., and Kress, V.C., 2002, The pMELTS: A revision of MELTS for improved calculation of phase relations and major element partitioning related to partial melting of the mantle to 3 GPa: *Geochemistry, Geophysics, Geosystems*, v. 3, no. 5, doi: 10.1029/2001GC000217, 36 p.
- Harford, C.L., Sparks, R.S.J., and Fallick, A.E., 2003, Degassing at the Soufrière Hills Volcano, Montserrat, recorded in matrix glass compositions: *Journal of Petrology*, v. 44, no. 8, p. 1503–1523.
- Hawkesworth, C.J., Blake, S., Evans, P., Hughes, R., Macdonald, R., Thomas, L.E., Turner, S.P., and Zellmer, G., 2000, Time scales of crystal fractionation in magma chambers—integrating physical, isotopic and geochemical perspectives: *Journal of Petrology*, v. 41 Number, no. 7, p. 991–1006.
- Heliker, C., 1995, Inclusions in Mount St. Helens dacite erupted from 1980 through 1983: *Journal of Volcanology and Geothermal Research*, v. 66, nos. 1–4, p. 115–135.
- Herriott, T.M., Sherrod, D.R., Pallister, J.S., and Vallance, J.W., 2007, Photogeologic maps of the 2004–2005 Mount St. Helens eruption, chap. 10 *in* Sherrod, D.R., Scott, W.E., and Stauffer, P.H., eds., *A volcano rekindled: the first year of renewed eruptions at Mount St. Helens, 2004–2006*: U.S. Geological Survey Professional Paper (this volume).
- Hoblitt, R.P., 1989, The Kalama eruptive period, southwest and south flanks, *in* Field excursions to volcanic terranes in the western United States II: Cascades and Intermountain West: New Mexico Bureau of Mines and Mineral Resources Memoir, v. 47, p. 65–69.
- Hoblitt, R.P., and Harmon, R.S., 1993, Bimodal density distribution of cryptodome dacite from the 1980 eruption of Mount St. Helens, Washington: *Bulletin of Volcanology*, v. 55, p. 421–437.
- Ihinger, P.D., Hervig, R.L., and McMillan, P.F., 1994, Analytical methods for volatiles in glasses, *in* Carroll, M.R., and Holloway, J.R., eds., *Volatiles in magmas*: Washington D.C., *Reviews in Mineralogy and Geochemistry*, v. 30, p. 67–121.
- Iverson, R.M., 2007, Rheology of the 2004–05 MSH dacite and implications for magma dynamics: U.S Geological Survey Professional Paper, chap. 21 *in* Sherrod, D.R., Scott, W.E., and Stauffer, P.H., eds., *A volcano rekindled: the first year of renewed eruptions at Mount St. Helens, 2004–2006*: U.S. Geological Survey Professional Paper (this volume).
- Iverson, R.M., Dzurisin, D., Gardner, C.A., Gerlach, T.M., LaHusen, R.G., Lisowski, M., Major, J.J., Malone, S.D., Messerich, J., Moran, S.C., Pallister, J.S., Qamar, A.I., Schilling, S.P., and Vallance, J.W., 2006, Dynamics of seismogenic volcanic extrusion at Mount St. Helens in 2004–2005: *Nature*, v.444, p.439–443.
- Jackson, E.D., 1968, The character of the lower crust and upper mantle beneath the Hawaiian Islands: *Proceedings of the 23rd International Geological Congress*, v. 1, p. 131–150.
- Kent, A.J.R., Rowe, M.C., Thornber, C.R., and Pallister, J.S., 2007, Trace element and Pb isotope composition of plagioclase from dome samples from the 2004–2005 eruption of Mount St. Helens, Washington, chap. 35 *in* Sherrod, D.R., Scott, W.E., and Stauffer, P.H., eds., *A volcano rekindled: the first year of renewed eruptions at Mount St. Helens, 2004–2006*: U.S. Geological Survey Professional Paper (this volume).
- Lacroix, A., 1904, *La Montagne Pelé et ses éruptions*: Paris.
- LaHusen, R.G., Swinford, K., Logan, M., and Lisowski, M., 2007, Instrumentation in remote and dangerous settings: an example from GPS deployments during the 2004–2005 renewed eruption of Mount St. Helens, chap. 16 *in* Sherrod,

- D.R., Scott, W.E., and Stauffer, P.H., eds., A volcano rekindled: the first year of renewed eruptions at Mount St. Helens, 2004–2006: U.S. Geological Survey Professional Paper (this volume).
- Lees, J.M., 1992, The magma system of Mount St. Helens: non-linear high resolution P-wave tomography: *Journal of Volcanology and Geothermal Research*, v. 53, no. 1–4, p. 103–116.
- Lepage, L.D., 2003, ILMAT: an Excel worksheet for ilmenite-magnetite geothermometry and geobarometry: *Computers and Geosciences*, v. 29, p. 673–678.
- Lisowski, M., LaHusen, R.G., Schilling, S.P., Denlinger, R., and Iwatsubo, E.Y., 2007, Using continuous and campaign GPS measurements to interpret deep structural changes in the volcano, chap. 15 in Sherrod, D.R., Scott, W.E., and Stauffer, P.H., eds., A volcano rekindled: the first year of renewed eruptions at Mount St. Helens, 2004–2006: U.S. Geological Survey Professional Paper (this volume).
- Mandeville, C.W., Webster, J.D., Rutherford, M.J., Taylor, B.E., Timbal, A., and Faure, K., 2002, Determination of molar absorptivities for infrared absorption bands of H₂O in andesitic glasses: *American Mineralogist*, v. 87, p. 813–821.
- Mastin, L.G., 1994, Explosive Tephra Emissions at Mount St. Helens, 1989–1991: The Violent Escape of Magmatic Gas Following Storms?: *Geological Society of America Bulletin*, v.106, p.175–185
- Mastin, L.G., Roeloffs, E., Beeler, N.M., and Quick, J.E., 2007, Constraints on the size, overpressure, and volatile content of the Mount St. Helens magma system from geodetic and dome-growth measurements during the 2004–2006 eruption, chap. 22 in Sherrod, D.R., Scott, W.E., and Stauffer, P.H., eds., A volcano rekindled: the first year of renewed eruptions at Mount St. Helens, 2004–2006: U.S. Geological Survey Professional Paper (this volume).
- McChesney, P.J., Couchman, M., Moran, S.C., Lockhart, A.B., Swinford, K., and LaHusen, R.G., 2007, Seismic monitoring deployments and instrument development (seismic spider) at Mount St. Helens 2004–2005, chap. 7 in Sherrod, D.R., Scott, W.E., and Stauffer, P.H., eds., A volcano rekindled: the first year of renewed eruptions at Mount St. Helens, 2004–2006: U.S. Geological Survey Professional Paper (this volume).
- Melnik, O.E., and Sparks, R.S.J., 2002, Dynamics of magma ascent and lava extrusion at Soufriere Hills Volcano, Montserrat, in Druitt, T.H., and Kokelaar, B.P., eds., The eruption of Soufriere Hills Volcano, Montserrat, from 1995 to 1999: *Geological Society, London, Memoir*, v. 21, p. 153–171.
- Melson, W.G., 1983, Monitoring the 1980–82 eruption of Mount St. Helens: Compositions and abundances of glass: *Science*, v. 221, p. 1387–1391.
- Mimatsu, M., 1995, Showa-Shinzan Diary: Sobetsu Town Office, Expanded Reprint, 179 p.
- Moore, G., Vennemann, T., and Carmichael, I.S.E., 1995, Solubility of water in magma to 2 kbar: *Geology*, v. 23, p. 1099–1102.
- Moore, G., Vennemann, T., and Carmichael, I.S.E., 1998, An empirical model for the solubility of H₂O in magmas to 3 kilobars: *American Mineralogist*, v. 83, no. 1–2, p. 36–42.
- Moran, S.C., 1994, Seismicity at Mount St. Helens, 1987–1992: Evidence for repressurization of an active magmatic system: *Journal of Geophysical Research*, v. 90, no. B3, p. 4341–4354.
- Moran, S.C., Malone, S., Qamar, A.I., Thelen, W., Wright, A.K., and Caplan-Auerbach, J., 2007, 2004–2005 Seismicity associated with the renewed dome-building eruption of Mount St. Helens, chap. 2 in Sherrod, D.R., Scott, W.E., and Stauffer, P.H., eds., A volcano rekindled: the first year of renewed eruptions at Mount St. Helens, 2004–2006: U.S. Geological Survey Professional Paper (this volume).
- Mullineaux, D.R., 1996, Pre-1980 tephra-fall deposits erupted from Mount St. Helens, Washington: U.S. Geological Survey 156, 99 p.
- Murphy, M.D., Sparks, R.S.J., Barclay, J., Carroll, M.R., Lejeune, A.-M., Brewer, T.S., Macdonald, R., Black, S., and Young, S., 2000, The role of magma mixing in triggering the current eruption at the Soufriere Hills volcano, Montserrat, West Indies: *Geophysical Research Letters*, v. 25, no. 18, p. 3433–3436
- Musumeci, C., Gresta, S., and Malone, S.D., 2001, Magma system recharge of Mount St. Helens from precise relative hypocenter location of microearthquakes: *Journal of Geophysical Research*, v. 107, no. B10, doi:10.1029/2001JB000629, 002002.
- Nakamura, M., 1995, Continuous mixing of crystal mush and replenished magma in the ongoing Unzen eruption: *Geology*, v. 23, no. 9, p. 807–810.
- Newman S., Stolper, E.M., and Epstein, S., 1986, Measurement of water in rhyolitic glasses: calibration of an infrared spectroscopic technique: *American Mineralogist*, v. 71, p. 1527–1541.
- Nielson, C.H., and Sigurdsson, H., 1981, Quantitative methods for electron microprobe analysis of sodium in natural and synthetic glasses: *American Mineralogist*, v. 66, p. 547–552.
- Nowak, M., and Behrens, H., 1995, The speciation of water in haplogranite melts determined by in situ near-infrared spectroscopy: *Geochimica et Cosmochimica Acta*, v. 59, p. 3445–3450.
- Pallister, J.S., Denlinger, R., Sherrod, D.R., Hoblitt, R.P., Cashman, K., Thornber, C.R., and Moran, S.C., 2006, Structural geology of the Mount St. Helens fault gouge zone—field relations along the volcanic conduit-wallrock interface [abs.]: *Eos (American Geophysical Union Transactions)*.
- Pallister, J.S., Heliker, C., and Hoblitt, R.P., 1991, Glimpses of the active pluton below Mount St. Helens [abs.]: *Eos (American Geophysical Union Transactions)*, v. 72, p. 576.

- Pallister, J.S., Hoblitt, R.P., Crandell, D.R., and Mullineaux, D.R., 1992, Mount St. Helens a decade after the 1980 eruptions: Magmatic models, chemical cycles, and a revised hazards assessment: *Bulletin of Volcanology*, v. 54, p. 126–146.
- Pallister, J.S., Hoblitt, R.P., Meeker, G.P., Knight, R.J., and Siems, D.F., 1996, Magma mixing at Mount Pinatubo: petrographic and chemical evidence from the 1991 deposits, *in* Newhall, C.G., and Punongbayan, R., eds., *Fire and mud: eruptions and lahars of Mount Pinatubo, Philippines*: Seattle, University of Washington Press, p. 687–732.
- Pallister, J.S., Reagan, M., and Cashman, K.V., 2005, A new eruptive cycle at Mount St. Helens?: *Eos*, v. 86, no. 48, p. 499–500.
- Pearce, N.J.G., Perkins, W.T., Westgate, J.A., Gorton, M.P., Jackson, S.E., Neal, C.R., and Chenery, S.P., 1997, A compilation of new and published major and trace element data for NIST SRM 610 and NIST SRM 612 glass reference standards: *Geostandards Newsletter*, v. 21, p. 115–144.
- Reagan, M.K., Cooper, K.M., Pallister, J.S., Thornber, C.R., and Wortel, M., 2007, Effects of degassing on ^{210}Po - ^{210}Pb - ^{226}Ra disequilibria in lavas erupted from Mount St. Helens 2004–2005, chap. 37 *in* Sherrod, D.R., Scott, W.E., and Stauffer, P.H., eds., *A volcano rekindled: the first year of renewed eruptions at Mount St. Helens, 2004–2006*: U.S. Geological Survey Professional Paper (this volume).
- Rowe, M.C., Thornber, C.R., and Kent, A.J.R., 2007, Geochemistry of 2004–2005 Mount St. Helens ash: identification and evolution of the juvenile component, chap. 29 *in* Sherrod, D.R., Scott, W.E., and Stauffer, P.H., eds., *A volcano rekindled: the first year of renewed eruptions at Mount St. Helens, 2004–2006*: U.S. Geological Survey Professional Paper (this volume).
- Rutherford, M., 1993, Experimental petrology applied to volcanic processes: *Eos* (American Geophysical Union Transactions), v. 74, no. 5, p. 49, 55.
- Rutherford, M.J., and Devine, J.D., III, 2007, Magmatic conditions and processes in the storage zone of the 2004–06 Mount St. Helens eruptions: the record in hornblende and plagioclase phenocrysts, chap. 31 *in* Sherrod, D.R., Scott, W.E., and Stauffer, P.H., eds., *A volcano rekindled: the first year of renewed eruptions at Mount St. Helens, 2004–2006*: U.S. Geological Survey Professional Paper (this volume).
- Rutherford, M.J., and Hill, P.M., 1993, Magma ascent rates from amphibole breakdown; an experimental study applied to the 1980–1986 Mount St. Helens eruptions: *Journal of Geophysical Research*, v. 98, no. B11, p. 19667–19685.
- Rutherford, M.J., Sigurdsson, H., Carey, S., and Davis, A., 1985, The May 18, 1980, eruption of Mount St. Helens; 1, Melt composition and experimental phase equilibria: *Journal of Geophysical Research*, v. 90, no. B4, p. 2929–2947.
- Scandone, R., and Malone, S.D., 1985, Magma supply, magma discharge, and readjustment of the feeding system of Mount St. Helens during 1980: *Journal of Volcanology and Geothermal Research*, v. 23, p. 239–262.
- Schilling, S.P., Thompson, R.A., Messerich, J.A., and Iwatsubo, E.Y., 2007, Mount St. Helens lava dome growth and surface modeling, 2004–2005, chap. 8, *in* Sherrod, D.R., Scott, W.E., and Stauffer, P.H., eds., *A volcano rekindled: the first year of renewed eruptions at Mount St. Helens, 2004–2006*: U.S. Geological Survey Professional Paper (this volume).
- Scott, W.E., Sherrod, D.R., and Gardner, C.A., 2007, Overview of 2004 to 2005, and continuing, eruption of Mount St. Helens, Washington, chap. 1 *in* Sherrod, D.R., Scott, W.E., and Stauffer, P.H., eds., *A volcano rekindled: the first year of renewed eruptions at Mount St. Helens, 2004–2006*: U.S. Geological Survey Professional Paper (this volume).
- Shen, A., and Keppler, H., 1995, Infrared spectroscopy of hydrous silicate melts to 1000°C and 10 kbar: direct observations of H₂O speciation in a diamond anvil cell: *American Mineralogist*, v. 80, p. 1335–1338.
- Sillitoe, R.H., 1973, The tops and bottoms of porphyry copper deposits: *Economic Geology*, v. 68, no. 6, p. 799–815.
- Silver, L.A., and Stolper, E.M., 1989, Water in albitic glasses: *Journal of Petrology*, v. 30, p. 667–709.
- Smith, A.L., and Roobol, M.J., 1990, Mt. Pelée, Martinique : a study of an active island arc volcano: *Geological Society of America Memoir* 175, 105 p.
- Smith, D., 2000, Insights into the evolution of the uppermost continental mantle from xenolith localities on and near the Colorado Plateau and regional comparisons: *Journal of Geophysical Research*, v. 105, no. B7, p. 16769–16781.
- Smith, D.R., and Leeman, W.P., 1987, petrogenesis of Mount St. Helens dacitic magmas: *Journal of Geophysical Research*, v. 92, no. B10, p. 10313–10334.
- Smith, D.R., and Leeman, W.P., 1996, The origin of Mount St. Helens andesites: *Journal of Volcanology and Geothermal Research*, v. 55, p. 271–303.
- Sowerby, J.R., and Keppler, H., 1999, Water speciation in rhyolitic melt determined by in-situ infrared spectroscopy: *American Mineralogist*, v. 84, p. 1843–1849.
- Sparks, R.S.J., Huppert, H.E., Turner, J.S., Sakuyama, M., and O'Hara, M.J., 1984, The fluid dynamics of evolving magma chambers: *Philosophical Transactions of the Royal Society of London, Series A, Mathematical and Physical Sciences*, v. 310, no. 1514, p. 511–534.
- Stormer, J.C., 1983, The effects of recalculation on estimates of temperature and oxygen fugacity from analyses of multi-component iron-titanium oxides: *American Mineralogist*, v. 68, p. 586–594.
- Streck, M.J., Broderick, C., Thornber, C.R., Clynne, M.A., and Pallister, J.S., 2007, Plagioclase populations and zoning in dacites of the 2004–2005 Mount St. Helens eruption: constraints for magma origin and dynamics, chap. 34 *in* Sherrod, D.R., Scott, W.E., and Stauffer, P.H., eds., *A*

- volcano rekindled: the first year of renewed eruptions at Mount St. Helens, 2004–2006: U.S. Geological Survey Professional Paper (this volume).
- Sun, S.S., and McDonough, W.F., 1989, Chemical and isotopic systematics of oceanic basalts: implications for mantle composition and processes, *in*: Saunders, A.D., and Norry, A.D., eds., *Magmatism in the ocean basins*: Geological Society of London Special Publication 42, p. 313-345.
- Swanson, D.A., Dzurisin, D., Holcomb, R.T., Iwatsubo, E.Y., Chadwick, W.W., Jr., Casadevall, T.J., Ewert, J.W., and Heliker, C.C., 1987, Growth of the lava dome at Mount St. Helens, Washington (USA), 1981–1983, *in* Fink, J.H., ed., *The emplacement of silicic lava domes and flows*: Boulder, Colo., Geological Society of America Special Paper 212, p. 1–16.
- Swanson, D.A., and Holcomb, R.T., 1990, Regularities in growth of the Mount St. Helens dacite dome, *in* Fink, J.H., ed., *Lava flows and domes*: Berlin, Springer, p. 3-25.
- Taggart, J.E., Lindsay, J.R., Scott, B.A., Vivit, D.V., Bartel, A.J., and Stewart, K.C., 1987, Analysis of geologic materials by X-ray fluorescence spectrometry, *in* Baedeker, P.A. ed., *Methods for geochemical analysis*: U.S Geological Survey Bulletin 1770, p. E1–E19.
- Thelen, W., Crosson, R.S., and Creager, K.C., 2007, Absolute and relative locations for earthquakes at Mount St. Helens using continuous data: implications for magmatic processes, chap. 4 *in* Sherrod, D.R., Scott, W.E., and Stauffer, P.H., eds., *A volcano rekindled: the first year of renewed eruptions at Mount St. Helens, 2004–2006*: U.S. Geological Survey Professional Paper (this volume).
- Thornber, C.R., Pallister, J.S., and Lowers, H.A., 2007a, Complex P-T history of amphiboles from the 2004–2005 eruption of Mount St. Helens, chap 32 *in* Sherrod, D.R., Scott, W.E., and Stauffer, P.H., eds., *A volcano rekindled: the first year of renewed eruptions at Mount St. Helens, 2004–2006*: U.S. Geological Survey Professional Paper (this volume).
- Thornber, C.R., Pallister, J.S., and others, a., 2007b, Digital database for samples collected during the 2004–2006 eruption of Mount St. Helens: U.S. Geological Survey Open-File Report, in technical review.
- Tuttle, O.F., and Bowen, N.L., 1958, Origin of granite in the light of experimental studies in the system NaAlSi₃O₈-KAlSi₃O₈-SiO₂-H₂O: Geological Society of America Memoir 74, 153 p.
- Vallance, J., Schilling, S., Messerich, J., and Thompson, R., 2007, Growth of recumbent dome and associated near-field deformation, chap. 9 *in* Sherrod, D.R., Scott, W.E., and Stauffer, P.H., eds., *A volcano rekindled: the first year of renewed eruptions at Mount St. Helens, 2004–2006*: U.S. Geological Survey Professional Paper (this volume).
- Venezky, D.Y., and Rutherford, M.J., 1999, Petrology and Fe-Ti oxide reequilibration of the 1991 Mount Unzen mixed magma: *Journal of Volcanology and Geothermal Research*, v. 89, no. 1, p. 213–230.
- Waite, G.P., 2006, Crustal P-wave speed structure under Mount St. Helens from local earthquake tomography [abs.]: *Eos (American Geophysical Union Transactions)*, in press.
- Watts, R.B., Heard, R.A., Sparks, R.S.J., and Young, S.R., 2002, Growth patterns and emplacement of the andesitic lava dome at Soufrière Hills Volcano, Montserrat, *in* Druitt, T.H., and Kokelaar, B.P., eds., *The eruption of Soufrière Hills Volcano, Montserrat, from 1995 to 1999*: Geological Society, London, *Memoirs*, v. 21, p. 115–152.
- Weaver, C.S., Grant, W.C., and Shemeta, J.E., 1987, Local crustal extension at Mount St. Helens, Washington: *Journal of Geophysical Research*, v. 92, p. 10170–10178.
- White, R.A., 1996, Precursory deep long-period earthquakes at Mount Pinatubo: Spatio-temporal link to basalt trigger, *in* Newhall, C.G., and Punongbayan, R.S., *Fire and mud: eruptions and lahars of Mount Pinatubo, Philippines*: Seattle, University of Washington Press, p. 307–328.
- Williams, D.L., Adams, G., Finn., C., Dzurisin, D., Johnson, D.J., and Denlinger, R., 1987, Evidence from gravity data for an intrusive complex beneath Mount St Helens: *Journal of Geophysical Research*, v. 92, p. 10210–10222.
- Williams, H., 1932, The history and character of volcanic domes: *University of California Bulletin of the Department of Geological Science*, v. 21, p. 51–146.
- Yamaguchi, D.K. and Hoblitt, R.P., 1995, Tree-ring dating of pre-1980 volcanic flowage deposits at Mount St. Helens, Washington: *Geological Society of America Bulletin*, v. 107, p. 1077-1093.

Digital Appendix

Appendix (digital). Oxide analyses used in thermobarometric calculations.